이학박사 학위논문

Scanning Josephson Tunneling Microscopy on High-T_C Superconductors

주사형 조셉슨 터널링 현미경을 이용한
고온 초전도체 연구

2019년 8월

서울대학교 대학원

물리천문학부

주상현

Scanning Josephson Tunneling Microscopy on High-T_C Superconductors

주사형 조셉슨 터널링 현미경을 이용한
고온 초전도체 연구

지도 교수 이 진 호

이 논문을 이학박사 학위 논문으로 제출함
2019년 8월

서울대학교 대학원
물리천문학부
주 상 현

주상현의 이학박사 학위논문을 인준함
2019년 6월

위 원 장	박 제 근	(인)
부위원장	이 진 호	(인)
위 원	김 기 훈	(인)
위 원	박 철 환	(인)
위 원	현 가 담	(인)

Abstract

Since the first High−T_C cuprate superconductor was discovered in 1986, tremendous quantity of theoretical and experimental studies have been conducted. Despite enthusiastic endeavors, the phenomena in cuprate superconductors are not fully understood and conundrums are mainly originated from the complicated phase diagram where various phases are entangled.

In this thesis, I will present the first application of nanometer resolution Scanning Josephson Tunneling Microscopy (SJTM) to a high−T_C cuprate superconductor, $Bi_2Sr_2CaCu_2O_{8+x}$. Josephson current, or Cooper−pair tunneling current, enables the direct access to superconducting order parameter and superconducting condensate. An *in−situ* fabricated $Bi_2Sr_2CaCu_2O_{8+x}$−tip is used with an aid of *in−situ* tip preparation stage.

SJTM studies are conducted at two different temperatures, 4.2 K and 50 mK. Detailed characterizations demonstrated imaging capability of Josephson critical current with nanometer resolution for both temperatures. In the SJTM study at 4.2 K, spatial variation of superconducting gap is directly measured for the first time, while the temperature window for SJTM is widely expanded to 4.2 K from mK. In the SJTM study at 50 mK, periodic modulation of superconducting condensate is observed for the first time.

Keyword : High−T_C superconductor, Scanning Josephson Tunneling Microscopy, Superconducting gap map, Pair density wave
Student Number : 2012−23101

Acknowledgements

This thesis could not have been written without the support of many people in many places. I would like to first thank my parents and my sister who helped me through long days and nights. I was very lucky to have their support.

I am grateful to have worked with Professor Jinho Lee as my advisor. He taught me how to be a physicist and inspired scientific creativity.

I am greatly indebted to Dr. Soo-hyon Phark for all his insightful advice. His guidance was critical to setting up the SNU STM1.

I would like to thank Jae-Joon Kim and Kyoung Seok Lee, who were my partners on the STM1 for the past seven years. We have not only researched together, but spent so many days and nights in the lab setting up and repairing the STM1. I have really enjoyed all of the years I worked with them and wish them success.

Thanks to Min Seok Park who led the lab and did all the hard work as the first group member. Also, thanks to other lab members, Junghoon Yoo, Jeong-Soo Kwak, and Sekye Jeon.

I would like to express my sincere gratitude to Professor Séamus Davis who is a truly passionate and distinguished scholar. I am grateful to have had the opportunity to work with him. I would also like to thank Dr. Kazuhiro Fujita, for answering all my questions and explaining everything so elaborately, and Dr. Chung Koo Kim for helping and advising me in so many ways. And I thank Hui Li and Dr. Zengyi Du, my labmates at BNL.

I would like to thank all my friends and soulmates, Kyungjun, Dongyoung, Jaehyuck, Jaeyoon, Minsu, Donghoon, Joongsuk, Taewook, Subong, Junwoo, Yuri, Yoonjeong and Sunmin. I am sorry that I cannot list all of them in here. Their support and encouragement allowed me to achieve the work here.

Table of Contents

List of Figures

Chapter 1. Introduction

1.1. Overview

In 1911, Heike Kamerlingh Onnes first discovered superconductivity by observing a sudden drop of electrical resistivity in mercury at 4.2 K. [1] Soon, superconductivity has found in many other materials, such as lead and tin. The first prominent characteristic of superconductors is revealed: perfect conductivity.

Another important characteristic of superconductivity is the perfect diamagnetism, which was discovered by Meissner and Ochsenfeld. [2] Superconductors not only repel magnetic flux from its interior but also expel presenting magnetic flux inside in a normal state as they are cooled down below superconducting transition temperature, T_C.

On the other hand, many theoretical efforts to elucidate the microscopic origin of the superconductivity was made. While phenomenological theories, the London theory [3] and the Ginzburg–Landau theory [4] were able to explain many aspects of this fascinating phenomenon, the celebrated Bardeen–Cooper–Schrieffer (BCS) theory [5] finally completes the microscopic theory for the superconductivity.

1.2. Brief History

The relentless search for the higher T_C superconductors was an ongoing global effort since the first discovery of superconductivity in 1911, however, the highest T_C reached 23 K in Nb_3Ge found in 1973. [6] An unexpected breakthrough was made by Bednorz and Muller in 1986. They discovered a new kind of superconductor in a perovskite cupric oxide or cuprate, $La_{2-x}Ba_xCuO_4$ (T_C ~ 30 K) [7] and in the

following year, the record of the highest T_C was by the discovery of $YBa_2Cu_3O_{7-\delta}$ with T_C ~ 93 K. [8] Many different cuprate superconductors were subsequently discovered and currently, the highest T_C of cuprate superconductor family reaches to 164 K in Hg-based compound under high pressure. [9] Recently, many new class of superconductors were discovered including iron-based superconductors [10-12] and H_2S [13] and especially, H_2S under ultra-high pressure achieves startling high T_C of 203 K. Meanwhile, in 2018, superconductivity was discovered in a twisted bilayer graphene for a certain twisted angle. [14] The history of T_C is shown in Figure 1.1.

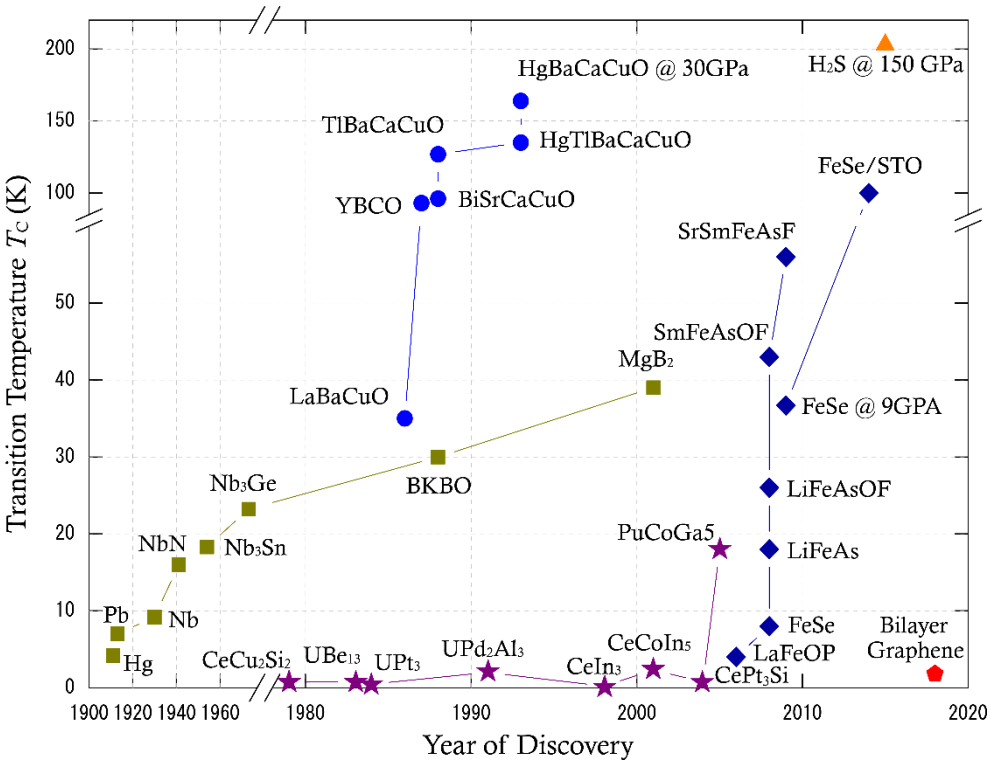

Figure 1.1: History of some of the discovered superconductors.

1. 3. Conventional Superconductivity

In the BCS theory, the Fermi surface becomes unstable in the presence of an attractive interaction between two electrons, regardless of the intensity of the interaction. [5] The attractive interaction is mediated by phonons and binds pairs of electrons, Cooper−pair, lying on the opposite sides of the Fermi surface.

When two electrons are added to the Fermi sea, the wave function of a Cooper−pair can be written as a product of orbital wave function and spin function. The total wave function has to be antisymmetric with respect to the exchange of two electrons, thus, for a spin−singlet pair, the orbital wave function is required to have an even parity, i.e., *s*−wave, *d*−wave, ... Cooper considered an attractive interaction between two electrons, $V_{\vec{k}\vec{k'}}$, such that [5],

$$V_{\vec{k}\vec{k'}} = \begin{cases} -V & (|\varepsilon_k| \ and \ |\varepsilon_{k'}| < \hbar\omega_c) \\ 0 & (\text{otherwise}) \end{cases} \tag{1.3.1}$$

, where the ε_k are unperturbed plane−wave energies and $\hbar\omega_C$ is a cutoff energy away from the Fermi energy so that the attractive interaction only occurs within the energy window. In the weak−coupling limit, this attractive interaction forms a bound state and the energy of a bound state is [15]

$$E \approx 2E_F - 2\hbar\omega_c e^{-2/N(0)V} \tag{1.3.2}$$

, where $N(0)$ is the density of states at the Fermi energy. The formation of a bound state with negative energy is actually found.

Having seen that the Fermi sea is unstable towards the formation of a Cooper pair, the large number of Cooper pairs lead to a new ground state, superconducting state, where Cooper pairs are condensed. BCS introduced the ground state wave function

$$|\Psi_{BCS}> = \prod_{\boldsymbol{k}}\left(|u_{\boldsymbol{k}}| + |v_{\boldsymbol{k}}|e^{i\varphi}c^{\dagger}_{\boldsymbol{k}\uparrow}c^{\dagger}_{-\boldsymbol{k}\downarrow}\right)|0> \qquad (1.3.3)$$

, where $u_{\boldsymbol{k}}$ and $v_{\boldsymbol{k}}$ are the coherence factors, ϕ is an arbitrary phase factor and |0> denotes the vacuum state. $c_{k\uparrow}$ $(c^{\dagger}_{k\uparrow})$ is the annihilation (creation) operator for a single electron of momentum k and spin up and $e^{i\phi}$ is a phase factor. As the $|u_{\boldsymbol{k}}|^2$ and $|v_{\boldsymbol{k}}|^2$ are the probability amplitude of the pair $(\boldsymbol{k}\uparrow, -\boldsymbol{k}\downarrow)$ being unoccupied and occupied, respectively, giving a constraint $u_{\boldsymbol{k}}^2 + v_{\boldsymbol{k}}^2 = 1$. Note that this wave function does not constrict on the total number of particles. However, it is possible to project out the N-particle part of the BCS ground state. Multiplying by $e^{-iN\phi}$ and integrating on ϕ over 2π gives

$$|\Psi_{BCS}> = \int_0^{2\pi} d\varphi e^{iN\varphi/2}\prod_{k}\left(|u_k| + |v_k|e^{i\varphi}c^{\dagger}_{k\uparrow}c^{\dagger}_{-k\downarrow}\right)|0> \qquad (1.3.4)$$

The phase ϕ becomes completely uncertain as it is integrated over all values while the particle number is fixed at N. This result hints the phase-number uncertainty relation

$$\Delta N\Delta\varphi \gtrsim 1 \qquad (1.3.5)$$

The conjugacy of number and phase will be crucial in the system subjected to the large Coulomb energy where ΔN is small.

To investigate the superconducting state, BCS considered the following Hamiltonian, so-called paring Hamiltonian,

$$H = \sum_{\boldsymbol{k}\sigma}\xi_{\boldsymbol{k}}c^{\dagger}_{\boldsymbol{k}\sigma}c_{\boldsymbol{k}\sigma} + \frac{1}{N}\sum_{\boldsymbol{k}\boldsymbol{k}'}V_{\boldsymbol{k}\boldsymbol{k}'}c^{\dagger}_{\boldsymbol{k}\uparrow}c^{\dagger}_{-\boldsymbol{k}\downarrow}c_{-\boldsymbol{k}'\downarrow}c_{\boldsymbol{k}'\uparrow} \qquad (1.3.6)$$

In the original BCS treatment, the variational method is used to determine the coherence factors and evaluate the ground state energy. However, to deal with excited states, a more sophisticated method is needed. Bogoliubov [16, 17] started from the mean-field

decoupling of the above Hamiltonian. The effective Hamiltonian becomes

$$H = \sum_{k\sigma} \xi_k c_{k\sigma}^{\dagger} c_{k\sigma} - \sum_{k} \left(\Delta_k c_{k\uparrow}^{\dagger} c_{-k\downarrow}^{\dagger} + \Delta_k^{*} c_{-k\downarrow} c_{k\uparrow} \right) + \sum_{k} \Delta_k < c_{k\uparrow}^{\dagger} c_{-k\downarrow}^{\dagger} > \qquad (1.3.7)$$

, where Δ_k is to be determined self−consistently

$$\Delta_k = -\frac{1}{N} \sum_{k'} V_{kk'} < c_{-k'\downarrow} c_{k'\uparrow} > \qquad (1.3.8)$$

Bogoliubov [17] and Valatin [16], independently showed that the above Hamiltonian can be diagonalized by the following canonical transformation with a new fermionic operator $\gamma_{k\sigma}$

$$\begin{aligned} c_{k\uparrow} &= u_k^{*} \gamma_{k\uparrow} + v_k \gamma_{-k\downarrow}^{\dagger} \\ c_{-k\downarrow}^{\dagger} &= u_k \gamma_{-k\downarrow}^{\dagger} - v_k^{*} \gamma_{k\uparrow} \end{aligned} \qquad (1.3.9)$$

The diagonalized Hamiltonian is then,

$$H = \sum_{k} \left(\xi_k - E_k + \Delta_k < c_{k\uparrow}^{\dagger} c_{-k\downarrow}^{\dagger} > \right) + \sum_{k\sigma} E_k \gamma_{k\sigma}^{\dagger} \gamma_{k\sigma} \qquad (1.3.10)$$

, where $E_k = \sqrt{\xi_k^2 + \Delta_k^2}$ and the coefficients u_k and v_k are chosen so that the Hamiltonian is diagonalized.

$$|v_k|^2 = 1 - |u_k|^2 = \frac{1}{2}\left(1 - \frac{\xi_k}{E_k}\right) \qquad (1.3.11)$$

The first term in the Hamiltonian is the ground state energy, while the second term provides the excitation energy upon creation of quasiparticles described by $\gamma_{k\sigma}$. The excitation spectrum E_k shown in Figure 1.2 (a), one can notice that the superconductor has an energy gap Δ_k even at the Fermi surface. Thus, the minimum energy $2|\Delta_k|$ is needed to excite the quasiparticles. These quasiparticles,

often called Bogoliubons or Bogoliubov quasiparticles, are the mixture of electrons and holes as can be seen from Eq. 1.3.9:

$$\gamma_{k\uparrow} = u_k c_{k\uparrow} - v_k c^{\dagger}_{-k\downarrow}$$
$$\gamma^{\dagger}_{-k\downarrow} = u^{*}_{\mathbf{k}} c^{\dagger}_{-k\downarrow} + v^{*}_{k} c_{k\uparrow} \qquad (1.3.12)$$

For example, in the normal state, where $\Delta_k = 0$, $u_k = 1$ & $v_k = 0$ for $\xi_k > 0$ whereas $v_k = 1$ & $u_k = 0$ for $\xi_k < 0$. That is, the quasiparticle creation operator,$\gamma^{\dagger}_{k}$, in the normal state creates an electron above the Fermi level, while creates a hole below the Fermi level with an opposite momentum and spin. In the superconducting state, as the coherence factors are following the relation in equation 1.3.11 (shown in Figure 1.2 (b)) and thus Bogoliubons become admixture of electrons and holes.

The density of states of the superconducting state, $N_S(E)$, with respect to the density of states of the normal state, $N_n(E)$, can be obtained from the excitation spectrum:

$$\frac{N_S(E)}{N_n(0)} = \begin{cases} \dfrac{E}{\sqrt{E^2 - \Delta^2}} & (E > \Delta) \\ 0 & (E < \Delta) \end{cases} \qquad (1.3.13)$$

, which is plotted in Figure 1.2 (c).

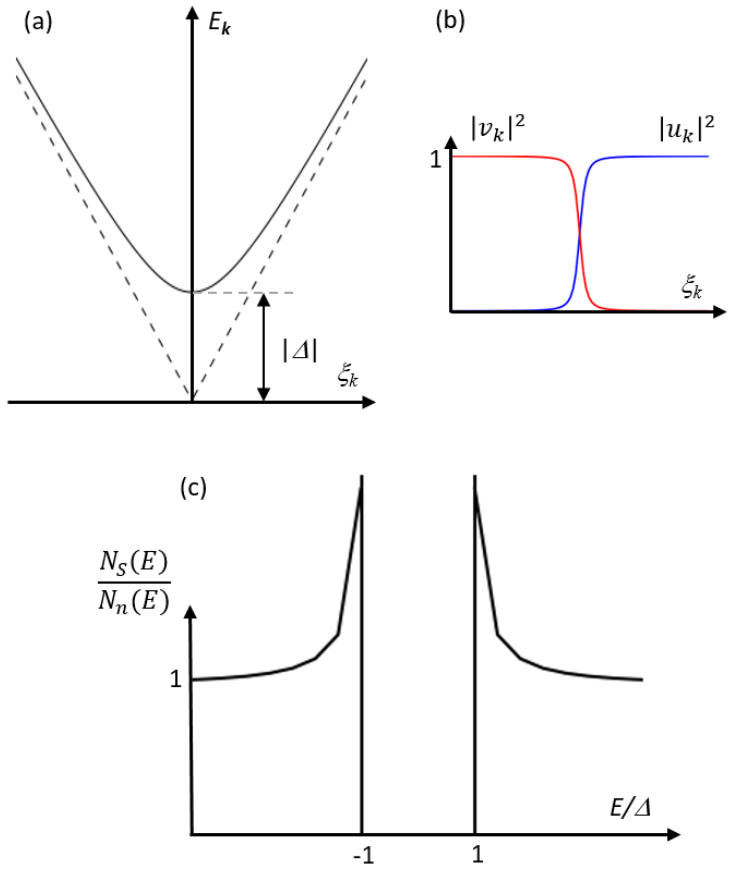

Figure 1.2: (a) Excitation spectrum, E_k, for BCS superconducting state. $\xi_{\boldsymbol{k}} = v_F(\boldsymbol{k} - \boldsymbol{k}_F)$. (b) Coherence factors $|u_k|^2$ and $|v_k|^2$ are plotted. (c) The density of states of BCS superconducting state, $N_S(E)$ normalized to the density of states of the normal state, $N_n(E)$.

Chapter 2. Phenomenology of Cuprates

2.1. Crystal Structure

Most of the cuprate superconductors are tetragonal lattice while some of them, for example, $YBa_2Cu_3O_{7-\delta}$ or $La_{2-x}Ba_xCuO_4$ at low temperature, have an orthorhombic lattice structure. Figure 2.1 shows the lattice structure of the cuprate superconductors. The heart of the cuprate superconductor is the CuO_2 plaquette, which can be quite obviously inferred from its name, as the superconductivity arises in the CuO_2 plane. Adjacent metallic-oxide layers separate copper oxide layers and, since the dopant atoms are usually introduced to these layers, they act as the charge reservoir doping the copper oxide layers.

Cuprates consist of the multiple numbers of CuO_2 layer. Although T_C increases with an increasing number of CuO_2 layer, triple-layer compounds are found to have the highest T_C because the synthesis of a quad-layer compound is known to be difficult.

This thesis will focus on $Bi_2Sr_2CaCu_2O_{8+x}$, which has a bi-layer CuO_2 planes. Since the bonding between two BiO layers is weak, $Bi_2Sr_2CaCu_2O_{8+x}$ is easy to be cleaved and reveals an atomically flat surface.

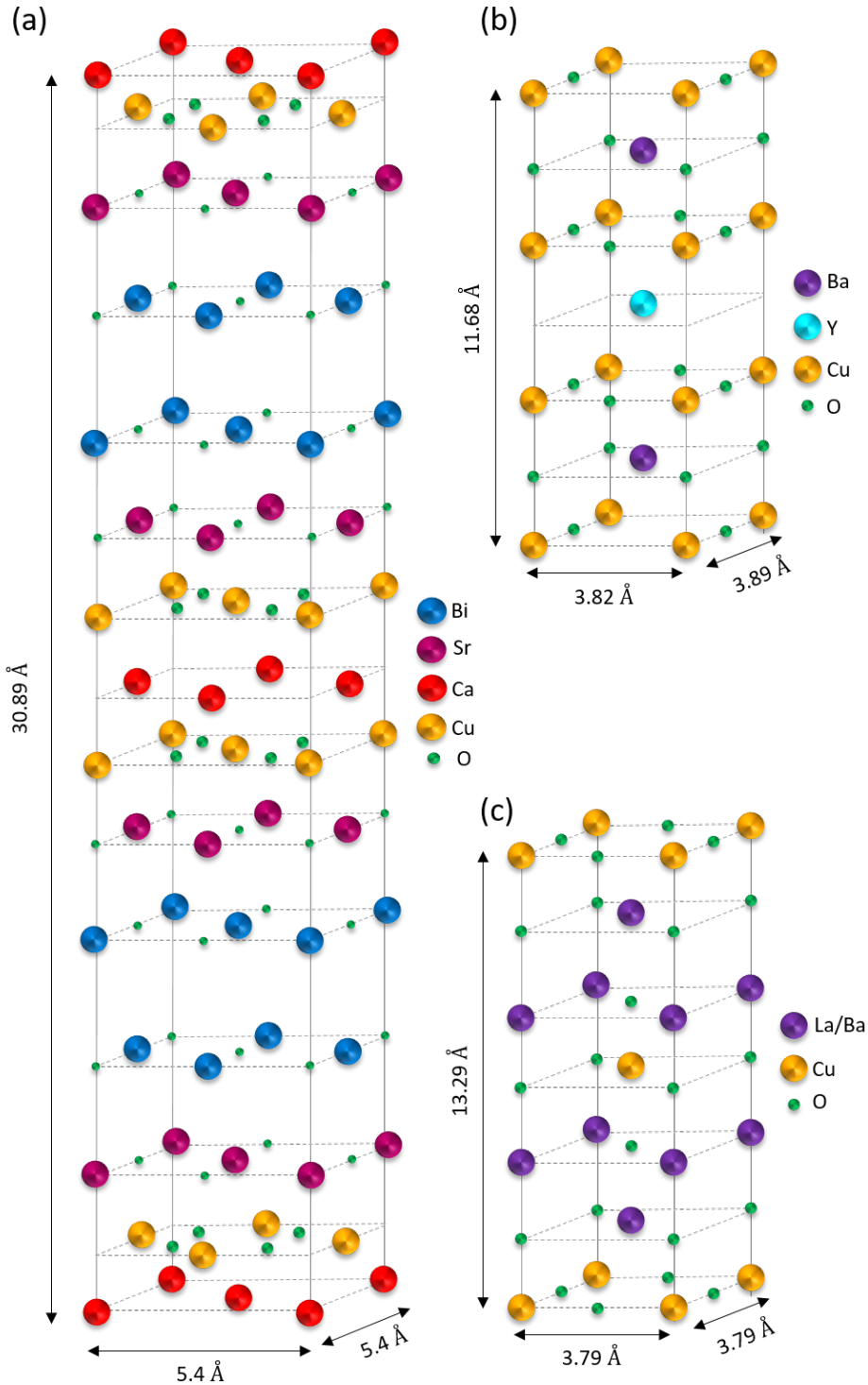

Figure 2.1: Unit cell lattice structure of (a) $Bi_2Sr_2CaCu_2O_{8+x}$, (b) $YBa_2Cu_3O_{7-\delta}$ and (c) $La_{2-x}Ba_xCuO_4$.

2.2. Phase diagram

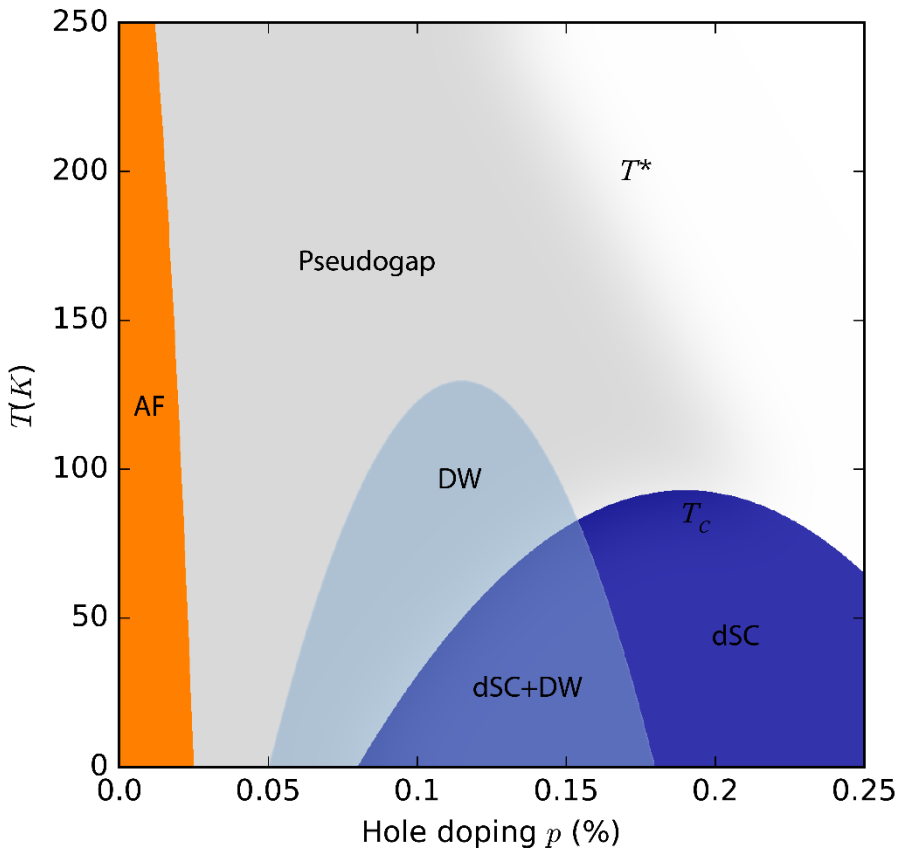

Figure 2.2: Phase diagram of the hole−doped cuprates in hole doping (p) vs temperature (T). Note that the precise boundary for pseudogap is still in debate. Abbreviations. AF: Antiferromagentic insulating phase, dSC: d−wave superconducting phase and DW: Density wave phase.

Since the first discovery of cuprate superconductors, physics of cuprate superconductors was intensely studied. It turns out that the cuprates exhibit a very rich and complex phase diagram. A phase diagram of the hole−doped cuprates is shown in Figure 2.2. Its parent material is an antiferromagnetic insulator and upon hole−doping, the

material becomes a d−wave superconductor. Further hole doping destroys superconductivity and turns it to a Fermi liquid. Along the temperature axis, we have an enigmatic phase, pseudogap. On the other hand, recently, various experiments observed the density wave ordering in underdoped range. I will briefly introduce each phases in the following sections.

2.2.1. AF Insulator: CuO_2 physics.

In low doping region, cuprates exhibit antiferromagnetic insulating phase. Since doping leads the rapid suppression of the AF correlations with the emergence of various states, naturally one would like to start to model from this state.

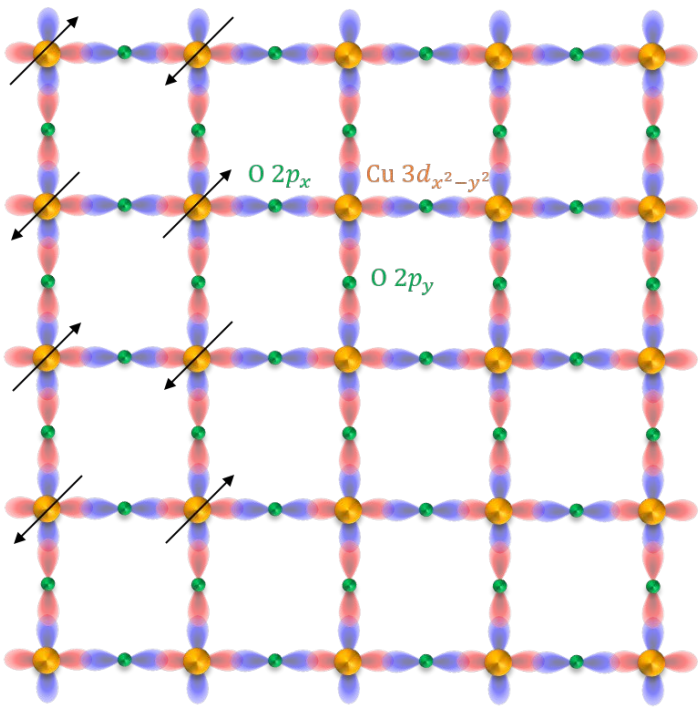

Figure 2.3: CuO_2 plane with Cu atoms in orange and oxygen atoms in green. The relevant Cu $3d_{x^2-y^2}$ and O $2p_{x,\,y}$ orbitals are shown. Black arrows represent the spin half state of each Cu atoms showing the anti−ferromagnetic ordering.

Key features of cuprates lie on CuO_2 plane. The crucial electronic degrees of freedom is revealed to be a singly occupied Cu $3d_{x^2-y^2}$ orbital, which is coupled to doubly occupied adjacent oxygen $2p_x$ and $2p_y$ orbitals.

Start from a simple Hubbard Hamiltonian considering only Cu atoms [18],

$$H = -t \sum_{<i,j>\sigma} \left(c_{i\sigma}^{\dagger} c_{j\sigma} + h.c. \right) + U \sum_{i} n_{i\uparrow} n_{i\downarrow} \qquad (2.2.1)$$

, where t is hopping parameter between nearest-neighbor sites and U is on-site Coulomb repulsion. To delocalize a carrier, an energy gain from inter-atomic hopping (t) has to be superior to an energy cost of doubly occupied state (U). It is believed to be in cuprates, U_d ~ 8 eV and t ~ 0.5 eV. [19] Hence, the on-site Coulomb repulsion prohibits an inter-atomic hopping making it an insulator, so-called "Mott-Hubbard insulator" [20]. However, this is not the end of the story in cuprates. CuO_2 plane consists of not only copper atom but also oxygen atoms. The on-site Coulomb potential splits Cu $3d_{x^2-y^2}$ band into upper- and lower- Hubbard band (UHB and LHB, respectively) with a gap U_d. On the other hand, an electron in the nearest-neighbor oxygen atom can hop to Cu atom introducing a charge excitation gap, Delta. When Delta is smaller than U_d, it is called a "charge-transfer insulator". [21-23] Figure 2.4 (a) and (b) show the schematic description of these two types of insulators. Cuprates are charge-transfer insulator as Δ is about 2 ~ 4 eV [22, 24, 25], which is actually smaller than U_d. As a result, an added hole will go in the O $2p$ band.

Having determined the schematic picture of CuO_2 plane, we can try to build an effective model. Since copper and oxygen atoms all are involved, it is natural to consider all of them explicitly in the model, so-called "three-band Hubbard model". [26, 27]

Zhang and Rice (ZR) [28] pointed out that a three−band Hubbard model can be reduced to a single−band Hubbard model owing to the formation of "Zhang−Rice singlet" (ZRS). ZR assumes that an extra hole introduced into oxygen band binds strongly with a localized hole in the Cu site and forms a singlet state. Thus, O $2p$ band is further split into two: ZR singlet band and non−bonding band. Since this ZR singlet state has a total spin of zero, it moves (hops) freely in the plane and considering the fact that it is centered at the Cu sites, the ZR singlet band can be described by a single−band model "t−J Hamiltonian", [28]

$$H = -t \sum_{<i,j>\sigma} P_G \left(c_{i\sigma}^{\dagger} c_{j\sigma} + h.c. \right) P_G + J \sum_{i} \left(\boldsymbol{S_i} \cdot \boldsymbol{Sj} - \frac{1}{2} n_i n_j \right)$$

, where $c_{i\sigma}$ annihilates a hole with spin σ on site i, P_G is the Gutzwiller projection operator that projects out any double occupancy and $\boldsymbol{S_i}$ is the spin operator.

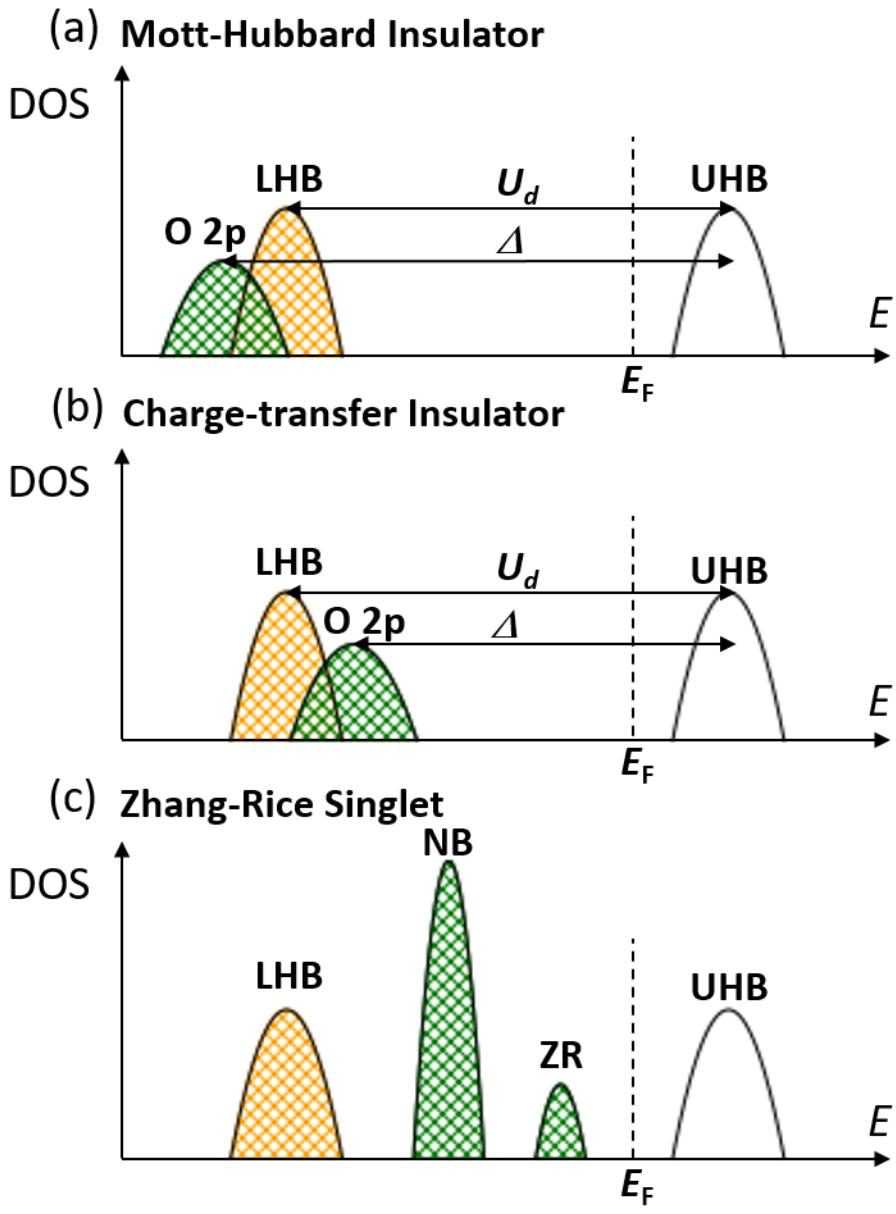

Figure 2.4: Schematic density of states (DOS) in the (a) Mott–Hubbard insulator, (b) Charge–transfer insulator and (c) Zhang–Rice singlet scenario. UHB and LHB represent upper Hubbard band and lower Hubbard band, respectively, ZR represents Zhang–Rice singlet and NB represents the non–bonding band.

2.2.2. *d*–wave Superconductivity

Upon further doping, cuprate becomes a superconductor. Beside its highest transition temperature T_C is strikingly high as 165 K [9], the *d*–wave order parameter symmetry (shown in Figure 2.5) is distinct from the conventional s–wave superconductors, which has an isotropic order parameter symmetry. The order parameter symmetry has been probed by different experiments. The amplitude of the order parameter was studied in k–space via Angle–Resolved Photoemission Spectroscopy (ARPES) [29] and specific heat [30], at the same time, tunneling measurement [31, 32] showed that conductance spectrum exhibits a V–shaped profile owing to the presence of a node rather than a U–shaped profile of *s*–wave superconductors. Phase–sensitive experiments [33–35] further confirmed *d*–wave order parameter symmetry.

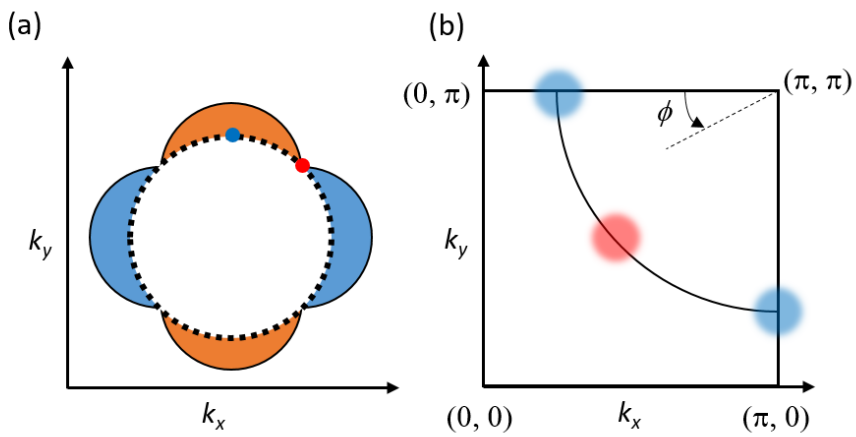

Figure 2.5: (a) Schematic *d*–wave superconducting gap function on the Fermi surface. Different colors represent the different sign of gap. Red and blue filled circles locate the node and anti–node, respectively. (b) The locations of node and anti–node in the first Brillouin zone are shown in red and blue filled circles.

2.2.3. Pseudogap

The most puzzling state in the cuprate phase diagram is the pseudogap state exhibiting a partial depletion of the density of states for $T_C < T < T^*$. The pseudogap is detected first by the Nuclear Magnetic Resonance (NMR) measurement in underdoped YBCO. [36]

Meanwhile, a partial spectral gap opening below the pseudogap onset temperature T^* is observed by ARPES [37−39] and optical conductivity [40−42]. ARPES experiments revealed that when the temperature cooled down below the pseudogap onset temperature T^*, the gap is opened near anti−nodal region (near (π, 0)) while near nodal area (near (π, π)) is still ungapped. As soon as the temperature is further cooled down below T_C, the ungapped near−nodal region is gapped resulting in a full d−wave order parameter. Apparently, there is a close relation between spectral gap measured below T_C (superconducting gap) and above T_C (pseudogap).

Presence of two different onset temperature of the gap opening naturally brings up a question that whether two gaps are really distinguished gaps (“Two gap picture”) or a single gap. ARPES investigated spectral gap in the anti−nodal region and nodal−region in two axes as shown in Figure 2.6 [38, 39, 43, 44]: doping dependence and temperature dependence. In the overdoped region where pseudogap is absent, momentum dependence of the spectral gap measured below T_C actually fits well with the d−wave gap function as one expected. However, as the doping level decreases, while the spectral gap near nodal region still follows the d−wave gap function, spectral gap close to the anti−nodal region starts to deviate from the d−wave functional form. Temperature dependence of two gaps shows the starker difference. Not only spectral gap near nodal region disappears at T_C but the amplitude of the spectral gap also grows with the increase of temperature below T_C. On the contrary, the spectral gap in the anti−nodal region is temperature independent and fully persists up to T^*, thereby supporting two gap picture.

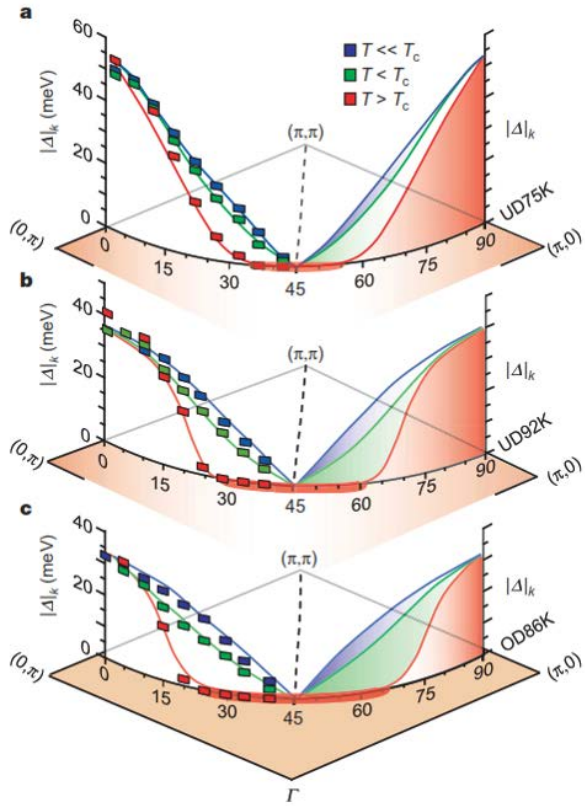

Figure 2.6: Temperature and angular dependence of the spectral gap for three different doping levels of $Bi_2Sr_2CaCu_2O_{8+x}$. Angles are defined in Figure 2.5 (b). For $T < T_C$, full d-wave gap is opened. As temperature increases, near-nodal gap decreases and vanishes for $T > T_C$. The anti-nodal gap persists and invariant over temperature change. Reproduced from [31].

Scanning Tunneling Microscopy (STM) and Raman spectroscopy results also support the two gap picture. The detailed studies of quasiparticle interference (QPI) on $Bi_2Sr_2CaCu_2O_{8+x}$ [45, 46] and $(Bi,Pb)_2(Sr,La)_2CuO_{6+\delta}$ [47] by STM revealed the coherent quasiparticles only exists for low energies, while for high energies, bi- or uni-directional charge ordering emerges. [48-51] The dichotomy of high/low energies suggests the coexistence of two different energy scales. Furthermore, temperature dependent

Scanning Tunneling Spectroscopy (STS) study in $Bi_2Sr_2CuO_{6+\delta}$ revealed the coexistence of homogeneous small gap and inhomogeneous large gap [52]. The other STS studies also found the two energy scales in d*I*/d*V* spectra. [31, 53] They showed that two energy scales evolving in a different way with underdoping, as shown in Figure 2.7, consistently suggesting the presence of two different energy scales.

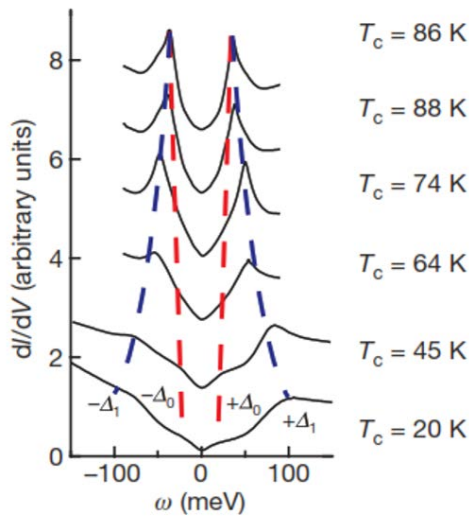

Figure 2.7: Conductance spectra for six different doping levels of $Bi_2Sr_2CaCu_2O_{8+x}$. Δ_1 (blue dashed line), characterized by the coherence peaks, is increased with underdoping, while Δ_0 (red dashed line), characterized by the kink in the spectra or from the extinction energy of coherent Bogoliubons, is nearly unchanged. Reproduced from [54].

Raman spectroscopy further supports two gap picture by detecting two distinct energy scales with opposite doping dependence. [55] In short, Figure 2.8 shows the compilation of the various experimental results. This figure clearly suggests that the pseudogap and superconducting gap are two distinct energy scales.

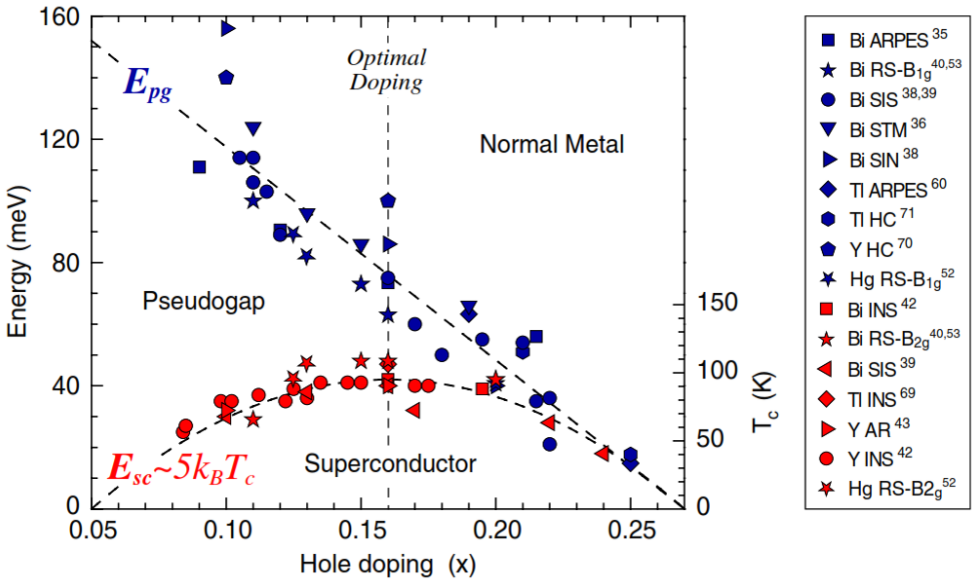

Figure 2.8: A compilation of energy scales from various experimental results. Two energy scales evolve differently as the doping level diminishes. Reproduced from [56].

2.2.4. Density waves in Cuprates

Numerous experimental results reported broken symmetries in the pseudogap state and superconducting state. Among the many them, charge density wave and spin density wave are ubiquitously found in hole-doped cuprates to break the lattice translational symmetry. Here I will briefly introduce the experimental evidence for the modulation of electronic density. More comprehensive reviews can be found in reference [57] and [58].

The first direct evidence for density waves in cuprates was found in $La_{2-x-y}Nd_ySr_xCu_2O_{4+\delta}$ by neutron scattering [59]. They observed charge and spin order peaks at Q_{charge} = (2, 2 ± 0.25, 0) and Q_{spin} = ~ (0.5, 0.5 ± 0.125, 0), respectively. The unidirectional nature of the ordered states provides the name of "stripe" order. Further neutron scattering and X-ray diffraction experiments confirmed the presence of the stripe orders in the other La-based compounds. [60-63]

Development of Resonance X-ray Scattering (RXS) provides as more evident picture of the charge ordered states. While RXS has high sensitivity to the modulations of the charge orders as its cross section is peaked at the electronic transition energy, neutron scattering and non-resonant X-ray scattering study the ordering of the charges indirectly by measuring the periodic lattice distortions.[58] Detection of stripe orders by RXS hence implies that stripe order is predominantly from the modulation of electronic density and the lattice distortions observed from neutron scattering and non-resonant X-ray scattering is a secondary effect. Abbamonte *et al.* [61] reported the first RXS study of charge order in $La_{2-x}Ba_xCuO_{4+\delta}$ and further RXS studies also found charge order in $La_{1.8-x}Eu_{0.2}Sr_xCuO_4$. [63]

Meanwhile, the observation of quantum oscillations in underdoped YBCO, with suppression of superconductivity by applying a high magnetic field, suggests the reconstruction of Fermi surface from hole-like Fermi barrels in the overdoped region to small electron pockets in underdoped region induced by the onset of the density wave. [64-66] While previous results showed the presence of density waves in the normal state of YBCO by applying a high magnetic field, distinguished charge density wave at zero field is also observed. [67]

Now, turn our attention to real-space studies in the charge orders by using STM. Since Hoffman *et al.* first found the charge order in vortex state in $Bi_2Sr_2CaCu_2O_{8+x}$ [68], many STM studies have reported detection of the short-range charge orders in $Bi_2Sr_2CaCu_2O_{8+x}$ [48, 49], $(Bi,Pb)_2(Sr,La)_2CuO_{6+\delta}$ [47] and $Ca_{2-x}Na_xCuO_2Cl_2$. [48, 69] Especially, Kohsaka *et al.* reported that the presence of bond-centered short-range unidirectional charge order [48]. This unidirectional charge order is later characterized as *d*-symmetry form factor density wave with having pseudogap energy as its characteristic energy. [49] On the other hand, there were attempts to combine real-space and reciprocal space techniques.

Comin *et al*. [70] and da Silva Neto *et al*. [71] performed STM and RXS studies in $Bi_2Sr_{2-x}La_xCuO_{6+\delta}$ and $Bi_2Sr_2CaCu_2O_{8+x}$, respectively, and they both found the charge orders. Recently, commensurate $4a_0$ period charge order has been found extremely underdoped insulating $Bi_2Sr_2CaCu_2O_{8+x}$. [72]

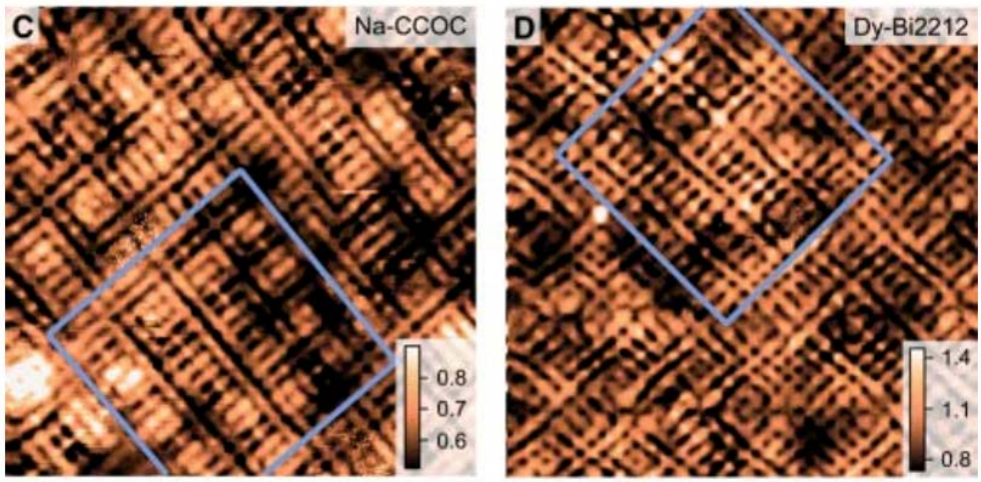

Figure 2.9: STM current ratio map, R(r, 150 meV) = I(r, 150 meV)/I(r, −150 meV), shows short−range charge order. Reproduced from [48].

3. Scanning Tunneling Microscopy (STM)

In 1960, Giaever [73] showed tunneling current in a superconductor−insulator−normal metal planar junction. Subsequently, Bardeen laid a theoretical foundation of tunneling spectroscopy [74]. Based on these theoretical developments, in 1982 the first STM was invented by Gerd Binnig and Heinrich Rohrer [75]. Since then, STM techniques have been improved dramatically and plays an important role in condensed matter physics field. The invention of Spectroscopic Imaging−STM (SI−STM) enables us to study the electronic structure of the material in real space with an excellent spatial resolution (< 1 Å). Together with the many spectroscopic tools such as ARPES, X−ray and many others, which provides detailed electronic structures in k−space, SI−STM completes the full picture of electronic structures of the material.

In this chapter, I will describe the principles of STM and techniques significant to STM research. Also, the design and capabilities of the SNU STM1.

3.1. Principles of STM

3.1.1 Electron Tunneling

I will follow the Bardeen's approach to describe the tunneling current of a tunnel junction. Here, a junction consists of two Fermi metal separated by an insulating barrier. Also, all the tunneling processes are assumed to be elastic.

The phenomenological tunneling Hamiltonian describing the tunneling of a particle across the vacuum barrier is given by

$$H_{\mathrm{T}} = \sum_{mn} M_{mn} c_{T,m}^{\dagger} c_{S,n} + h.c. \qquad (3.1.1)$$

Here, the operator $c^{\dagger}_{T,m}$ creates an electron in the single-particle state m on the tip and the operator $c_{R,n}$ destroys an electron in the single-particle state n on the sample. The tunneling matrix element M_{mn} can be written as [76]

$$M_{mn} = -\frac{\hbar^2}{2m}\oint dS\left(\psi_m \frac{\partial \psi_n}{\partial z} - \psi_n \frac{\partial \psi_m}{\partial z}\right) \tag{3.1.2}$$

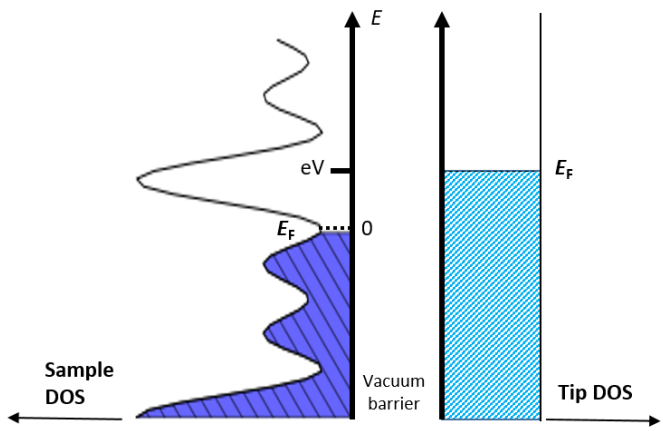

Figure 3.1: The density of states of the sample and tip. A bias voltage is applied to the sample.

The transfer rate from left to right electrode can be calculated by using Fermi's golden rule

$$w = \frac{2\pi}{\hbar}\ |M_{mn}|^2 \delta(E_m - E_n) \tag{3.1.3}$$

When a positive sample bias V is applied and measure energy relative to the sample Fermi surface, the current from tip to sample is then

$$I_{T\to S} = -2e\frac{2\pi}{\hbar}\int_{-\infty}^{\infty} |M|^2 \rho_T(E - eV) f(E - eV) \rho_S(E)[1 - f(E)]\, dE \tag{3.1.4}$$

, where $f(E)$ is the Fermi-Dirac distribution function and $\rho_{T(S)}$ is the density of states of a tip (sample). The tunneling matrix M is assumed to be a constant.

The current from sample to tip is

$$I_{S\to T} = -2e\frac{2\pi}{\hbar}\int_{-\infty}^{\infty}|M|^2\rho_T(E-eV)[1-f(E-eV)]\rho_S(E)f(E)\,dE \quad (3.1.5)$$

At sufficiently low temperature, the Fermi-Dirac distribution function is approximated to a step-function and the total current is thus

$$I = I_{T\to S} - I_{S\to T} \approx \int_0^{eV}|M|^2\rho_T(E-eV)\rho_S(E)\,dE \quad (3.1.6)$$

Tersoff and Hamann [77] assumed an s-wave apex of the tip and calculated the matrix element:

$$|M|^2 \propto \exp\left(-2\frac{\sqrt{2m\phi}}{\hbar}z\right) \quad (3.1.7)$$

, where ϕ is a convoluted work function, m is the electron mass and z is the separation between two electrodes. Further assuming the density of states of a tip is constant, the final current above is reduced to

$$I(z,V) \propto \exp\left(-2\frac{\sqrt{2m\phi}}{\hbar}z\right)\rho_T\int_0^{eV}\rho_S(E)\,dE \quad (3.1.8)$$

From the final form of the current, one can see the tunneling current changes exponentially with respect to the distance between tip and sample. For example, when a work function is ~5 eV, an Angstrom increase of the tip-sample distance causes an order of magnitude decrease in current. This will give an extremely high sensitivity of the current to the height changes on the surface.

Meanwhile, the differential conductance of the tunneling current is

$$g(z,V) = \frac{\mathrm{d}I}{\mathrm{d}V}(z,V) \propto \exp\left(-2\frac{\sqrt{2m\phi}}{\hbar}z\right)\rho_T\rho_S(eV) \qquad (3.1.9)$$

Hence, the differential conductance is proportional to the local density of states of a sample for a fixed z.

3.1.2 Operation of STM

The schematic of the STM operation is shown in Figure 3.2. A sharp metallic tip is attached to a piezoelectric tube. A piezoelectric tube provides a scanning ability through a fine x, y and z motions. A tip−sample junction is characterized by the tunneling current and a bias voltage, typically applied to a sample. In order to keep the constant tunneling current, a PID feedback loop is exploited. When the tunneling current exceeds a setpoint current I_S, piezoelectric tube retracts to increase the tip−sample distance. Conversely, when the tunneling current is lower than a setpoint current, the tip−sample distance is reduced by extending the piezoelectric tube. Thus, an STM junction is typically specified with a setpoint current I_S and a sample bias voltage V, or a junction resistance R_J.

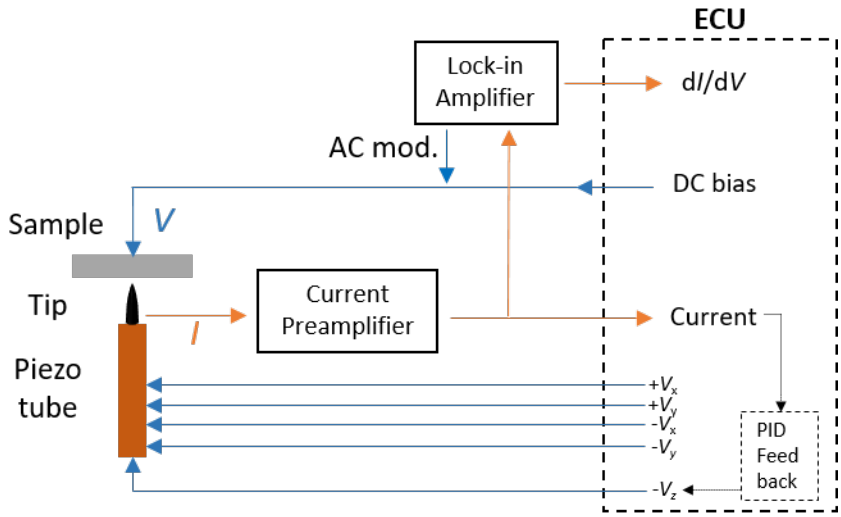

Figure 3.2: Schematic of the STM operation. Block diagram shows a simple version of the connection between STM and electronic control unit (ECU). ECU controls the sample bias and piezo tube while collecting data (tunneling current & d*I*/d*V*).

3.2. Types of Measurements

3.2.1 Topography

Topographic image of a sample surface can be measured by two different methods: constant current mode and constant height mode. In constant height mode, the height of a tip (voltage applied on z-piezotube) is kept fixed. Thus, the tunneling current will vary as the surface height changes giving a topographic image of a surface. Although the process is straightforward, this mode is not a popular choice for topography. If a sample surface is too rough, a tip can collide with a sample or a tip can be out of tunneling range.

More reliable topography is performed in constant current mode. Rather than a fixed height, the tunneling current is fixed. Equation 3.1.8 shows that the tunneling current has exponential sensitivity to

the tip−sample distance. In order to keep the tunneling current constant, tip height will vary along with the surface height. The record of the tip height provides the topographic image of a sample surface. Figure 3.3 shows an atomically resolved topographic image of $Bi_2Sr_2CaCu_2O_{8+x}$ in an 80 nm x 80 nm field of view measured in constant current mode.

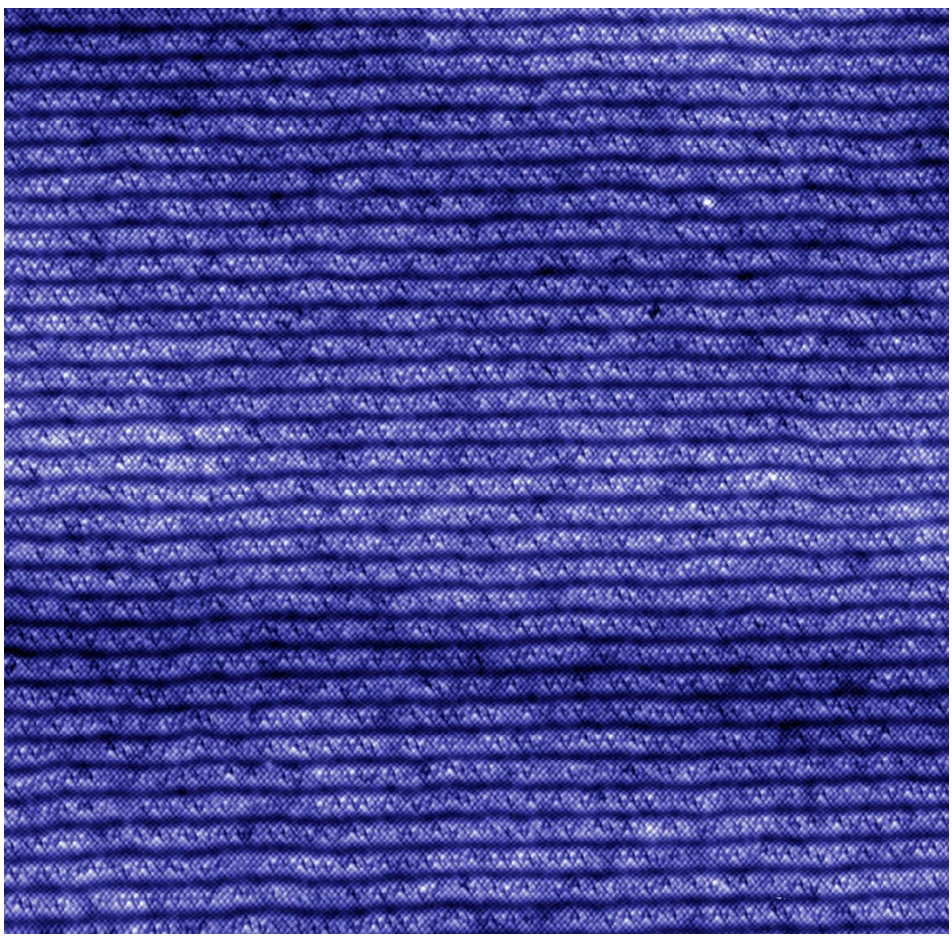

Figure 3.3: Topographic image of a $Bi_2Sr_2CaCu_2O_{8+x}$ sample in an 80 nm x 80 nm field of view measured by SNU STM1. (Junction setup: 100 mV / 10 pA, 1100 pixels^2)

3.2.2 Scanning Tunneling Spectroscopy

I have shown that the differential conductance is proportional to the local density of states of a sample for a fixed tip–sample distance.

$$g(z,V) = \frac{\mathrm{d}I}{\mathrm{d}V}(z,V) \propto \exp\left(-2\frac{\sqrt{2m\phi}}{\hbar}z\right)\rho_T\rho_S(eV) \propto \rho_S(eV) \quad (3.1.10)$$

Sweeping the sample bias voltage while fixing a tip–sample distance provides the local density of states of the sample. The differential conductance can be calculated by numerical derivation of the tunneling current, $I(z, V)$. However, the lock–in technique provides a better signal–to–noise ratio. When a small AC voltage modulation, $A\sin(\omega t)$, superposed onto a DC sample bias voltage, V_0, the Taylor expansion of the tunneling current is then

$$\begin{aligned} I\big(z,V(t)\big) &= I(z,V_0 + Asin(\omega t)) \\ &= I(z,V_0) + \frac{dI(z,V)}{dV}\bigg|_{V_0} ASin(\omega t) + \frac{1}{2}\frac{\mathrm{d}^2 I(z,V)}{dV^2}\bigg|_{V_0} \big(ASin(\omega t)\big)^2 + \cdots \end{aligned} \quad (3.1.11)$$

Thus, measuring the amplitude of the first harmonic by using a lock–in amplifier gives the differential conductance. To fully utilize the power of a lock–in technique, the driving frequency of the AC modulation has to be chosen carefully so that it is far away from the presenting noise band.

Differential conductance measurement across the uniformly spaced two–dimensional array, $g(\boldsymbol{r}, E)$, is called differential conductance map. This constitutes a three–dimensional array, two associated with spatial coordinates and one associated with energy. Figure 3.4 shows the data structure of a differential conductance map. Current and $\mathrm{d}I/\mathrm{d}V$ are measured at each pixel in a two–dimensional grid with varying sample bias voltage thus forming a three–dimensional data structure (x, y, E). For an analysis, three–dimensional data is

reduced to two dimensional or one-dimensional data by fixing one or two axes. If energy is fixed, E_0, a compilation of $g(x, y, E_0)$ is obtained. On the other hand, with fixed spatial coordinates, a point spectrum, $g(E)$, is obtained.

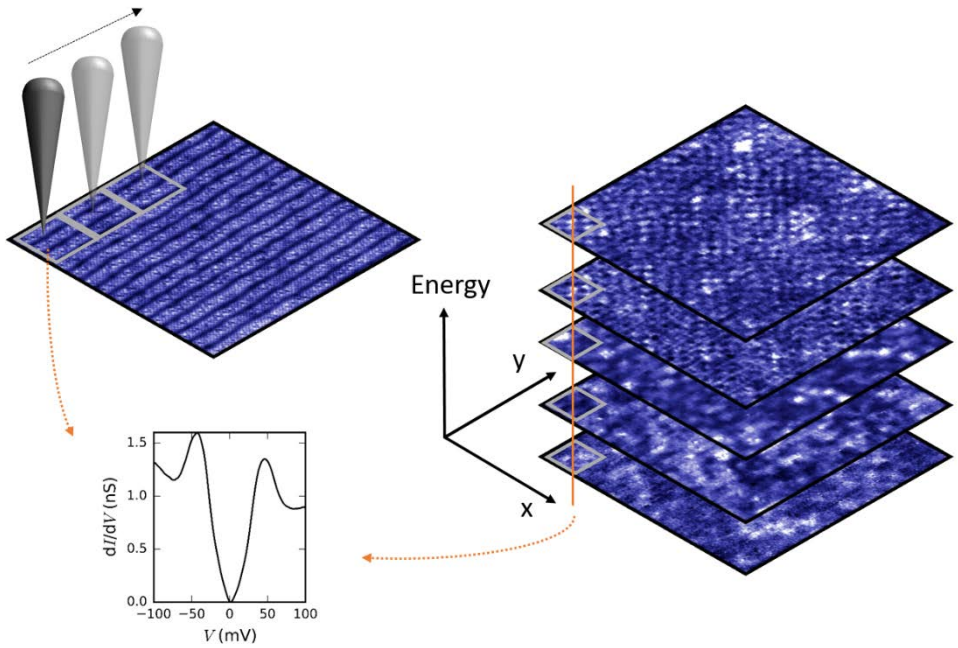

Figure 3.4: Schematic illustration of STS. Current and conductance spectrum are measured at each pixel in an evenly spaced two-dimensional grid. Thus, at each pixels gain extra energy axis and eventually, the data structure becomes three dimensional: x, y, and energy axes.

3.3. Design and Construction of Low Temperature-STM

The high sensitivity of the tunneling current with respect to the tip-sample distance enables a fine z-resolution, however, at the same time, tiny fluctuations, such as vibration and acoustic noise, can ruin STM experiments. The design philosophy of Low Temperature-STM (LT-STM) is thus to maximize the stability of STM by lowering

mechanical and electrical noises.

LT-STM constitutes of three components: Ultra-Low Vibration Laboratory (ULV-Lab), cryostat and STM head. While ULV-Lab isolates STM from the external perturbations, such as vibrations and acoustic noise, cryostat provides a low temperature measurement environment. Finally, the actual measurement is performed in the STM head.

3.3.1. Ultra-Low Vibration Laboratory

The entire lab space is divided into a control room, pump room, and four identical ULV facilities. Schematic diagram of the laboratory is depicted in Figure 3.5.

The main goal of ULV-Lab design was to achieve maximum vibration isolation while making them as compact as possible. Each ULV room has a rectangular pit with four niches on top of the concrete base. 30 tons of high-density concrete blocks are constructed inside these pits. To isolate these concrete blocks from external vibrations, they are separated from all walls and also each of them is supported by six air springs for further vibration isolations from the foundation. The niches in the pit provide space for the maintenance of the air springs. With this niched pit design, the required areal space reduced by half compared to the existing designs, which requires extra space around the concrete blocks.

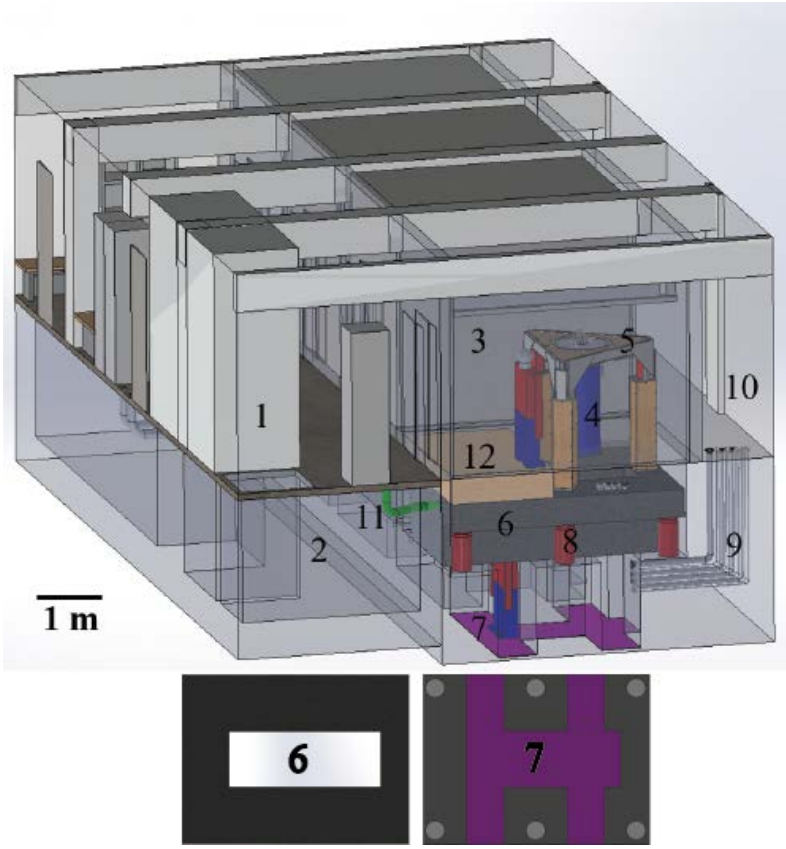

Figure 3.5: Schematic diagram of the SNU STM laboratory. Researchers depicted in the diagram are 180 cm tall. STM can be controlled from the control room (1). Space for the sample preparation (2). Inside the acoustic room (3), a cryostat and a dewar (4) are mounted on the main table (5) which is supported by three air springs that are installed on top of the legs. The acoustic room is installed on top of the inertia block (6). The inertia block is on top of the concrete base (7) and six air springs (8) on the concrete base support the inertia blocks. Pump lines (9) are buried in the inertia block and base. They are connected to the pump room (10). The signal lines are extended to control the STM through PVC pipes (11) buried in the inertia blocks. To overcome the low-level ceiling, the acoustic room has a floor level lower than that of the control room. To resolve this problem, a false floor (12) is installed on top of the inertia blocks. Top view of the inertia block (6) and the concrete base (7) are also shown for clarity.

On top of the concrete block, acoustic isolation room is constructed to isolate STM from the acoustic noise. The main table for STM is installed inside the acoustic room and supported by an additional three air springs. Each air springs is placed on top of the leg, which is filled with lead shots to increase the mass. All the features in the ULV-Lab are designed to have a resonance frequency as low as possible. The resonance frequencies of two sets of air springs are chosen to be different. The vibration isolation performance can be found in Figure 3.6.

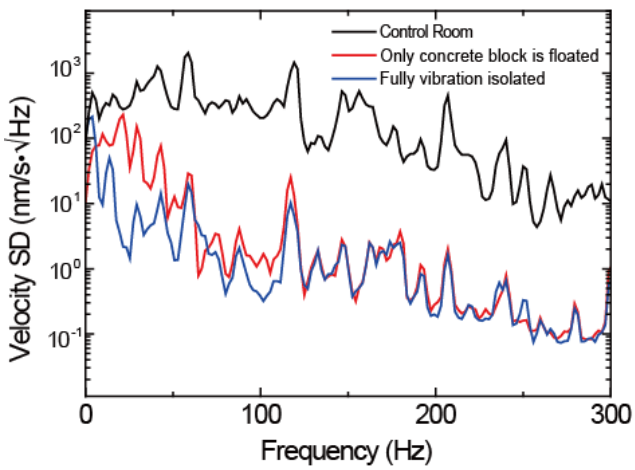

Figure 3.6: Velocity spectral density, measured by an OYO Geospace GEO-GS-11D, is plotted. The black curve shows the vibration noise measured in the control room. Inside the acoustic room, the geophone was installed on top of the main table. When the air springs supporting the inertia block is inflated (red curve) and all the vibration isolation system is activated (blue curve), vibration noise at all frequencies is highly suppressed.

3.3.2. Cryostat

Figure 3.7 shows the 3D drawings of the cryostat and the liquid helium Dewar. The cryostat has three stages: 4K plate, 1K plate, and

mK pot. A sample cleaving stage is placed right below the 4K plate and STM head is installed at the bottom end of the cryostat to have maximum temperature stability.

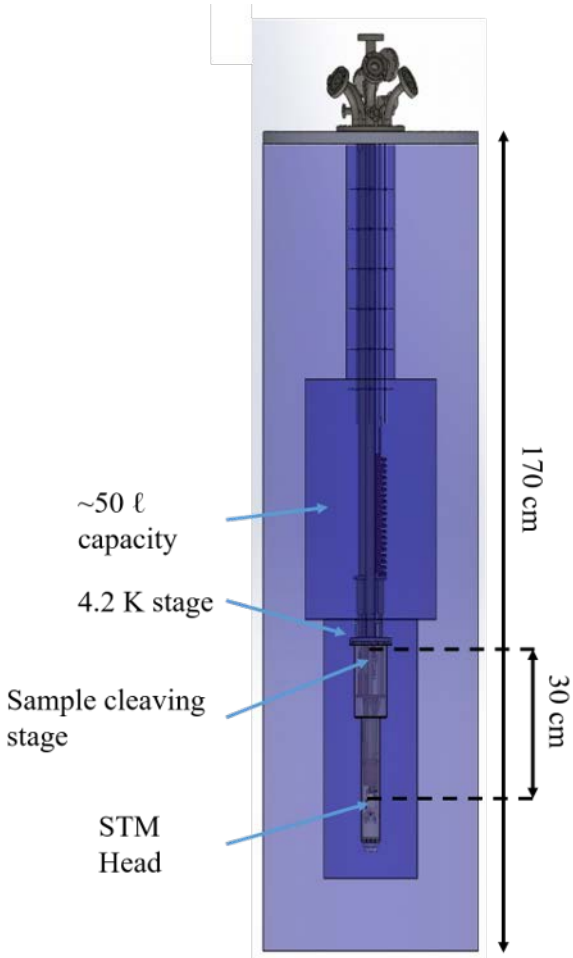

Figure 3.7: 3D drawings of the cryostat and the dewar. Location of the sample cleaving stage and the STM head is depicted.

3.3.3. STM Head

Figure 3.8 shows the 3D drawing of STM Head. STM Head mainly constitutes of four modules: Scanner, Walker, sample receptacle and field emission stage. All these modules are assembled in a Shapal^{TM}

Hi-M Soft body.

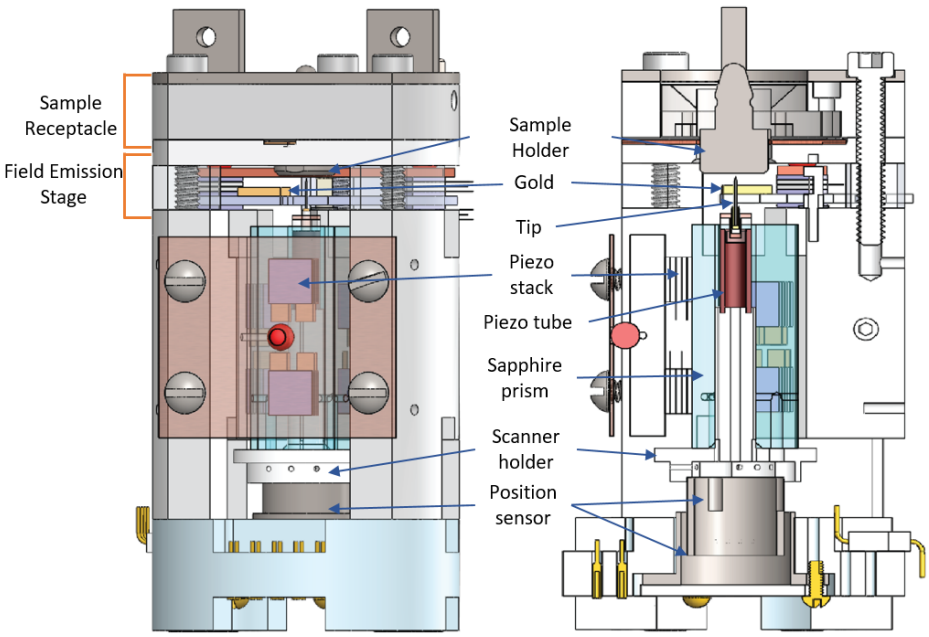

Figure 3.8: 3D drawing of the STM head design (left) and its cross-sectional view (right).

The scanner is the core component of the STM head and its assembly consists of a tip, piezoelectric tube, scanner holder and sapphire prism. A tip is placed on top of the piezoelectric tube, which provides scanning motion. The piezoelectric tube has four split electrode outside and a single electrode. Applying voltages to these electrodes individually, the piezoelectric tube can be bent or stretched (retracted) giving the x, y, and z scanning motions. The length of the piezoelectric tube used in this study is 0.375" ≈ 9.5 mm. The piezoelectric tube is placed inside the sapphire prism and both components are glued to the scanner holder.

While the scanner module provides a fine *x*, *y* and *z* motions for the measurement, the walker module gives a coarse *z* motion. The design of the walker module is followed by the famous S. H. Pan's design

[78], which utilizes six piezoelectric shear stacks. All six piezoelectric shear stacks are in contact with the sapphire prism and move it through a slip-stick motion.

The most distinguished component of the STM head used in this study is the field emission stage. A new tip is installed in the STM head from the ambient condition, oxide layers cover the surface of the tip. Moreover, as a lateral resolution of scanning highly depends on the sharpness of the apex of a tip, it is essential to have an atomically sharp tip. Furthermore, even with a well-prepared tip, many instabilities, such as contaminants or rough surfaces, can cause a tip change during measurement. In every case, a tip has to be re-prepared for the measurement.

Among many techniques to prepare such a sharp tip, field emission technique is one popular choice that can be done *in-situ.* [79-81] By applying high voltages, typically 100 to 300 volts, on a gold target, a field emission current flows through the tip-gold junction. The current will suffer a sudden drop or increase when the tip is changed due to a high electric field. Repetition of this process eventually produces a sharp and clean tip. This biggest advantage of this technique is that it is performed *in-situ*. Thus, it doesn't require to take out a tip for the tip treatment. However, a conventional STM head design has a limitation that the sample under measurement has to be replaced with a gold target for the tip preparation. The replacing process not only consumes considerable time (> ~24 hours) but also requires to discard a sample under measurement. The field emission stage is developed to overcome these problems by providing the ability to move a gold target to be aligned with a tip while leaving a sample intact.

Figure 3.9 shows the design of the field emission stage. This stage is installed right below the sample receptacle and consists of four piezoelectric shear stacks, sapphire plate. The field emission stage is designed to be completely independent module thus it does not

interfere with the sample receptacle stage. A gold target is installed on top of the sapphire plate, which can be rotated. The rotation motion is provided by the four piezoelectric shear stacks via the slip–stick motion along the tangential direction of the sapphire plate. During the sample measurement, the gold target is rotated away from a tip so that it won't interfere with the vertical motion of the scanner (Figure 3.9 (a) and (c)). When the tip needs to be prepared, the gold target is rotated and aligned with the tip (Figure 3.9 (b) and (d)). These processes are completely independent to the sample, thus only requires relatively short time (< 12 hours), at the same time, saves the sample. Another advantage of this stage is its versatility. By adding other functional materials, such as ferromagnetic or superconducting material, the tip can be formed to have different physical properties.

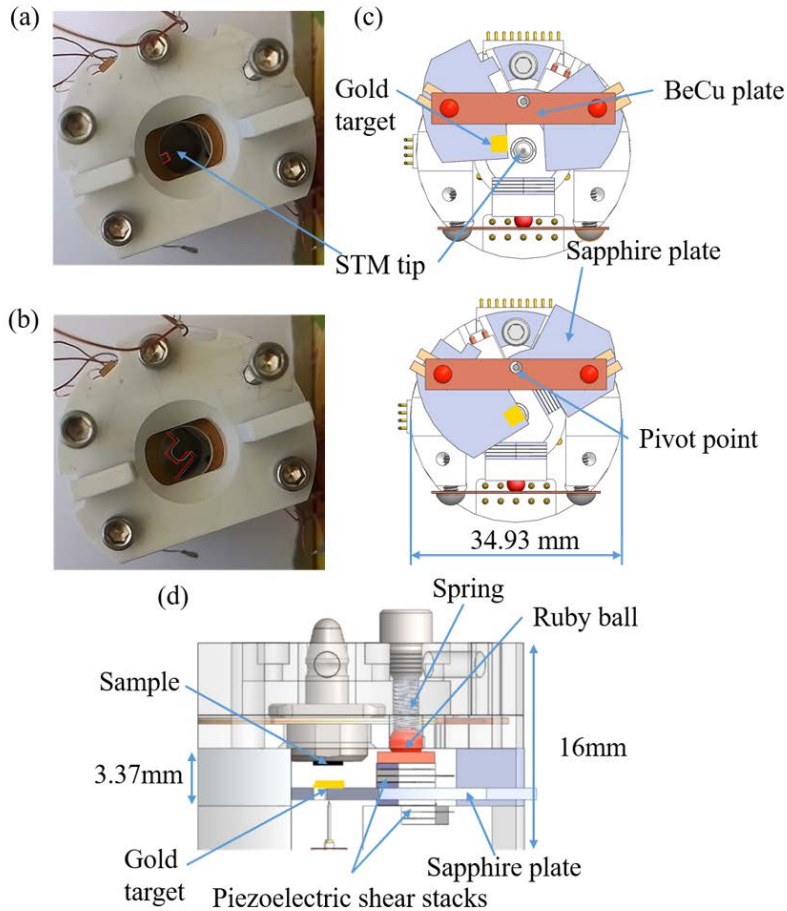

Figure 3.9: Top view of the STM head. When the gold target is (a) out of the tip position and (b) on the tip position. Red lines show the location of the gold target. The gold target is not installed on the sapphire plate in these pictures. (c) Top view of the STM head with top parts removed for more clarity. (d) Side view of the STM head. There are two pairs of piezoelectric shear stacks above and below the sapphire plate. A pair of the piezoelectric shear stacks attached to the STM head body and another pair of the piezoelectric shear stacks is attached to the BeCu plate and pressed by the BeCu plate, ruby balls, springs, and bolts.

4. Scanning Josephson Tunneling Microscopy

4.1. Introduction

The idea of Scanning Josephson Tunneling Microscopy (SJTM) is utilizing STM imaging capabilities to measure Cooper-pair density. Although conventional STM experiments were able to measure many different electronic degrees of freedoms with an excellent *r*-space resolution, there was one constraint that STM measures quasiparticle tunneling current. Quasiparticles contain information about Cooper-pairs, however, there is always an ambiguity as they are not Cooper-pairs themselves. Especially in cuprates, the pseudogap phase has an intimate connection to the superconductivity and purportedly coexists with the superconductivity. Under these circumstances, the direct measurement of superconducting condensate is crucial to study superconductivity and pseudogap. SJTM measures Cooper-pair tunneling current via Josephson effect instead of quasiparticle tunneling current, thus directly measures the superconducting condensate. All the STM imaging capabilities are retained so that SJTM still has an excellent *r*-space resolution. Moreover, by controlling the tip-sample distance, we can choose what to measure, quasiparticle tunneling and Cooper-pair tunneling, which provides a direct comparison between them.

4.2. Brief History

Early SJTM studies are performed in conventional superconductors. The first SJTM is reported by Naaman *et al.* [82] in a Pb film using Pb deposited tip. They were able to measure Josephson effect, although no scanning result was reported. Successive SJTM studied Pb and Al using Pb or Al tip and measured Josephson effect with an atomically resolved topographic image, but no scanning spectroscopy was reported. [83] Later, Proslier *et al.* [84] finally succeeded to achieve scanning spectroscopy in MgB_2 using MgB_2-tip. While all the

SJTM studies concentrated on the conventional superconductors, Kimura *et al.* [85] tried to apply SJTM to a high− T_C superconductor with Pb tip, but they weren't able to obtain scanning results.

4.3. Single-particle Tunneling in Superconductor Junction.

Josephson effect is a pair−tunneling phenomenon when two superconductors are weakly−linked. A typical type of Josephson junction is SIS (Superconductor−Insulator−Superconductor), while SNS (Superconductor−Normal metal−Superconductor) or different geometries are also possible. The necessary condition to have Josephson effect is coupling between two superconductors by having overlapped wave functions in the weak link. Here, Josephson junction will be discussed only within SIS junction, where superconductors are all BCS superconductors unless specified.

4.3.1. Quasiparticle Tunneling

The tunneling Hamiltonian of two metals (superconductors) can be written as a form of

$$H_{\mathrm{T}} = \sum_{\boldsymbol{kq}\sigma} T_{\boldsymbol{kq}} c^{\dagger}_{\boldsymbol{k}\sigma} c_{\boldsymbol{q}\sigma} + h.c. \qquad (4.3.1)$$

, where $T_{\boldsymbol{kq}}$ is a tunneling matrix element and $c^{\dagger}_{\boldsymbol{k}\sigma}$ ($c_{\boldsymbol{q}\sigma}$) creates (annihilates) an electron with momentum k and spin σ. Here, we assumed no magnetic perturbations so that no spin−flip process occurs in the tunneling process.

By exploiting Fermi's Golden rule, the net tunneling current can be written as

$$I = |T|^2 \int_{-\infty}^{\infty} N_1(E) N_2(E + eV)[f(E) - f(E + eV)]dE \tag{4.3.2}$$

, where the tunneling matrix element is assumed to be a constant, $N(E)$ is the density of states of an electrode and $f(E)$ is the Fermi–Dirac distribution function.

As a start, it's instructive to consider normal metal – normal metal junction. The tunneling current becomes

$$\begin{aligned} I_{\mathrm{nn}} &= |T|^2 N_1(0) N_2(0) \int_{-\infty}^{\infty} [f(E) - f(E + eV)]dE \\ &= |T|^2 N_1(0) N_2(0) eV \equiv G_{nn} V \end{aligned} \tag{4.3.3}$$

and we get an Ohmic junction as expected.

Now, let's replace one metal electrode with a superconductor. The density of states of a superconductor is given by

$$\frac{N_{\mathrm{S}}(E)}{N_n(0)} = \begin{cases} \dfrac{E}{\sqrt{E^2 - \Delta^2}} & (E > \Delta) \\ 0 & (E < \Delta) \end{cases} \tag{4.3.4}$$

, hence the net current becomes

$$I_{\mathrm{Sn}} = |T|^2 N_1(0) N_2(0) \int_{-\infty}^{\infty} \frac{N_{2S}(E)}{N_2(0)} [f(E) - f(E + eV)]dE \tag{4.3.5}$$

The qualitative behavior of current–voltage characteristic can be easily understood in Figure 4.1 (a) and (b). At $T = 0$, when the chemical potential difference is large enough to create quasiparticles, i.e., $e|V| \geq \Delta$, current starts to flow, otherwise, there will be no tunneling current. Recall that the quasiparticles are hole and electron

mixture, resulting tunneling current also maintain superconductor's particle−hole symmetry.

When both electrodes are superconductors, the tunneling current becomes

$$I_{SS} = |T|^2 N_1(0) N_2(0) \int_{-\infty}^{\infty} \frac{|E|}{\sqrt{E^2 - \Delta_1^2}} \frac{|E + eV|}{\sqrt{(E + eV)^2 - \Delta_2^2}} [f(E) - f(E + eV)] dE \quad (4.3.6)$$

, where Δ_1 and Δ_2 are the energy gaps of each superconductor electrodes, respectively. Similar qualitative analysis as in SIN junction above provides a schematic description of the current. At $T = 0$, to have a finite current, the chemical potential difference must provide enough energy to create a hole on one side, at the same time, create an electron on the other side. Hence, the required minimum energy to have a finite current is $e|V| \geq \Delta_1 + \Delta_2$.

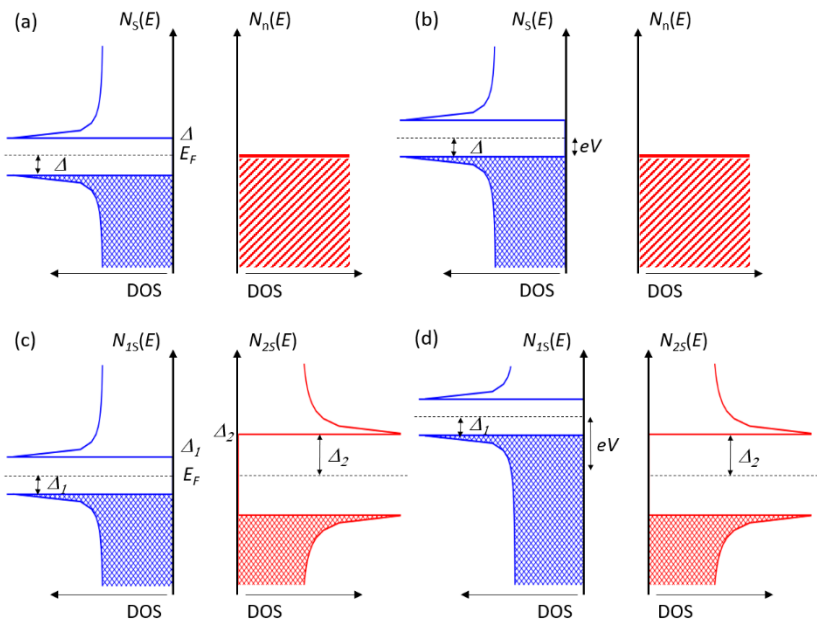

Figure 4.1: (a –b) Schematic tunneling between a superconductor and a normal metal. The filled area represents filled states. (c − d) Schematic tunneling between two superconductors.

4.3.2. Andreev Reflection

Andreev reflections is another type of charge-transfer process in Normal metal-Superconductor (NS) interface [86]. For energies below the superconducting gap Δ, an electron incident from the normal metal can't enter the superconductor because there are no quasiparticle states inside the gap. An electron, instead, is reflected back into the normal metal as a hole resulting production of a Cooper pair in the superconductor. The schematic process is described in Figure 4.2 (a). Andreev reflection occurs not only in NS interface but also is possible in SIS junction via Multiple Andreev Reflection (MAR) [15, 87].

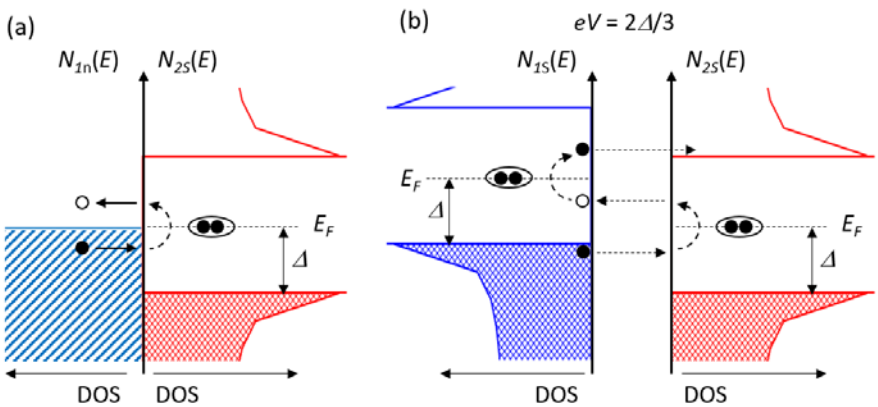

Figure 4.2: Schematic illustration of (a) Andreev reflection and (b) multiple Andreev reflection. The filled circles represent electrons while the open circles represent holes. Note that although electron and hole are drawn with non-zero energy for the clear visualization, the process can occur only near the Fermi energy (only at the Fermi energy when $T = 0$).

The schematic MAR process is illustrated in Figure 4.2 (b). When a bias voltage applied to the left superconducting electrode, an electron with energy eV incident from the left electrode arrives inside the gap of the right electrode causing Andreev reflection. Since a Cooper-

pair has zero kinetic energy, a retro-reflected hole will gain additional energy eV and this reflected hole again Andreev reflected at the left electrode. This process will be iterated until electron energy exceeds $\Delta_1 + \Delta_2$ so that it can enter the normal metal region. Thus, MAR will be shown as subharmonic gap structure at $eV = (\Delta_1 + \Delta_2) / n$ (n = 2, 3 ...).

4.4. Josephson Effect

4.4.1. Ideal Josephson Junction

In 1962, B. D. Josephson proposed a startling prediction about tunneling phenomena in SIS junction [88]. He assumed that superconducting order parameters of two superconducting electrodes can extend into the barrier and coupled in a weak link. As a result of phase coherence between two superconductors, pairs can tunnel through the barrier and flow of superfluid is made. This idea brought a huge controversy because, at the time, it is generally believed that the order parameter of superconductor can't be extended into the insulating barrier. However, as the experiments actually measured the supercurrent [89, 90], Josephson effect is firmly confirmed.

When two superconductors are uncoupled, the macroscopic wave functions of them are given by

$$\psi_1 = \sqrt{n_1} e^{i\theta_1}$$
$$\psi_2 = \sqrt{n_2} e^{i\theta_2} \qquad (4.4.1)$$

, where n is the superfluid density and θ is the phase. When two superconductors are coupled so that Cooper-pairs can be exchanged, the system is described by introducing the coupling constant K into the time-dependent Schrodinger equations:

$$\frac{\partial \psi_1}{\partial t} = -\frac{i}{\hbar}[E_1\psi_1 + K\psi_2]$$
$$\frac{\partial \psi_2}{\partial t} = -\frac{i}{\hbar}[E_2\psi_2 + K\psi_1] \qquad (4.4.2)$$

After substituting the wave functions into the Schrodinger equations and separating them into real part and imaginary part, we obtain

$$\frac{\partial n_1}{\partial t} = \frac{2K}{\hbar}\sqrt{n_1 n_2}\sin\phi$$
$$\frac{\partial n_2}{\partial t} = -\frac{2K}{\hbar}\sqrt{n_1 n_2}\sin\phi$$
$$\frac{\partial \theta_1}{\partial t} = -\frac{E_1}{\hbar} - \frac{K}{\hbar}\sqrt{\frac{n_2}{n_1}}\cos\phi$$
$$\frac{\partial \theta_2}{\partial t} = -\frac{E_2}{\hbar} - \frac{K}{\hbar}\sqrt{\frac{n_1}{n_2}}\cos\phi \qquad (4.4.3)$$

, where ϕ is the phase difference, $\theta_2 - \theta_1$. First two equations describe the supercurrent flow in the junction, thus, we obtain the current–phase relation,

$$I = I_C \sin\phi \qquad (4.4.4)$$

with the maximum or Josephson critical current $I_c = 2K\sqrt{n_1 n_2}$. On the other hand, from the third and fourth equations with $n_1 = n_2$, we obtain the voltage–phase relation,

$$\frac{\partial \phi}{\partial t} = \frac{E_1 - E_2}{\hbar} \equiv \frac{2eV}{\hbar} \qquad (4.4.5)$$

, where V is the voltage across the junction. As a result, for an ideal Josephson junction, where no dissipations present, supercurrent flows without any voltage drop, *i.e.*, zero bias current or conductance occurs.

Note that the Josephson critical current, I_C, is proportional to the

order parameters. Thus, measuring the quantity I_C will directly lead to the fundamental quantity, the superconducting order parameter, which provides the methodology of SJTM. Meanwhile, in order to measure I_C, knowing the current–voltage characteristic of Josephson junction is critical. As the voltage fully depends on the time evolution of the phase difference, identifying the phase dynamics is essential to predict the current–voltage characteristic of a junction.

Ambegaokar and Baratoff [91, 92] derived the exact temperature dependence of I_C for two identical superconductors:

$$I_C R_N = \frac{\pi\Delta}{2e}\tanh\left(\frac{\Delta}{2k_B T}\right) \tag{4.4.6}$$

, where R_N is the normal state resistance and k_B is the Boltzmann constant. Ambegaokar–Baratoff formula describes the temperature dependence of I_C, but at the same time, this formula connects the superconducting gap to the Josephson critical current. Especially, at low temperatures, Ambegaokar–Baratoff formula is reduced to a simpler form,

$$I_C R_N \approx \frac{\pi\Delta}{2e} \tag{4.4.7}$$

Thus, one can calculate the superconducting gap from I_C or vice versa.

Before proceeding, there are three key quantities in Josephson effect: Josephson critical current I_C, the phase–voltage relation and the Josephson coupling energy $E_J = \hbar I_C/2e$. As I_C is proportional to the superfluid density, I_C will be the key physical quantity. In order to measure I_C, we need to know the current–voltage characteristic of a junction, which is provided by the phase–voltage relation, that is, the dynamics of the phase. Finally, E_J is the characteristic energy of a junction, which competes with various fluctuations given in the system.

4.4.2. The RCSJ Model

In the last chapter, an ideal Josephson junction is discussed, where no dissipations exist. In reality, dissipations must be considered and the real Josephson junction is described by the Resistively and Capacitively Shunted Junction (RCSJ) model [15], shown in Figure 4.3. The resistance R represents dissipation channel from quasiparticle tunneling current while the capacitance C is shunting capacitance between two electrodes.

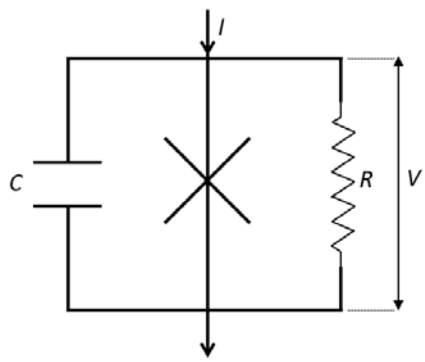

Figure 4.3: Lumped circuit diagram of RCSJ model. X represents an ideal Josephson junction.

In the presence of a bias current I, the equation of motion for the phase difference ϕ is

$$I = I_C sin\phi + \frac{V}{R} + C\frac{dV}{dt} \tag{4.4.8}$$

where I is a bias current and V is the voltage across the junction. By dividing both sides with I_C and exploiting the voltage−phase relation, equation 4.4.8 becomes

$$\frac{d^2\phi}{d\tau^2} + Q^{-1}\frac{d\phi}{d\tau} + sin\phi = \frac{I}{I_C} \tag{4.4.9}$$

, where $\tau = \omega_p t$, $\omega_p = (2eI_C/\hbar C)^2$ and $Q = \omega_p RC$. ω_p is called "Josephson

plasma frequency" of the junction and Q is "quality factor" of the junction. Note that under the condition where $\omega << 1$, equation 4.4.9 reduces to the form of a damped driven harmonic oscillator. Josephson plasma frequency, thus, corresponds to the oscillating frequency of the phase.

To capture the physical picture of RCSJ model intuitively, a mechanical analog, so-called "tilted washboard", provides the qualitative picture. In the tilted washboard model, a particle of mass $(\hbar/2e)^2C$ moving in an effective potential

$$U(\varphi) = -E_J cos\varphi - \left(\frac{\hbar I}{2e}\right)\varphi \qquad (4.4.10)$$

together with viscous drag force $(\hbar/2e)^2(1/R)\,d\phi/dt$. The equation of motion of a particle under this circumstance is equal to the equation 4.4.9, hence the dynamics of a particle equivalent to the dynamics of the phase. The effective potential consists of a cosine term and a linear term. Cosine term forms a potential barrier preventing a particle from advancing. On the other hand, a linear term tilts the potential, at the same time, reducing a potential barrier allowing a particle to move.

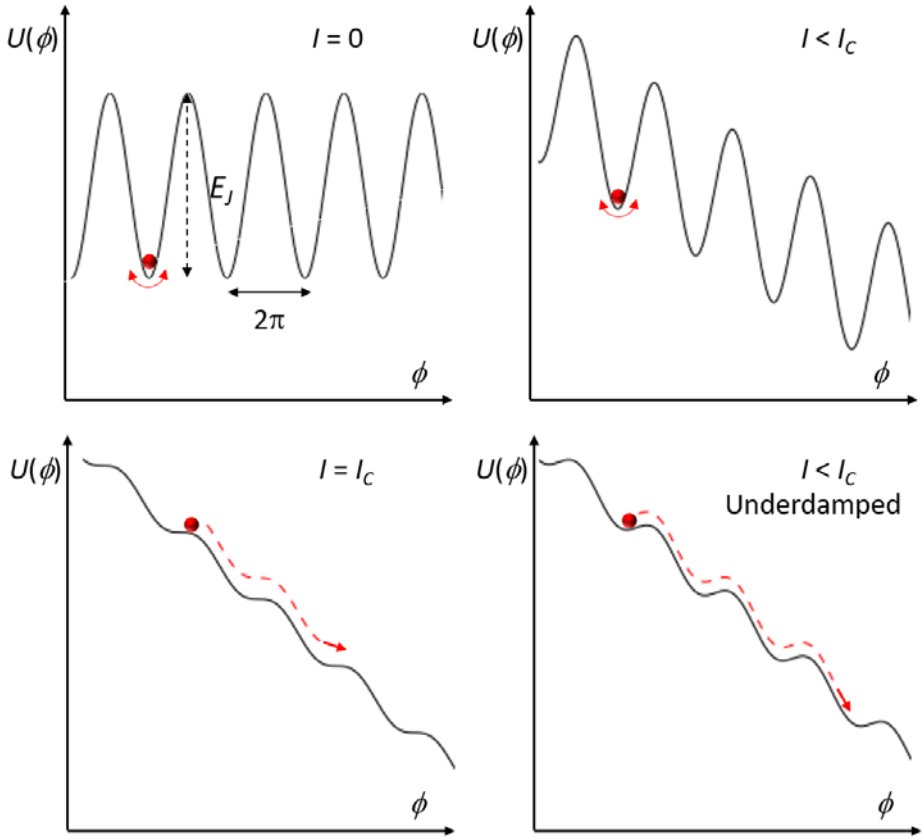

Figure 4.4: Illustration of the tilted washboard potential for the different bias currents. As the bias current is increased from (a) $I = 0$, (b) $I < I_C$ and (c) $I = I_C$, the potential barrier height becomes less and finally, the particle (phase) starts to advance. (d) For an underdamped case, the particle continues to move down even for $I < I_C$ when the bias current is reduced from $I > I_C$.

As an example, let's consider zero bias current. In this case, the effective potential is a simple cosine and the particle will just stay in the minimum of the potential giving zero voltage. Similarly, the particle will rest in the minimum in the potential until bias current becomes equal to I_C. When bias current equals or exceeds I_C, there are no cosine minima for the particle to find a stable equilibrium, consequently, the particle will continuously slide down and a finite voltage will show up.

On the other hand, the quality factor Q describes the damping of the system. If $Q >> 1$ and C is large, the system is underdamped. Starting from $I = 0$, zero voltage state is maintained until $I = I_C$ and a finite voltage occurs for $I >= I_C$. However, ramping down the current from $I > I_C$ works differently, in other words, the system is hysteretic. When $I > I_C$, due to the heavy tilting, the particle moves down along the potential. In order to recover the zero voltage state, this "running" particle has to be retrapped in the potential minimum. However, since the system is underdamped, the particle will keep running until the potential is sufficiently tilted back to horizontally. Consequently, zero bias state will be recovered at a "retrapping current", which is essentially smaller than I_C and resulting in a hysteretic current–voltage characteristic.

If $Q << 1$, the system is overdamped as C is small and the viscous drag force dominates its dynamics. Unlike the underdamped case, heavy damping almost stops the particle as soon as $I \leq I_C$ so that the particle can be retrapped in the potential minima. Hence, no hysteresis occurs in an overdamped junction.

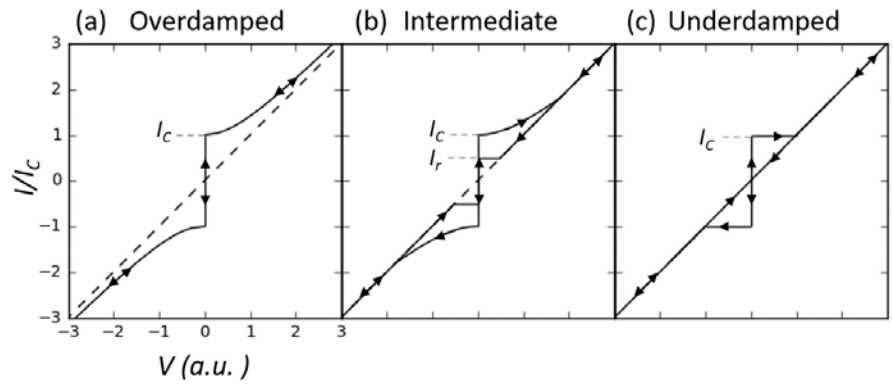

Figure 4.5: Current−voltage characteristics of Josephson junction with (a) Overdamping, (b) intermediate damping and (c)underdamping. The direction of current variations is indicated by arrows. I_r represents the retrapping current.

4.4.3. Thermal Fluctuations

In the last two sections, the current−voltage characteristic of Josephson junction is described starting from an ideal junction and expanded to the more realistic RCSJ mode. These two models considered definite phase, *i.e.*, no phase fluctuations. The subsequent sections will consider the phase fluctuation effects from thermal fluctuations and quantum fluctuations.

Here, I'll expand the RCSJ model by introducing thermal fluctuations from the environment, such as leads on the junction. Formally, thermal fluctuations are introduced as a Johnson noise in the circuit, however, thermal activations in the tilted−washboard model provide a physical picture as well. Although thermal energies try to activate the particle in the potential minima, fluctuation effects won't be prominent until thermal energies are sufficiently large to

excite the particle to surmount the barrier. Imagine a particle in a stable state in the potential minima. Small thermal energies only give a phase fluctuation near the equilibrium results in $\langle\phi\rangle = 0$. On the other hand, thermal energies large enough so that a particle can escape to the next minimum, which will affect the dynamics of the particle.

In an underdamped system, small fluctuations still can render the dynamics of the particle. If $k_B T << E_J$ with zero bias current, the probability that thermal fluctuations excite the particle to the next minimum is small as $\exp(-\Delta U/k_B T)$. Applied bias current will tilt the potential, that is, lower barrier height, and provides a higher escaping probability. Analogous to the underdamping RCSJ model, once the particle surmounts the barrier, the particle will be in a running state without retrapped in the minima. As a result, the critical current is reduced and a premature switching to a finite voltage state occurs.

Now, let's start from the current bigger than I_C. We know that in the underdamped system, zero voltage state is recovered at a retrapping current, $I_r < I_C$. At $I = I_r$ without fluctuations, the particle continuously moves down without being retrapped in the minimum. As we turn on thermal fluctuations, downward fluctuations deflect the particle trajectory toward the minimum making it be retrapped in the minimum. Upward fluctuations increase the energy of the particle, however, dissipations bring it back rapidly to original trajectory. This is because while the increase of energy is proportional to a voltage V as $V \propto d\phi/dt$, dissipations described by $\sim V^2/R$ outweighs. Hence, thermal energies increase a retrapping current while the critical current is reduced.

In an overdamped system, thermal fluctuations fundamentally change its current–voltage characteristic. As in the underdamped system, when thermal energies are sufficiently large the particle can advance to the next minimum. However, heavy damping will retrap the particle into the minimum until it is excited again to move to the

next minimum. This will repeatedly happen and the particle continuously “diffuses” over the barrier resulting in a finite voltage state below I_C. This regime is called “phase diffusion regime”.

4.4.4. Ultra-Small Josephson Junction I

The discussion so far is in the classical limit. When the size of a junction becomes small, then the capacitance of the junction is concomitantly small (order of fF). This small capacitance causes fundamental changes.

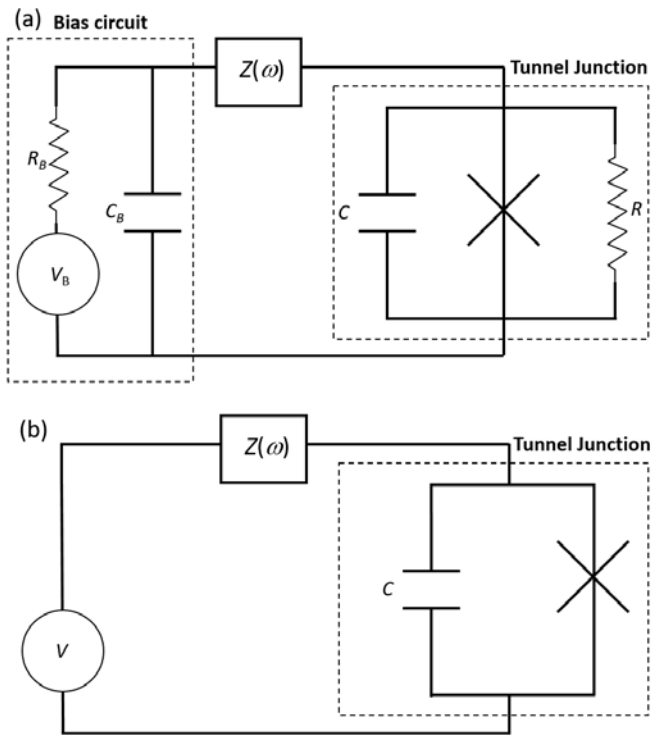

Figure 4.6: (a) The current biased circuit model with the environment including the bias circuit and the impedance, $Z(\omega)$. (b) The bias circuit in (a) is replaced by a voltage source in series with the impedance, $Z(\omega)$.

In the RCSJ model, an ideal current source is assumed, which has an infinite impedance for all frequencies except DC frequency. In addition, the electromagnetic environment of the junction, which includes electronics and the electrical leads connected down to the junction, has not been considered. Meanwhile, for a small capacitance, the phase dynamics set by the Josephson plasma frequency typically has a high characteristic frequency order of 10^{11} Hz. At these high frequencies, the shunting DC resistance R in the junction plays no role and the damping of the junction is dominated by the impedance of the environment. Thus, to incorporate the dynamic nature of the junction, the assumed ideal current source needs to be replaced with detailed environment model. The bias circuit can be modeled with a voltage source V_B in series with a DC resistor R_B and a parasitic capacitance C_B. The bias circuit takes account for the low-frequency response of the environment. To take account for the high-frequency response of the environment, an impedance $Z(\omega)$ is placed in series with the bias circuit. The corresponding circuit is shown in Figure 4.6 (a). This circuit model can be further simplified owing to the high-frequency nature of the junction. [93, 94] First, the DC bias resistance, R_B, can be omitted at high frequencies. In addition, since the parasitic capacitance, C_B, is typically much larger than the junction capacitance, C, the voltage across the capacitance C_B can be approximated as time independent. Hence, the bias circuit model in Figure 4.6 (a) can be replaced by a voltage source in series with the high-frequency impedance $Z(\omega)$, as shown in Figure 4.6 (b). After all, the current biased junction can be effectively described as a voltage biased junction.

On the other hand, the high-frequency impedance, $Z(\omega)$, can be approximated as an infinite transmission line. [93-97] Since the radiation phenomena dominating the impedance has a wavelength of an order of a millimeter, only a few millimeters of the leads are relevant. Thus, the impedance as seen from the junction will be an order of free space, $Z_1 \sim Z_0/2\pi \sim 100\ \Omega$, where $Z_0 \sim 377\ \Omega$ is the free space impedance. [93-97] Note that at these high frequencies, as

the junction resistance R plays no role, the damping is dominated by the low environment impedance. Therefore, the junction will be always overdamped irrelevant to the junction resistance R. As seen in the previous section, the overdamped junction in the presence of large thermal fluctuations will be in the phase diffusion regime. The analytic solution of the phase diffusion model is found by Ivanchenko and Zil'berman [98] namely the phase diffusion model. (Later, Ingold *et al.* [99] independently derived the same result by treating the Josephson effect quantum mechanically.) They considered a circuit model in Figure 4.6 (b) with an ohmic impedance, $Z(\omega) = Z$, and introduced thermal fluctuation to the junction by assuming that the ohmic impedance in thermal equilibrium at temperature T gives rise to Johnson noise. The equation for the phase is then, [98, 100]

$$C\frac{\mathrm{d}^2\phi}{\mathrm{d}t^2}+\frac{1}{Z}\frac{d\phi}{dt}+\frac{2e}{\hbar}I_C sin\phi=\frac{2e}{\hbar}\frac{V_0+V(t)}{Z} \tag{4.4.11}$$

, where V_0 is the voltage supplied by the voltage source and $V(t)$ is the stochastic voltage noise across the junction, which is assumed to be frequency independent. In the limit where $C \rightarrow 0$, the analytic solution of the corresponding Fokker–Planck equation can be found as [98, 100]

$$\frac{I}{I_C}=Im\left(\frac{I_{1-i\beta E_J v}(\beta E_J)}{I_{1-i\beta E_J v}(\beta E_J)}\right) \tag{4.4.12}$$

, where $I_n(z)$ is the modified Bessel function, $\beta = 1/k_B T$ and $v = V/RI_C$ is the dimensionless applied voltage. In the case, for $E_J << k_B T$, the current–voltage characteristic becomes

$$I(V)=\frac{I_C^2 Z_1}{2}\frac{V}{V^2+V_P^2} \tag{4.4.13}$$

, where $V_P = 2eZ_1 k_B T/\hbar$. The current–voltage characteristics are plotted in Figure 4.7 (a). Thermal fluctuations give rise to the finite

resistance at zero bias. In the experimental view, this functional form is favorable. Current−voltage characteristic exhibits a current peak and the current peak occurring at the voltage V_P is

$$I(V = V_P) = \frac{I_C^2 Z_1}{4V_P} \propto I_C^2 \tag{4.4.14}$$

Thus, measuring a current peak in the current−voltage characteristic is equivalent to measuring physically important I_C. The occurrence of a current peak can indicate the formation of Josephson junction, which is experimentally identifiable and advantageous. Alternatively, dI/dV (V) can be exploited which is plotted in Figure 4.7 (b). dI/dV (V) exhibits zero bias conductance peak:

$$\frac{\mathrm{d}I}{dV}(V = V_P) = \frac{I_C^2 Z_1}{2V_P^2} \propto I_C^2 \tag{4.4.15}$$

Similarly, measuring the zero bias conductance peak leads to I_C and identifies the formation of Josephson junction.

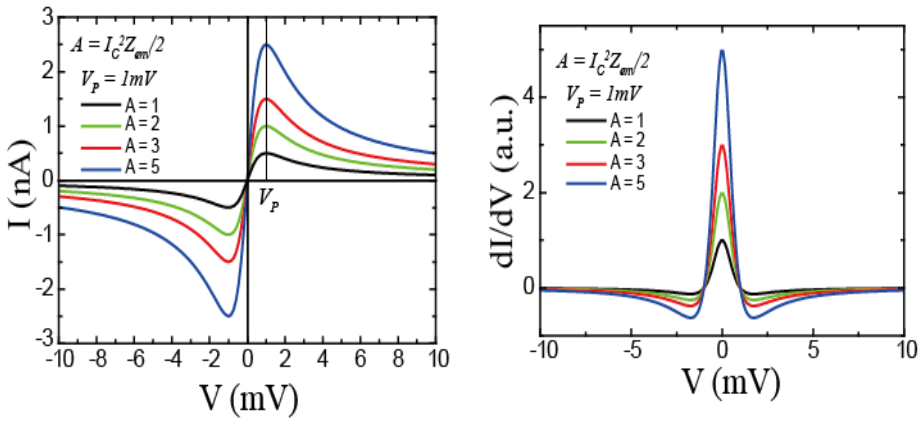

Figure 4.7: (a) Current−voltage characteristics of the phase diffusion model. (b) dI/dV spectra of the phase diffusion model.

4.4.5. Ultra−small Josephson junction II: Incoherent Pair−Tunneling

The Josephson junction hitherto has been treated classically, where the phases of the superconductors are well−defined. However, a small capacitance brings quantum fluctuations in the phase. Phase ϕ and particle number N are conjugate variables and have the uncertainty relation

$$\Delta N \Delta \varphi \gtrsim 1 \tag{4.4.16}$$

In the system with a small particle number fluctuation, the phase fluctuation becomes large and the phase of a superconductor is no longer be well−defined. In the ultra−small Josephson junction, where the charging energy $E_C = 2e^2/C$ is the dominant fluctuation, Coulomb blockade occurs. Consequently, the particle number fluctuation becomes greatly diminished and the system can't be treated classically. However, if the thermal fluctuation is the dominant energy, then the capacitive effect is averaged out and the system will be brought back to the classical system. Thus, the description of an ultra−small Josephson junction is determined by three characteristic energy scales: thermal energy, charging energy and Josephson coupling energy.

To explicitly show the quantum mechanical effect, consider an isolated Josephson junction at $T = 0$. The total energy of the junction is

$$E = -E_J cos\phi + \frac{1}{2}CV^2 = -E_J cos\phi + \frac{1}{2}C\left(\frac{\hbar}{2e}\right)^2\left(\frac{d\phi}{dt}\right)^2 \tag{4.4.17}$$

Here no dissipation is assumed, which can be justified because the junction resistance is typically high, thus quasiparticle tunneling is negligible. By defining $\hat{N}$ as a pair number operator and replacing the charge Q with $Q/2e = N \rightarrow i\,\partial/\partial\phi$, the Hamiltonian can be written as

$$H = -E_J cos\phi - 4E_C \frac{\partial^2}{\partial \phi^2} \tag{4.4.18}$$

For a system having $E_J >> E_C$, E_C in the Hamiltonian is negligible, hence ϕ is a good quantum number. Consequently, Josephson junction is described by the phase diffusion model in the previous section. Note that as the phase is well-defined, the pair-tunneling current in this regime is coherent pair-tunneling.

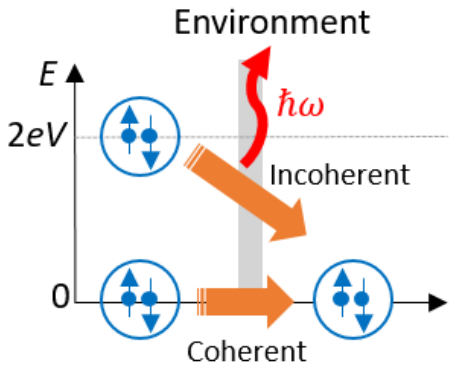

Figure 4.8: Schematic illustration of coherent and incoherent pair-tunneling. While coherent pair-tunneling occurs at zero bias voltage, incoherent pair-tunneling emits radiation to the environment.

On the other hand, for a system having $E_C >> E_J$, particle number is a good quantum number and the phase will suffer a large fluctuation. Since the phase is not well-defined and both superconductors have an identical constant number of Cooper-pairs N to minimize a charging energy, coherent pair-tunneling is no longer possible. In this case, the pair-tunneling process will happen only by an inelastic process. Suppose that Cooper-pair tunneling happens. The number of pairs in each superconductor will be $(N+1)$ and $(N-1)$, which will increase the charging energy corresponding to charge 2e,

$$\Delta E_C = \frac{2e^2}{C} \cdot 2e \tag{4.4.19}$$

To compensate this increase of a charging energy, a voltage V across the junction needs to be applied. On the other hand, since a Cooper-pair can't have a kinetic energy, the extra energy $2eV$ provided to a Cooper-pair needs to be emitted and absorbed by the environment. This inelastic pair-tunneling process is called incoherent pair-tunneling. As the tunneling process should be accompanied by the interaction between the environment and the junction, the dissipative environment necessarily considered in formulating the incoherent pair-tunneling. The incoherent pair-tunneling is formally described by the $P(E)$-theory developed by Ingold *et al.* [93, 99, 100]

Caldeira and Legget [101] formulate the dissipative environment microscopically as an infinite set of LC-circuits of capacitors C_n and inductors L_n. The corresponding Hamiltonian for the environment is given by [94, 99]

$$H_{env} = \sum_{n=1}^{\infty} \left[\frac{q_n^2}{2C_n} + \left(\frac{\hbar}{e}\right)^2 \frac{1}{2L_n} \left(\frac{\phi}{2} - \frac{e}{\hbar} Vt - \phi_n \right)^2 \right] \tag{4.4.20}$$

, where V is the external voltage. Introduce the environment Hamiltonian to the junction, then the Hamiltonian for the Josephson junction is

$$H = \frac{Q^2}{2C} - E_J \cos\phi + H_{\text{env}} \tag{4.4.21}$$

To have the incoherent pair-tunneling, the charging energy must significantly exceed the Josephson coupling energy. In this limit, the E_J term in the Hamiltonian can be treated perturbatively. The tunneling rate is calculated by applying Fermi's golden rule:

$$\Gamma_{i\to f} = \frac{2\pi}{\hbar} |< f| - E_J cos\phi |i>|^2 \delta\left(E_f - E_i\right) \tag{4.4.22}$$

, where $|i>$ and $|f>$ are the initial state and the final state,

respectively and they are the total states as a product of a quasiparticle state and a charge state coupled to the environment. After tracing out the environmental states, the forward tunneling rate is given by [94, 99]

$$\vec{\Gamma}(V) = \frac{E_J^2}{4\hbar^2}\int_{-\infty}^{\infty} dt \exp\left(i\frac{2e}{\hbar}Vt\right) < e^{i\phi(t)}e^{-i\phi(0)} > \tag{4.4.23}$$

The last term in the integrand, $< e^{i\phi(t)}e^{-i\phi(0)} >$, is called the phase correlation function. This measures the change of the phase coherence caused by the pair-tunneling. The correlation function for an arbitrary impedance can be evaluated as

$$J(t) = 2\int_{-\infty}^{\infty} \frac{d\omega}{\omega}\frac{ReZ_t(\omega)}{R_Q}\frac{e^{-i\omega t}-1}{1-e^{-\beta\hbar\omega}} \tag{4.4.24}$$

, where $R_Q = h/4e^2$ is the resistance quantum and $Z_t(\omega)$ is the total impedance given by

$$Z_t(\omega) = \frac{1}{i\omega C + Z^{-1}(\omega)} \tag{4.4.25}$$

By taking advantage of $J(t)$, the forward tunneling rate can be rewritten as

$$\vec{\Gamma}(V) = \frac{\pi E_J^2}{2\hbar^2}P(2eV) \tag{4.4.26a}$$

$$P(E) = \frac{1}{2\pi\hbar}\int_{-\infty}^{\infty} dt\, exp\left[J(t) + \frac{i}{\hbar}Et\right] \tag{4.4.26b}$$

The forward tunneling rate is proportional to $P(E)$, which indicates that $P(E)$ is the probability that a Cooper-pair tunneling occurs with the emission of energy E. As discussed above, the incoherent pair tunneling requires external voltage, V, to overcome the change of charging energy. The total tunneling current is then

$$I(V) = 2e\left[\vec{\Gamma}(V) - \overleftarrow{\Gamma}(-V)\right] = \frac{\pi e E_J^2}{\hbar}\left[P(2eV) - P(-2eV)\right] \qquad (4.4.27)$$

To predict the actual current−voltage characteristic in an experiment, the spectral probability $P(E)$ needs to be calculated. The full details of total impedance in the $J(t)$ are difficult to calculate, however, we have seen that the environment impedance can be approximated as an ohmic impedance, Z_1. Under this assumption, for low temperature and low voltages, the current−voltage characteristic is evaluated to [100]

$$I(V) = \frac{\pi}{2} I_C \frac{E_J}{E_C} \rho^{2\rho} \left(\frac{E_C}{2\pi^2 k_B T}\right)^{1-2\rho} e^{-2\gamma\rho} \frac{|\Gamma(\rho - i(eV/\pi k_B T)|^2}{\Gamma(2\rho)} \sinh\left(\frac{eV}{k_B T}\right) \qquad (4.4.28)$$

, where $\rho = Z_1/R_Q$, γ is Euler's constant and $\Gamma(x)$ is the Gamma function. This current−voltage characteristic is plotted in Figure 4.9. The maximum current can be found from the current−voltage characteristic [100]:

$$I_{Max} = \frac{\pi}{2} I_C \frac{E_J}{E_C} \rho^{2\rho} \left(\frac{E_C}{2\pi^2 k_B T}\right)^{1-2\rho} \exp(-2Z_1\rho) \sinh(\pi\rho) \frac{|\Gamma(\rho(1-i)|^2}{\Gamma(2\rho)} \propto I_C^2 \qquad (4.4.29)$$

The current peak is directly proportional to the Josephson critical current as in the phase diffusion model.

One can notice that the current−voltage characteristics of the phase diffusion model and $P(E)$−theory are overall very similar. They both exhibit a finite resistance at zero bias with current peak proportional to the square of the Josephson critical current. This implies although the physical origin of the fluctuations is quite different, they can be bridged. Indeed, Grabert and Ingold [100] showed that they can be smoothly bridged by properly renormalizing the Josephson coupling energy.

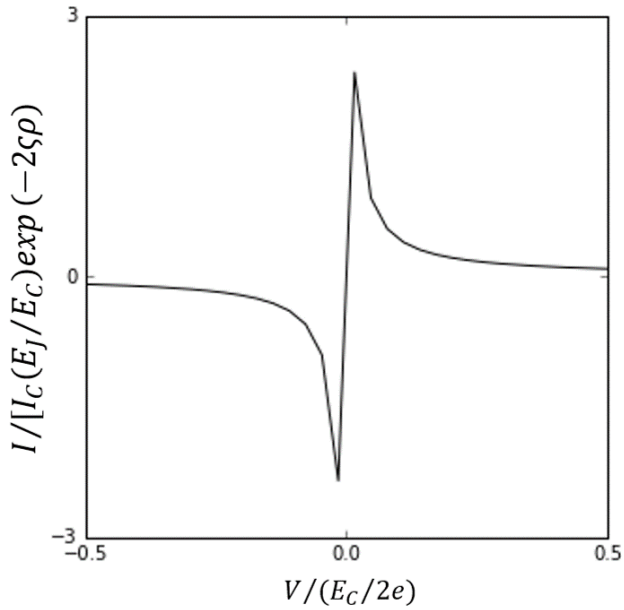

Figure 4.9: Current−voltage characteristic calculated from equation 4.4.28 in the main text. The current peak is proportional to the square of the Josephson critical current.

In summary, the dynamics of the Josephson effect is characterized by three quantities: E_J, E_C, and k_BT. In the limit, where $k_BT > E_J > E_C$, the phase diffusion model describes the current−voltage characteristic as plotted in Figure 4.7. On the other hand, in the limit, where $E_C > k_BT > E_J$, the $P(E)$−theory describes the current−voltage characteristic as plotted in Figure 4.9.

4.5. Technical Aspects.

4.5.1. Tip Fabrication

Tip fabrication is the most crucial, but the challenge in the realization of SJTM. For a successful SJTM, a tip has to meet several requirements.

First and foremost, a tip has to be a superconductor to form a Josephson junction. In the previous SJTM studies used conventional superconductors, Pb, Al and MgB_2 as a superconducting material for a tip. [82-85]

Second, a superconducting tip is better to have a larger gap. According to the Ambegaokar-Baratoff formula [91, 92], a large gap in a superconducting tip equals to a large I_CR_N value. A large I_CR_N value provides a large I_C, which makes easier to resolve, at the same time, a higher R_N, which provides a more stable tip-sample junction. In the experimental view, this condition is very crucial, especially in high temperatures as the R_N needs to be very small.

Last but not least, in order to study cuprates, which have a *d*-wave order parameter symmetry, a *d*-wave superconducting tip is preferable. Assuming a tip is an *s*-wave superconducting tip, a convolution between a *d*-wave order parameter in a sample and an isotropic order parameter of a tip will result in a zero current.

Conventionally a superconducting tip is fabricated *ex-situ* and transferred to STM head for SJTM. This method may provide better control of the tip, however, it requires a change of a tip from a normal metal for STM measurements. Depending on a design of STM, this may take a few days or even require a warmup the whole system. Furthermore, a more crucially, to satisfy the third condition, the choice of the material for a tip has to be *d*-wave superconductor, which is impossible to fabricate as a sharp tip.

We took an alternative method to fabricate a superconducting tip satisfying all conditions above. When a normal metal tip, typically tungsten, approaches to a $Bi_2Sr_2CaCu_2O_{8+x}$ sample, a tip can pick up a nanometer-sized flake of $Bi_2Sr_2CaCu_2O_{8+x}$ sample, forming a $Bi_2Sr_2CaCu_2O_{8+x}$-tip. The $Bi_2Sr_2CaCu_2O_{8+x}$-tip has several advantages. Obviously, it has a *d*-wave order parameter with a large gap, as $Bi_2Sr_2CaCu_2O_{8+x}$ usually has a gap (> 10 meV) for all doping

range. In addition, since the flake is picked up from the sample surface without any rotation, it is reasonable to assume that the phase of order parameter in tip and sample is identical. This will maximize the Josephson critical current. The tip is fabricated *in-situ*, the tip doesn't need to be replaced, providing, in principle, a chance to study the same surface with a normal metal tip and a superconducting tip.

However, one caveat of this method is that the *in-situ* tip fabrication is not easy. There is always a possibility that a tip changed to other than a superconducting tip. Indeed, during the tip fabrication, occasionally, one can see a tip showing the spectroscopic evidence of superconducting but with lack of imaging capability or vice versa. Empirically, when a normal metal tip in a good condition, which can produce good conventional STM data, is prone to be a stable $Bi_2Sr_2CaCu_2O_{8+x}$-tip.

4.5.2. Ultra-Low vibration

The barrier thickness of a Josephson junction, in SJTM, tip-sample distance should be extremely small, especially at 4.2 K. In addition, since tunneling current varies exponentially with respect to tip-sample distance, with a tip close to a sample, a small fluctuation of a tip-sample distance results in a huge current fluctuation. Thus, SJTM requires a stable junction, that is, ultra-low vibration system. With an aid of ultra-low vibration isolation system as explained in Chapter 3, we could achieve sufficiently low vibration.

4.5.3. Characterization of $Bi_2Sr_2CaCu_2O_{8+x}$-tip.

$Bi_2Sr_2CaCu_2O_{8+x}$-tip is fabricated by applying a voltage pulse (-2 V ~ 2 V) or extending z piezoelectric tube very close to the sample. As mentioned above, this process may require many attempts and sometimes tip has to be re-prepared by field-emission technique.

Having *in-situ* field emission stage, described in Chapter 3, enables us to fabricate the tip without discarding sample for the field emission and to recover back to a normal metal tip whenever it is needed.

A superconducting tip in SJTM experiments provides its unique characters differing from those of conventional STM experiments using a normal metal tip. Since a $Bi_2Sr_2CaCu_2O_{8+x}$-tip inherits spectral characters from a $Bi_2Sr_2CaCu_2O_{8+x}$ sample, the resulting current is a convolution of the density of states of tip and sample. Moreover, the apex of the tip is no longer characterized as a single atom but has a spatial structure of $Bi_2Sr_2CaCu_2O_{8+x}$. Consequently, resulting topographic images are again a convolution of the spatial structures of tip and sample. These characters are important to characterize and verify the proper fabrication of $Bi_2Sr_2CaCu_2O_{8+x}$-tip.

The characterization of a tip is achieved in two ways. First, by taking topographic images, one can check the tip's ability to resolve atoms. As explained above, since resulting topographic images are the convolution of the spatial structures of tip and sample, local crystalline imperfections, such as lattice vacancies, may absent in the images.

On the other hand, the shift of coherence peaks in spectra provides a more definite character of a $Bi_2Sr_2CaCu_2O_{8+x}$-tip. In Chapter 4, I have shown that for an SIS junction, the presence of gaps in both electrodes shifts the location of coherence peaks to $\Delta_1+\Delta_2$. The verification of this shift will provide not only verification of actual fabrication of $Bi_2Sr_2CaCu_2O_{8+x}$-tip, but also estimation of the gap of a $Bi_2Sr_2CaCu_2O_{8+x}$-tip.

5. Scanning Josephson Tunneling Microscopy at 4.2 K

5.1. Introduction

It is now widely accepted that the pseudogap and the superconducting gap in cuprates are distinct as discussed in Chapter 2. Moreover, there is compelling experimental evidence that the pseudogap not only presents above T_C but also coexists with superconducting phase below T_C. [43, 45, 55, 68] In spectroscopic measurement in k-space, such as ARPES and Raman spectroscopy, can distinguish pseudogap and superconducting gaps below T_C, as they live in different locations in k-space, anti-node and node, respectively. However, conventional STM utilizing a normal metal tip measures single-particle excitations in r-space causing ambiguity in the measurement of the pseudogap and the superconducting gap in r-space. In contrast to conventional STM, SJTM is able to probes the superconducting order parameter directly. [82-85] We utilize SJTM technique on overdoped $Bi_2Sr_2CaCu_2O_{8+x}$-tip (T_C ~ 60 K) to reveal the r-space structure of the superconducting gap. Meanwhile, SJTM experiments hitherto are performed between 20 mK ~ 1 K [82-85] providing only a narrow window of temperature. We performed SJTM at 4.2 K to expand the window.

5. 2. Characterization of a $Bi_2Sr_2CaCu_2O_{8+x}$-tip.

As a $Bi_2Sr_2CaCu_2O_{8+x}$-tip is fabricated *in-situ*, the tip needs to be characterized. The characterization of a $Bi_2Sr_2CaCu_2O_{8+x}$-tip is done by measuring topographic images and differential conductance spectra.

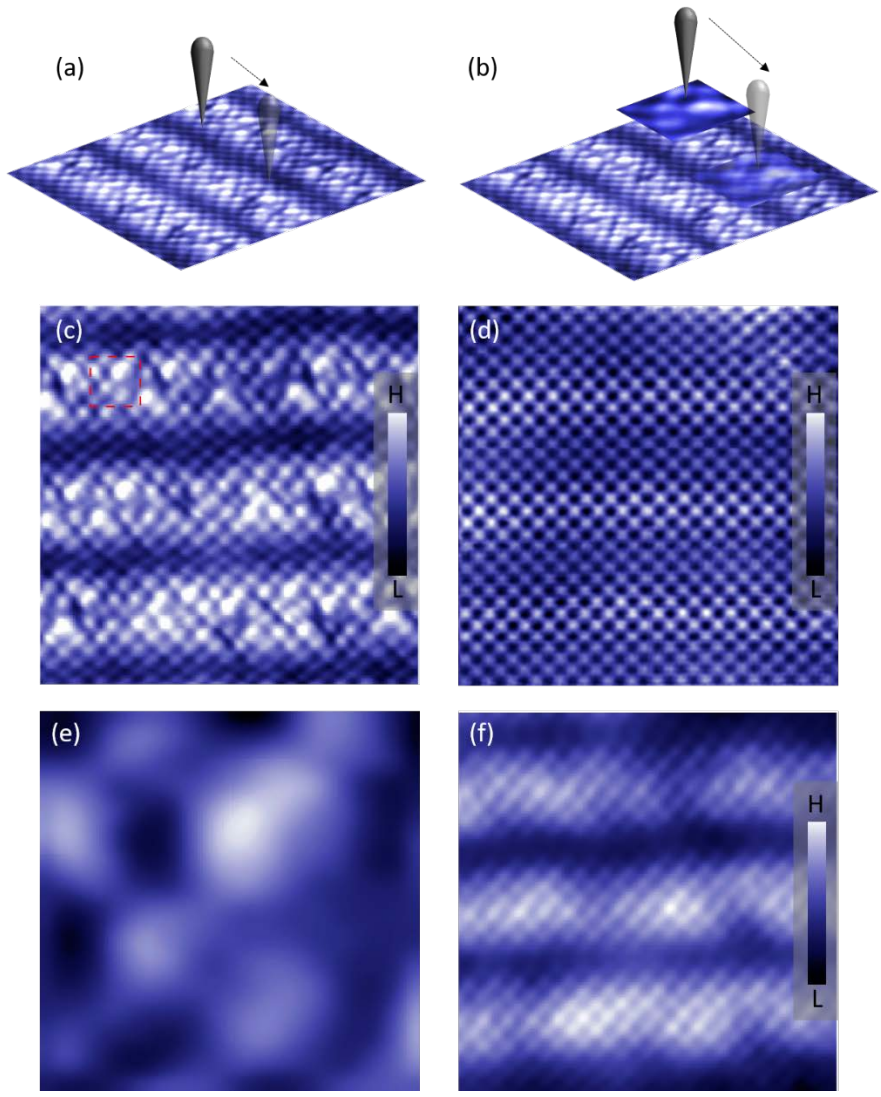

Figure 5.1: (a – b) Cartoons illustrate (a) STM operation with a normal metal tip and (b) SJTM operation with in-situ fabricated $Bi_2Sr_2CaCu_2O_{8+x}$-tip. (c) Topographic image of $Bi_2Sr_2CaCu_2O_{8+x}$ measured by a tungsten tip. (d) Topographic image of $Bi_2Sr_2CaCu_2O_{8+x}$measured by a $Bi_2Sr_2CaCu_2O_{8+x}$-tip. (e) Assume that a tungsten tip picks up a nanometer-sized flake from the surface shown in (c) (dashed red box in(c)). Thus, the topographic image of this $Bi_2Sr_2CaCu_2O_{8+x}$-tip will be identical to the dashed red box in (c). (f) SIS topographic image is simulated by convolution of topographic images in (c) and (e), representing sample surface and tip, respectively.

Figure 5.1 (c) and (d) show the topographic images taken with a tungsten tip and a $Bi_2Sr_2CaCu_2O_{8+x}$–tip, respectively. Atomic corrugations, supermodulations and lattice mismatches are clearly observed in the SIN topographic image (Figure 5.1 (c)) as expected. SIS topographic image (Figure 5.1 (d)) clearly shows atomic corrugations and supermodulations while local lattice structures, such as lattice mismatches, are missing.

SIS topographic image can be understood from a simple simulation. A $Bi_2Sr_2CaCu_2O_{8+x}$–tip is fabricated by picking up a small flake of a sample, thus, the topographic image of a $Bi_2Sr_2CaCu_2O_{8+x}$–tip would be identical to a part of a topographic image of a sample. Figure 5.1 (e) shows an assumed topographic image of a $Bi_2Sr_2CaCu_2O_{8+x}$–tip, which is taken from the dashed red box in Figure 5.1 (c). An SIS topographic image is a convolution between the SIN topographic images of tip and sample, a simulated SIS topographic image is generated by convoluting Figure 5.1 (c) and (e) as depicted in Figure 5.1 (f). Because of the finite size of a tip, local lattice structures are missing, however, atomic corrugations and lattice supermodulations persist. Thus, this simulation shows that even though a $Bi_2Sr_2CaCu_2O_{8+x}$–tip is not a single atom–size tip, nanometer resolution can be achieved. Comparing the simulation with the measured SIS topographic image in Figure 5.1 (d) verifies measured SIS topographic images are actually measured from a $Bi_2Sr_2CaCu_2O_{8+x}$–tip. The characteristic of a $Bi_2Sr_2CaCu_2O_{8+x}$–tip is retained in a large field of view topographic image shown in Figure 5.2.

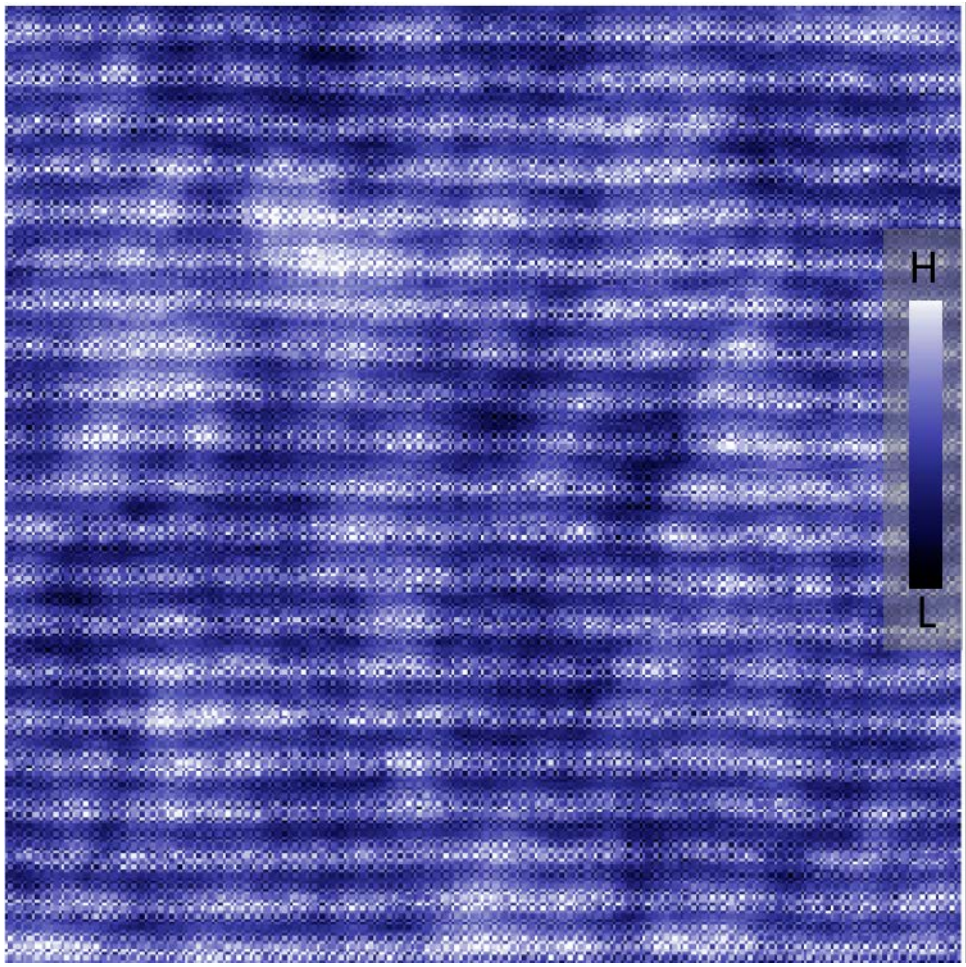

Figure 5.2: 60 nm x 60 nm field of view topographic image of $Bi_2Sr_2CaCu_2O_{8+x}$ measured by $Bi_2Sr_2CaCu_2O_{8+x}$–tip.

Another important characterization of a $Bi_2Sr_2CaCu_2O_{8+x}$−tip is performed by measuring the differential conductance spectra. While the density of states of a tungsten tip is assumed to be a constant over the energy, the density of states of a $Bi_2Sr_2CaCu_2O_{8+x}$−tip has a gap with V−shaped dispersion inside the gap. The single−particle tunneling current in SIS junction is already derived in the previous Chapter 4 and is given by

$$I_{\mathrm{SIS}} = |T|^2 \int_{-\infty}^{\infty} N_S(E) N_T(E+eV)[f(E) - f(E+eV)]dE \qquad (5.2.1)$$

Here, subscription S and T represent sample and tip, respectively. The Fermi−Dirac distribution function can be approximated as a step function and by differentiating the resulting current, we obtain the differential conductance in SIS junction:

$$g(V) = \frac{dI}{dV}(V) = |T|^2 \left[N_S(E) N_T(E+eV) + \int_0^{eV} N_S(E) \frac{\partial N_T(E+eV)}{\partial (eV)} dE \right] \qquad (5.2.2)$$

Figure 5.3 demonstrates the density of states model for SIN (tungsten tip) and SIS ($Bi_2Sr_2CaCu_2O_{8+x}$−tip) junction and corresponding normalized differential conductance spectra. The presence of coherence peaks in the density of states of $Bi_2Sr_2CaCu_2O_{8+x}$−tip, coherence peak will appear when the bias voltage, eV, coincides with $\Delta_S + \Delta_T$, where Δ_S (Δ_T) is the energy separation between coherence peaks in the sample (tip). Hence, the observation of an increase in the energy separation between coherence peaks is good evidence that tip is actually superconducting.

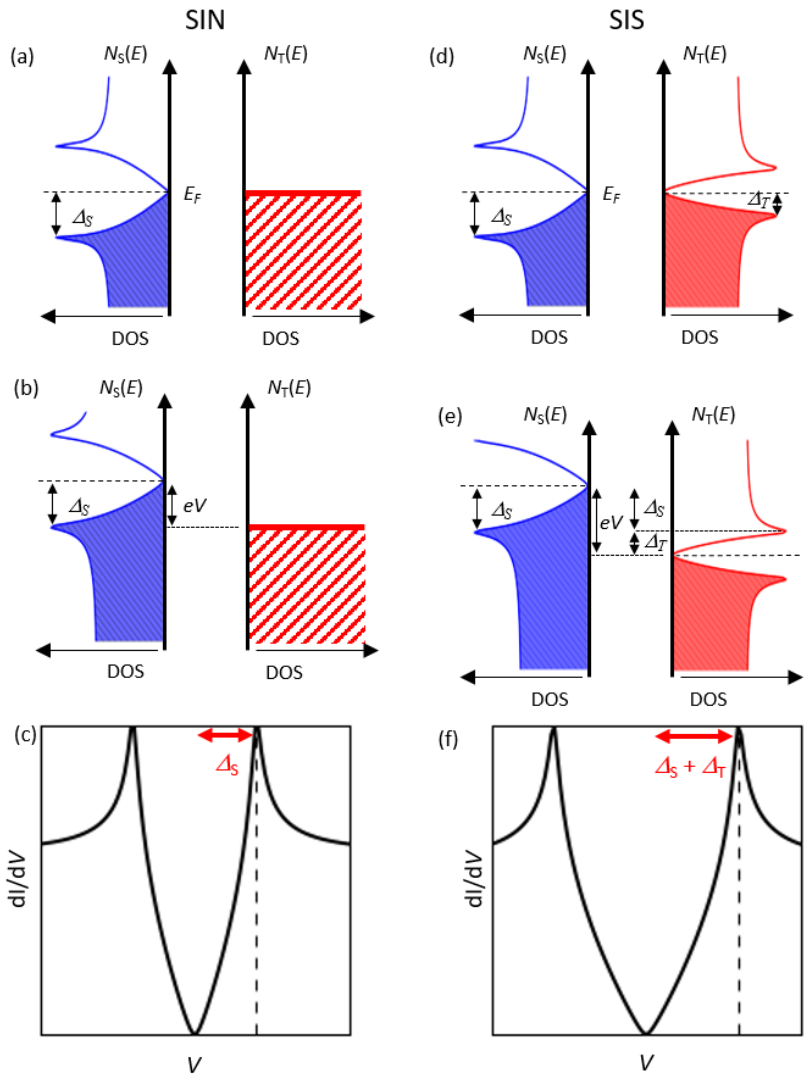

Figure 5.3: (a – c) Density of states of a normal metal tip and d−wave superconductor are illustrated with (a) zero bias and (b) finite sample bias voltage applied. The predicted dI/dV spectrum is shown in (c). (d – e) The density of states of two d−wave superconductors are illustrated with (d) zero bias and (e) finite sample bias voltage applied. The predicted dI/dV spectrum is shown in (f). The coherence peak will occur when $eV = \Delta_1 + \Delta_2$.

Figure 5.4 shows the measured dI/dV spectra with a tungsten tip (red) and a $Bi_2Sr_2CaCu_2O_{8+x}$−tip (blue). Coherence peak occurring at 14 meV in SIN spectrum shifted to 36 meV as a tip is converted to a $Bi_2Sr_2CaCu_2O_{8+x}$−tip. This ensures the fabrication of a $Bi_2Sr_2CaCu_2O_{8+x}$−tip.

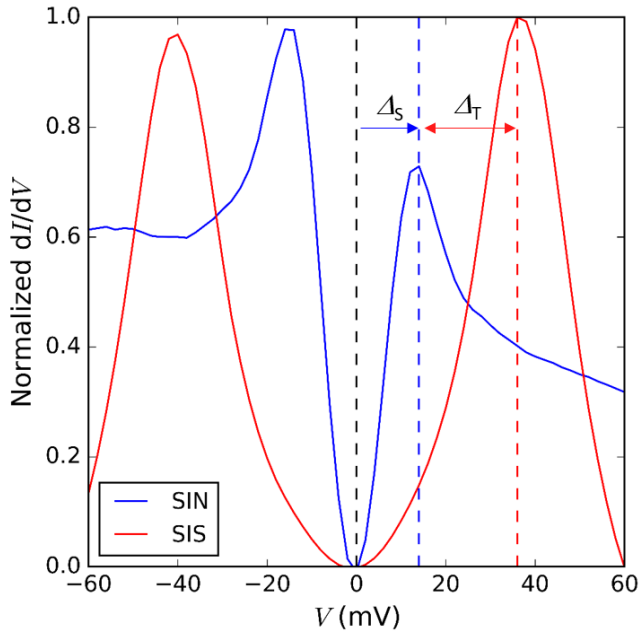

Figure 5.4: Measured dI/dV spectra with a tungsten tip (blue) and a $Bi_2Sr_2CaCu_2O_{8+x}$−tip (red). From an increase in the energy separation between coherence peaks, we can estimate Δ_T, $\Delta_T \approx$ 22 meV.

5. 3. Single-tunneling Regime to Pair-tunneling Regime

Having verified the fabrication of a $Bi_2Sr_2CaCu_2O_{8+x}$ tip, a Josephson junction can be formed by approaching a $Bi_2Sr_2CaCu_2O_{8+x}$ tip to a $Bi_2Sr_2CaCu_2O_{8+x}$ sample. When tip−sample distance sufficiently diminishes, the tunneling regime is changed from single−particle to pair−tunneling and it can be observed from current−voltage characteristic, as shown in Figure 5.5.

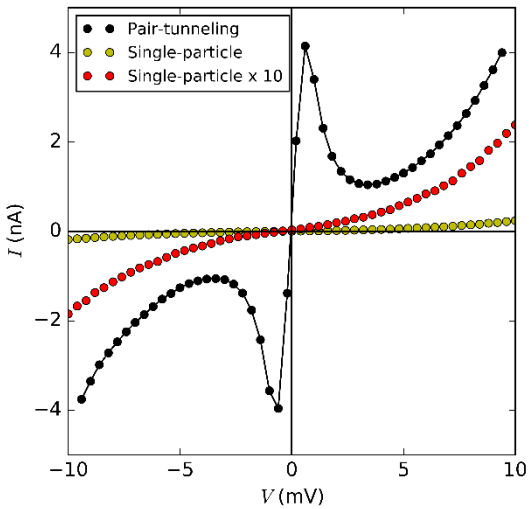

Figure 5.5: Comparison between current−voltage characteristics of pair−tunneling current (black) and single−particle tunneling (red). The presence of the current peaks near zero bias voltage indicates the tunneling regime has been changed to the pair−tunneling regime. Junction setup: 10 mV / 4.2 nA (black) and 10 mV / 25 pA (yellow).

Figure 5.6 (a) shows the resulting current−voltage characteristics of a junction at the same location with reducing tip−sample distance, i.e. normal state resistance, R_N. The near zero bias current peaks indicate the flow of pair−tunneling current and zero bias conductance peaks in Figure 5.6 (b) reaffirms it.

To extract the Josephson critical current from the measured current−voltage characteristics, the appropriate model has to be chosen. As discussed in the previous chapter, there are three relevant energy scales: the Josephson coupling energy E_J, thermal energy k_BT and the charging energy E_C.

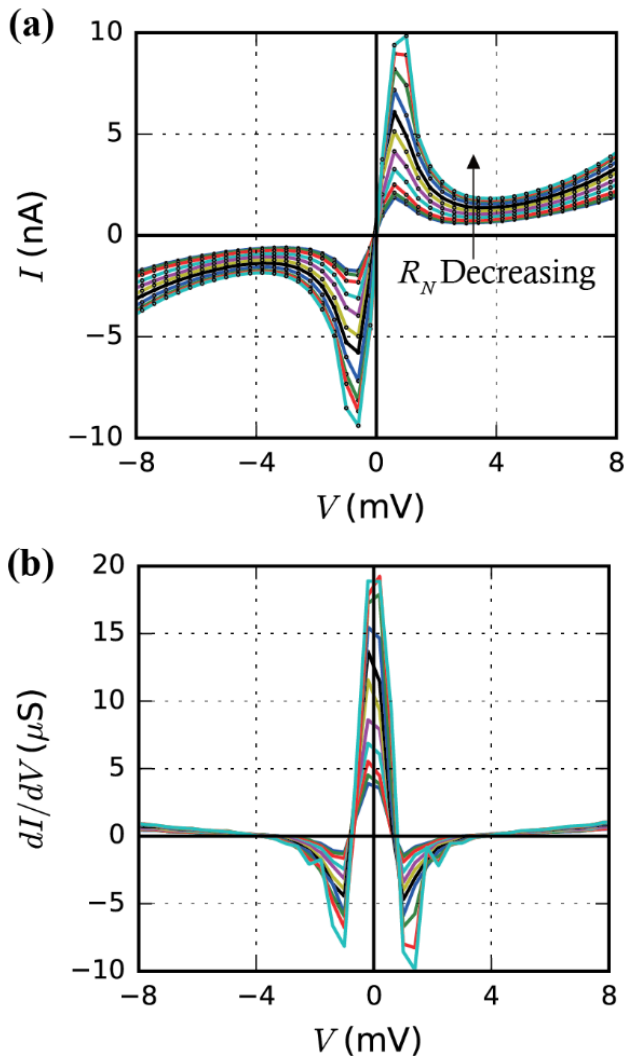

Figure 5.6: (a) Measured current−voltage characteristics of pair−tunneling current with reducing the tip−sample distance, or normal state resistance, R_N. (b) Numerical differentiation of the current−voltage characteristics in (a). Strong zero bias conductance peaks confirm the flow of pair−tunneling current.

The Josephson coupling energy E_J is given by

$$E_J = \frac{\hbar I_C}{2e} \tag{5.3.1}$$

Assuming I_C is 10 nA, then E_J = 0.075 meV. Thermal energy $k_B T$ at the STM base temperature of 4.2 K is 0.36 meV. The charging energy E_C is given by

$$E_C = \frac{2e^2}{C} \tag{5.3.2}$$

and by assuming the tip−sample capacitance C ~ 10 fF, E_C = 0.032 meV. The energy scales thus $k_B T > E_J > E_C$. The corresponding model is the phase diffusion model as shown in the previous Chapter 4. Current−voltage characteristic of the phase diffusion model is given by [98, 99]

$$I(V) = \frac{I_C^2 Z}{2} \frac{V}{V^2 + V_P^2} \tag{5.3.3}$$

, where Z is the ohmic environmental impedance and $V_P = 2eZ_1 k_B T/\hbar$. The current peak amplitude, $I(V_P)$, is directly proportional to the square of the Josephson critical current, thus the square root of the current peak amplitude, $\sqrt{I(V_P)} \propto I_C$, will be used as a quantity representing the Josephson critical current.

Knowing both I_C and R_N enables to exploit the Ambegaokar−Baratoff formula, which is given by [91, 92]

$$I_C R_N = \frac{\pi \Delta}{2e} \tag{5.3.4}$$

Since all the current−voltage characteristics are measured at the same location, Δ is constant. Hence, I_C and $G_N = 1/R_N$ should have a linear relation. This is plotted in Figure 5.7. As the linear fit fits well, this again assures the formation of Josephson junction and the phase diffusion model is an appropriate choice of model.

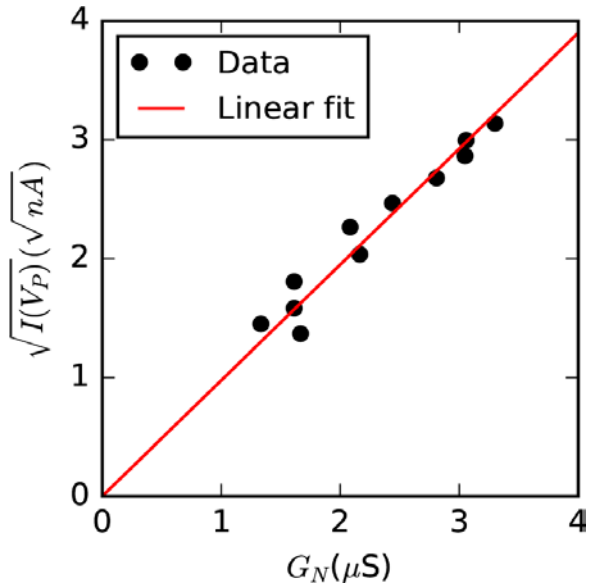

Figure 5.7: Square root of current peak amplitude, $\sqrt{I(V_P)}$, is plotted with respect to the normal state conductance, $G_N = 1/R_N$. Black solid circles represent the measured data and red solid line represent the linear fit.

5. 4. Characterization of *r*-space resolution

In Section 5.2, topographic images showed that a $Bi_2Sr_2CaCu_2O_{8+x}$−tip can resolve atoms. A more precise method to show its *r*−space resolution is detecting a single impurity atom. STM study has shown that a Zn impurity atom in $Bi_2Sr_2CaCu_2O_{8+x}$ induces impurity states in its vicinity. [102] Impurity states are extended from its center with a cross−shaped *r*−space structure with a characteristic resonance peak at $V = -1.5$ mV. Certainly, this impurity states are local, isolated electronic structure and detecting these local electronic structures can well demonstrate the *r*−space resolution of a $Bi_2Sr_2CaCu_2O_{8+x}$−tip.

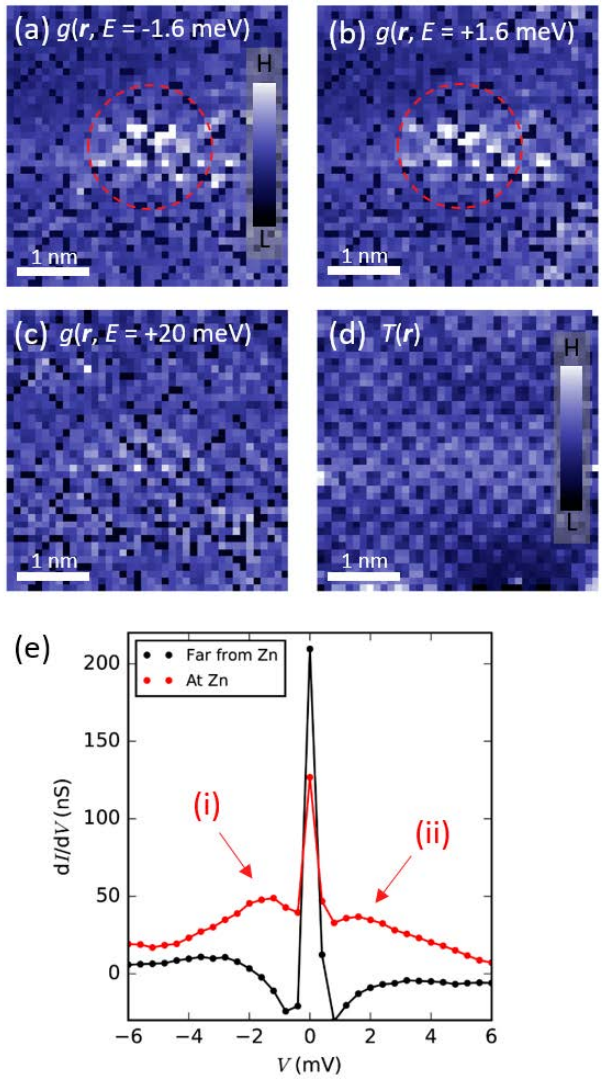

Figure 5.8: (a – c) Conductance map, $g(\boldsymbol{r}, E)$, measured in the same field of view at (a) −1.6 meV, (b) 1.6 meV and (c) 20 meV. Impurity states are detected at a bias voltage of −1.6 mV and +1.6 mV, as guided by dashed red circles. (d) Topographic image, $T(\boldsymbol{r})$, measured in the same field of view in (a – c) (e) Conductance spectrum of the bright spot in (a) (red). Two peaks at V = −1.6 mV and +1.6 mV are observed. Conductance spectrum measured at a point far from the bright spot is shown as black. Background quasiparticle tunneling conductance is subtracted for both spectra.

Figure 5.8 (a) shows the measured SIS conductance map, $g(\boldsymbol{r}, E = -1.6$ meV). Impurity states can be found, as guided by a red circle, and the corresponding resonance peak can be seen in Figure 5.8 (e). The energy of the impurity resonance peak (−1.6 meV) coincides with the reported Zn impurity resonance peak. [102] In addition, the cross−shaped spatial structure of the impurity state resembles that of Zn impurity. Thus, we can conclude that the observed impurity states are originated from a Zn impurity. Furthermore, the simultaneously acquired topographic image, shown in Figure 5.8 (d), has no surface defects further supporting it. The detection of a single isolated impurity in SIS conductance map provides valuable information that a $Bi_2Sr_2CaCu_2O_{8+x}$−tip is capable to resolve nanometer−sized local electronic structures.

A close look at impurity states in SIS dI/dV spectra reveals two features. First, the amplitude of a resonance peak is significantly smaller than that of SIN dI/dV spectrum. Second, an additional peak at V = +1.6 mV is observed, while only one resonance peak is observed at V = −1.5 mV in SIN dI/dV spectrum in the vicinity of a Zn impurity atom. [102] The additional resonance peak has a smaller amplitude than the peak at the negative bias voltage. In addition, the r−space structure of impurity states is found to be particle−hole symmetric. To explain these features, we propose a simple toy model. Figure 5.9 (a) shows the density of states of a tungsten tip and a $Bi_2Sr_2CaCu_2O_{8+x}$sample when the negative sample bias is applied. A Zn impurity state is located $|\Omega|$ = 1.6 meV below the Fermi energy resulting in a resonance peak at V = −1.6 mV. On the other hand, a $Bi_2Sr_2CaCu_2O_{8+x}$−tip has V−shape profile of density of states as depicted in Figure 5.9 (b), the resonance peak will appear at the same sample bias voltage but because of a much smaller density of states of the tip, the peak amplitude will be much smaller as experimentally observed. Meanwhile, in order to form a Josephson junction at 4.2 K, a $Bi_2Sr_2CaCu_2O_{8+x}$−tip has to be extremely close to a sample. Considering the fact that Zn impurity induces impurity states over a radius of a few nanometers, Zn impurity in a sample may induce

identical impurity states in a $Bi_2Sr_2CaCu_2O_{8+x}$−tip. In this case, one would expect the density of states of the impurity states in a $Bi_2Sr_2CaCu_2O_{8+x}$−tip is smaller than that in a sample. When a negative sample bias voltage is applied, impurity states in a sample will be measured (Figure 5.9 (c)). When a positive sample bias voltage is applied, impurity states in a $Bi_2Sr_2CaCu_2O_{8+x}$−tip is measured giving a symmetric peak at V = +1.6 mV (Figure 5.9 (d)). Since, we assumed the density of states of impurity states in a $Bi_2Sr_2CaCu_2O_{8+x}$−tip is smaller, the amplitude of peak at positive bias concurrently smaller than that of at a negative bias. Therefore, this toy model can explain particle−hole symmetric resonance peaks observed in the SIS conductance spectra.

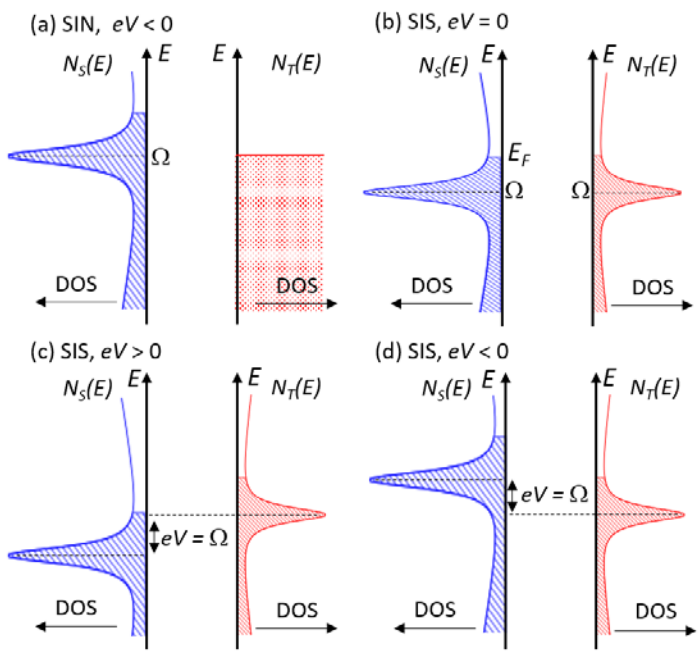

Figure 5.9: Density of states of tip and sample with Zn resonance peak. **Ω** denotes the resonance energy. (a) With a tungsten tip, when negative sample bias is equal to the resonance energy, the resonance peak is measured in the conductance spectrum. (b – c) With a $Bi_2Sr_2CaCu_2O_{8+x}$−tip, when positive (negative) sample bias is equal to the resonance energy of tip (sample), the resonance peak is measured in the conductance spectrum.

5. 5. Superconducting Gap map

Within the previous sections, *in-situ* fabricated $Bi_2Sr_2CaCu_2O_{8+x}$-tip has been characterized and demonstrated that it is capable to form a Josephson junction in a controlled way and has a nanometer resolution. Now, we are in a position to directly measure spatial variations of the superconducting order parameter in a nanometer scale.

One of the advantages of SJTM is that one can convert the tunneling regime from the single-particle tunneling to the pair-tunneling regime and vice versa, by controlling the tip-sample distance. In this section, I will present the superconducting gap map calculated from the pair-tunneling current and compare with a gap map generated by a completely independent single-particle tunneling result.

One technical detail has to be addressed. In order to measure Josephson effect, tip-sample distance typically characterized by a junction resistance has to be extremely small. While conventional STM measurement on $Bi_2Sr_2CaCu_2O_{8+x}$ is performed at 1 GOhm setup junction (100 mV/100 pA), for SJTM measurement the setup junction resistance has to be smaller than 5 MOhm (10 mV / ~2 nA), which is ~200 times larger than typical STM setup junction resistance. It is almost impossible to scan with such a low junction resistance, we used two setup junctions, one for scanning with higher junction setup and another for Josephson effect measurement with lower junction setup. Thus, the measurement is performed as follows.

Move tip laterally with higher junction resistance setup and push tip towards the sample with lower resistance setup junction and measure Josephson effect. Pull back the tip away from the sample with a higher junction resistance setup and repeat the process above. Through these processes, we can avoid possible tip crash during the measurement. However, changing the junction setup consumes a substantial amount of time and limits the possible duration of

measurement time (typically < 3 days).

According to the Ambegaokar–Baratoff formula, the product of Josephson critical current, I_C, and the normal state resistance, R_N, is proportional to the superconducting gap, $I_C R_N \propto \Delta$. I_C is proportional to the square root of the current peak amplitude, $\sqrt{I(V_P)}$, and here, I refer to the $\sqrt{I(V_P)}R_N$ product as Δ_{AB}, $\Delta_{AB} \equiv \sqrt{I(V_P)}R_N$. Since the current peak amplitude corresponds to I_C, measuring current–voltage characteristics in a two–dimensional grid of points across the sample surface enables to create the Josephson critical current map, $I_C(\boldsymbol{r})$. $I_C(\boldsymbol{r})$ multiplied by the normal resistance map, $R_N(\boldsymbol{r})$, thus generates a gap map, $\Delta_{AB}(\boldsymbol{r})$. Figure 5.10 (b) shows the measured $\Delta_{AB}(\boldsymbol{r})$ in a 60 nm x 60 nm field of view.

$\Delta_{AB}(\boldsymbol{r})$ may be viewed as a superconducting gap map for the following reasons. The process regards only a pair–tunneling current. Moreover, the Ambegaokar–Baratoff formula assumes a superconducting gap and removes possible geometric effects in $I_C(\boldsymbol{r})$. With all together, $\Delta_{AB}(\boldsymbol{r})$ will be closely related to a superconducting gap map.

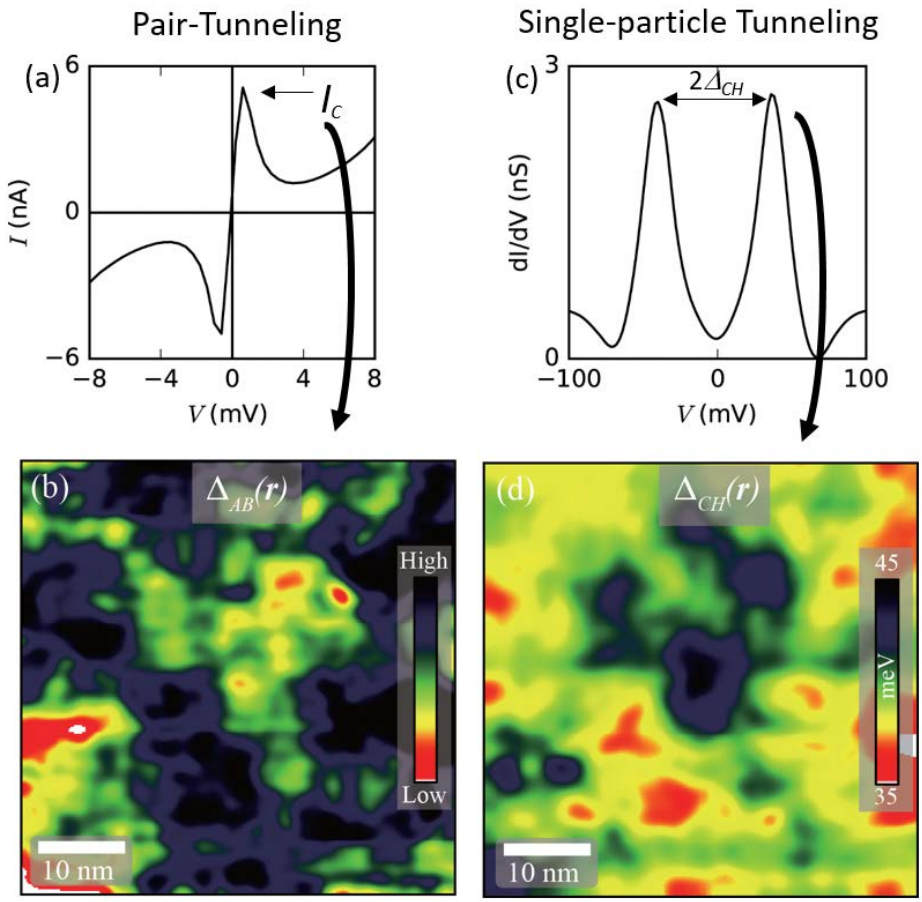

Figure 5.10: (a – b) Pair−tunneling regime. (a) $I_C(\boldsymbol{r})$ is extracted from the measured current−voltage characteristic across the 60 nm x 60 nm field of view. (b) $\Delta_{AB}(\boldsymbol{r})$ in a 60 nm x 60 nm field of view is shown, which is determined by multiplying $I_C(\boldsymbol{r})$ by $R_N(\boldsymbol{r})$ in the same field of view. Lattice supermodulations are removed by the Fourier Filteration and low pass filter is applied. (c – d) Single−particle tunneling regime. (c) SIS Conductance spectrum measured in a single−particle tunneling regime. Conventionally gap is defined by the energy separation between coherence peaks. Here, this gap is dubbed as Δ_{CH}. (d) Gap map, $\Delta_{CH}(\boldsymbol{r})$, generated by the conventional method. Lattice supermodulations are removed by the Fourier Filteration and low pass filter is applied.

On the other hand, a gap in the STM conductance spectrum is conventionally defined by the energy separation between coherence peaks and here, this gap is dubbed as Δ_{CH}. Figure 5.10 (d) shows $\Delta_{CH}(\boldsymbol{r})$ in the same field of view as in Figure 5.10 (b). Note that Δ_{CH} is calculated from the single-tunneling measurement, which is completely independent of the pair-tunneling current measurement. As can be seen by eyes, $\Delta_{AB}(\boldsymbol{r})$ and $\Delta_{CH}(\boldsymbol{r})$ are apparently anticorrelated. To quantify their anticorrelation, the normalized cross-correlation can be evaluated. The definition of the normalized cross-correlation between two-dimensional maps, $f(\boldsymbol{r})$ and $g(\boldsymbol{r})$, is given by [103]

$$C_{f,g}(\boldsymbol{R}) = \frac{\int [f(\boldsymbol{r}) - \bar{f}][g(\boldsymbol{r}+\boldsymbol{R}) - \bar{g}] d^2\boldsymbol{r}}{\sqrt{A_{f,f}(0) A_{g,g}(0)}}$$

, where $\mathrm{A_{f,f}}(R) = \int [f(\boldsymbol{r}) - \bar{f}][f(\boldsymbol{r}+\boldsymbol{R}) - \bar{f}] d^2\boldsymbol{r}$. Figure 5.11 shows the azimuthally averaged normalized cross-correlation coefficient of Δ_{AB} and Δ_{CH}. The normalized cross-correlation coefficient is −0.65, showing a strong anticorrelation between $\Delta_{AB}(\boldsymbol{r})$ and $\Delta_{CH}(\boldsymbol{r})$. The similar anticorrelation between $I_C R_N$ and Δ_{CH} is also reported by Kimura *et al.* [85]

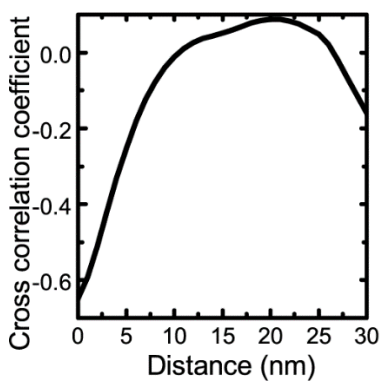

Figure 5.11: Azimuthally averaged normalized cross-correlation coefficient of Δ_{AB} and Δ_{CH}. The coefficient at the center is −0.65 indicating a strong anticorrelation.

The discrepancy between them poses a possibility that the origin of Δ_{CH} may not be superconductivity. One possible candidate taking responsible for Δ_{CH} is a pseudogap state. Two gap nature of a pseudogap and superconducting gap has been introduced in Chapter 2. Among the compelling experimental evidence, STM studies observe two different energy scales in dI/dV spectra. [31, 52, 53, 104] Especially, doping dependent studies [31] revealed two energy scales evolving differently with the decrease in doping level. Δ_{CH} monotonically increases as a doping level decreases from overdoped to underdoped, analogous to the evolution of the characteristic temperature of pseudogap, T^*, while another energy scale, Δ_0, defined by a kink in the conductance spectrum [31] or quasiparticle interference extinction energy [45], follows the evolution of T_C and becomes doping independent. Moreover, spatial homogeneity also distinguished. Δ_{CH} is found to be spatially inhomogeneous, whereas Δ_0 is spatially uniform. [31, 45, 52, 104] Furthermore, magnetic field dependent STM studies in the vortex states revealed that two different energy scales. [47] These results all suggest a possibility that Δ_{CH} is a pseudogap rather than a superconducting gap. In this scenario, Δ_{CH} represents the pseudogap map while Δ_{AB} is a true superconducting gap map. The discrepancy between Δ_{AB} and Δ_{CH} thus supports the two gap dichotomy of pseudogap and superconducting gap.

The anticorrelation between Δ_{AB} and Δ_{CH} suggests the interplay between superconductivity and pseudogap. The interplay between pseudogap and superconductivity was suggested by many researches. In the presence of the magnetic field, STM study reported charge order associated with pseudogap was found in the vortex state where superconductivity is destroyed. [68] Furthermore, superconductivity coherence suppressed by magnetic field was anticorrelated to coexisting pseudogap. [47] In momentum space, temperature and doping dependent ARPES measurement showed that pseudogap is not static below T_C but interact with superconductivity. [105, 106] Meanwhile, charge order is found in the pseudogap. Especially,

charge order reported by STM−RXS study on $Bi_2Sr_2CaCu_2O_{8+x}$ showed that charge order onsets at about T^* and strongest at T_C, then gradually weaken below T_C. [71] Similar competition between charge density wave and superconductivity also reported in $YBa_2Cu_3O_{6.67}$. [107] Intertwined order theory predicts not only charge order but also other symmetry breaking order, such as nematic phase, are all intertwined together with superconductivity. [57]

6. SJTM II: SJTM at 50 mK.

6.1. Introduction

Analogous to the SJTM at 4.2 K, SJTM experiment was performed at 50 mK. Lowering the temperature by 100 times smaller from 4.2 K to 50 mK enables to have a larger junction resistance to form a Josephson junction providing a much more stable junction. This provides a longer measurement time with far less probability of tip change and allows to achieve better r-space resolution and larger field of view. Exploiting this advantage, in this section, we performed SJTM experiment on slightly overdoped $Bi_2Sr_2CaCu_2O_{8+x}$ (T_C ~ 88 K). We directly measured the spatial variations of superfluid density and detected the modulations of the superfluid density, Cooper-pair density wave (PDW).

6.2. Cooper-pair density wave (PDW)

An exotic state called "Cooper-pair density wave" (PDW) is predicted by many theories. [57, 108-111] Unlike the conventional Cooper-pairs, which have net zero momentum as two electrons having the exact opposite momentum are paired, in PDW states, Cooper-pairs have finite net momentum and propagates.

6.1. Fulde-Ferrel-Larkin-Ovchinnikov (FFLO) State

FFLO state is first proposed by Fulde and Ferrel [112], and Larkin and Ocvhinnikov [113] in 1964. In the FFLO state, the Cooper-pairs formed between Zeeman split parts of Fermi surface with a finite center-of-mass momentum.

In type II superconductors, the upper critical field H_{C2} is determined by orbital pair breaking effect and Pauli paramagnetic pair breaking effect. External magnetic field penetrates and forms vortex

line in type II superconductors, while the kinetic energy of the supercurrent flowing around the vortex cores reduces condensation energy. The phase transition to normal state occurs when vortex cores overlapped at an orbital upper critical field, which is given by $H_{c2}^{orb} = \Phi_0/2\pi\xi^2$. [114] On the other hand, as the Cooper-pair carries zero spins (here, assuming spin-singlet superconductors), Cooper-pairs have zero spin susceptibility. Upon applying a larger magnetic field, spin polarized normal metal has lower energy than the superconducting state, which determines a Pauli-limited upper critical field, which is estimated to be $H_{c2}^{P} = \sqrt{2}\Delta/g\mu_B$. [115] Generally, both effects contribute to the determination of the upper critical field and their relative importance is evaluated by the Maki parameter, [114]

$$\alpha = \sqrt{2}\frac{H_{c2}^{orb}}{H_{c2}^{P}} \tag{6.2.1}$$

When a system has a sufficiently large Maki parameter, a new pairing state, FFLO state, can be formed. Because of the Zeeman effect, the Fermi surface is split into spin-up Fermi surface and spin-down Fermi surface. FFLO pointed out that the pairing between ($\boldsymbol{k}\uparrow$, $-\boldsymbol{k}+\boldsymbol{q}\downarrow$) with $\boldsymbol{q}\sim 2\mu_B H/\hbar v_F$ can reduce the Zeeman energy. Note that the center-of-mass momentum of a pair is non-zero in FFLO state, contrast with zero center-of-mass momentum of BCS state. As a result, the FFLO state will break spatial symmetry. Figure 6.1 illustrates these pairing states.

Two distinct types of superconducting order parameter are considered. Fulde and Ferrel considered [112]

$$\Delta(\boldsymbol{r}) = \Delta_1 e^{i\boldsymbol{q}\cdot\boldsymbol{r}}$$

, where Δ_1 is a real number. In the Fulde-Ferrel (FF) state, only the phase modulates periodically in real space while the amplitude of the order parameter remains homogenous. In this state, only a fraction

of the Zeeman split Fermi surfaces participates the pairing and the resulting net magnetization reduces Zeeman energy (red shaded region in Figure 6.1 (b)).

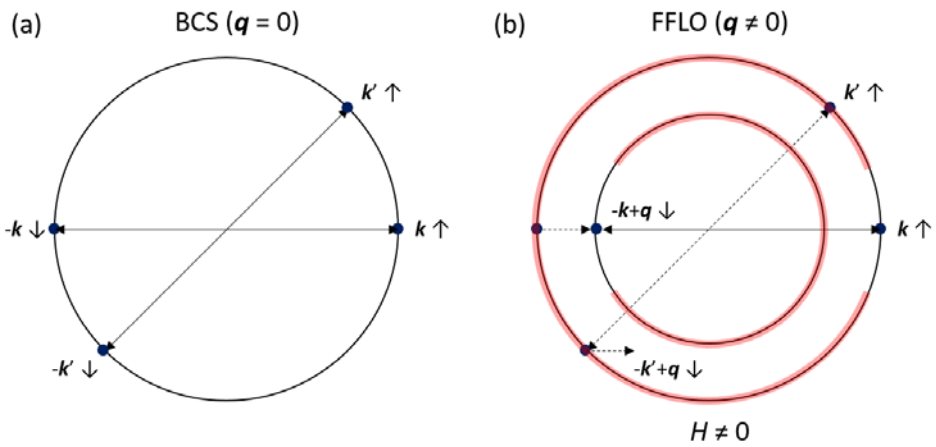

Figure 6.1: Schematic illustration of pairing states. (a) BCS pairing state. (b) FFLO pairing state with a finite center-of-mass momentum $\boldsymbol{q}$. The inner and outer circle represent the Zeeman split spin up and spin down bands, respectively. Red shaded regions represent the un-paired region for FF states.

Meanwhile, Larkin and Ovchinnikov propsed [113],

$$\Delta(\mathrm{r}) = \Delta_1\left(e^{i\boldsymbol{q}\cdot\boldsymbol{r}} + e^{-i\boldsymbol{q}\cdot\boldsymbol{r}}\right) = 2\Delta_1\cos(\boldsymbol{q}\cdot\boldsymbol{r})$$

, where Δ_1 is again a real number. In this Larkin-Ovchinnikov (LO) state, the order parameter becomes spatially modulating with a wavelength of $2\pi/q$. Hence, Cooper-pair density itself also modulates periodically. Generally, the LO state is found to have lower energy. [114, 116] Note that FF- or LO- state both break the U(1) gauge symmetry indicating the superconductivity.

However, despite many endeavors, FFLO states are never been directly detected. This is because the requirement for the system to

achieve FFLO states is strict. [114, 116] First of all, a superconductor has to be type II with a large Maki parameter. Since it has been shown that orbital effects hinder FFLO states, Pauli pair breaking effect must be the dominant which leads a large Maki parameter. For a similar reason, an applied magnetic field has to be precisely parallel to the superconducting plane, otherwise, the magnetic field will create vortex states, which are detrimental to the FFLO state. Furthermore, superconductor must be in a very clean limit as the FFLO state is fragile against impurities. The detailed review about FFLO state can be found in references. [114, 116]

6.2. Pair Density Wave in Cuprates

In cuprates, many theories predict zero-field PDW state (Hereafter, PDW state will only refer to zero-field PDW to distinguish from FFLO state). Just like the FFLO state, PDW state has modulating superconducting order parameter. This state is proposed to explain distinguished property in $La_{2-x}Ba_xCuO_4$. In $La_{2-x}Ba_xCuO_4$, especially at $x = 1/8$ doping, together with the emergence of spin- and charge- density wave, strong decoupling between layers are observed. [57, 60] SDW and CDW emerge as the temperature decreases and upon further cooling 2D superconductivity arises. The intriguing thing is that 2D superconductivity arises much higher temperature than the onset temperature of 3D superconductivity, as can be seen in Figure 6.2 (a). Hence, there is a phase where the 2D superconductivity sets in, but only in in-plane and the interlayer Josephson coupling is completely frustrated.

In pursuit of understanding this phenomenon, new theories proposed a new type of state, PDW. [57, 108-111] The theories suggest that the stripe PDW state sets in at T_{2D}, but with π-phase difference between layers as shown in Figure 6.2 (b). Consequently, the interlayer Josephson coupling is suppressed and 3D superconductivity is concurrently suppressed.

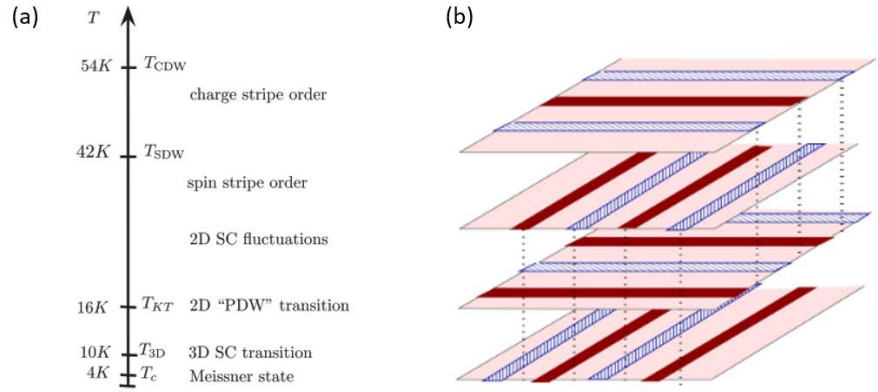

Figure 6.2: (a) The onset temperatures and corresponding phases of $La_{2-x}Ba_xCuO_4$ at x = 1/8. Reproduced from [57]. (b) Stacking of stripe planes with π–phase shift between layers. Reproduced from [108].

6.3. Tip characterization

A $Bi_2Sr_2CaCu_2O_{8+x}$–tip was fabricated in the same way in the SJTM at 4.2 K. After the fabrication of a $Bi_2Sr_2CaCu_2O_{8+x}$–tip, the first step is the characterization of the tip. The characterization has been performed by measuring topographic images and conductance spectra, following the same procedure performed in the previous Chapter 5.3.

Figure 6.3 shows topographic images measured by a $Bi_2Sr_2CaCu_2O_{8+x}$–tip. Atomic corrugations and lattice supermodulations are clearly resolved in the SIS topographic image while local surface structures such as lattice mismatches are absent due to the convolution nature of a junction. The convolutional effect has been described in the previous Chapter 5.3.

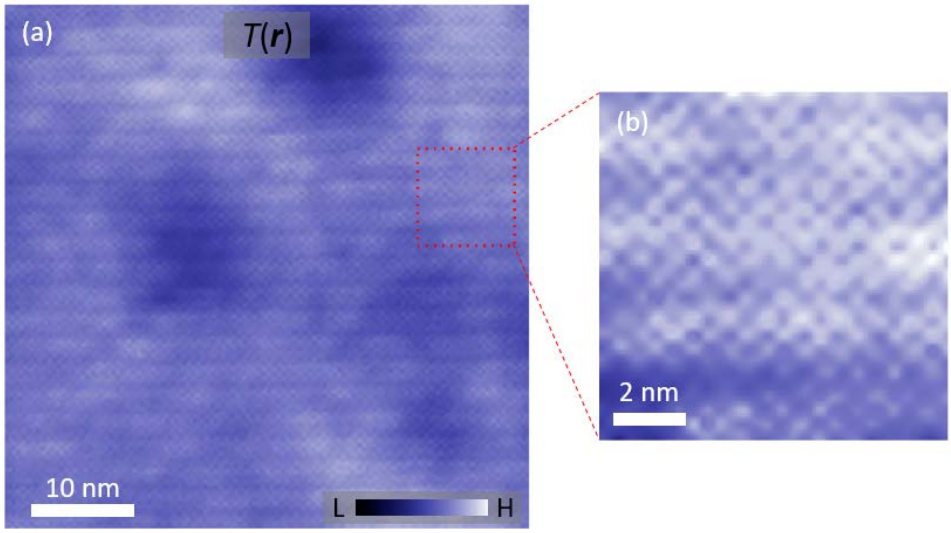

Figure 6.3: Topographic images measured by a $Bi_2Sr_2CaCu_2O_{8+x}$−tip. (a) A 53 nm x 53 nm field of view topographic image. (b) Zoomed−in field of view of red dashed box in (a).

Further spectroscopic characterization is performed from the measured conductance spectrum. Figure 6.4 shows the SIN and SIS conductance spectra. The energy separation between coherence peaks is actually shifted from 37 meV to 62 meV as the junction is converted from SIN to SIS verifying that the fabrication of a $Bi_2Sr_2CaCu_2O_{8+x}$−tip, at the same time, this $Bi_2Sr_2CaCu_2O_{8+x}$−tip has a gap of 25 meV.

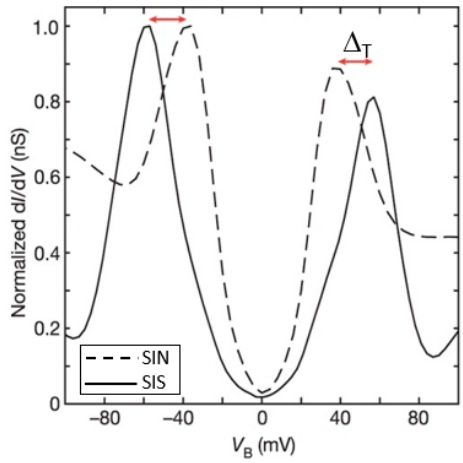

Figure 6.4: Measured dI/dV spectra with a tungsten tip (dashed line) and a $Bi_2Sr_2CaCu_2O_{8+x}$−tip (solid line). From an increase in the energy separation between coherence peaks, we can estimate Δ_T, $\Delta_T \approx 25$ meV.

6.4. Single-tunneling Regime to Pair-tunneling Regime

Having characterized a $Bi_2Sr_2CaCu_2O_{8+x}$−tip, now we can move on to measure pair−tunneling current by reducing the tip−sample distance. The measured current−voltage characteristics in the pair−tunneling regime are shown in Figure 6.5. To analyze the measured current−voltage characteristics, we need to choose the correct model. The energy scales related to the phase dynamics are the Josephson coupling energy E_J, the charging energy E_C, and thermal energy $k_B T$. For an STM base temperature of 50 mK, thermal energy $k_B T$ ~ 4.3 ueV. For I_C ~ 1 nA, E_J ~ 7.5 ueV. Assuming the capacitance of a junction as 10 fF gives E_C ~ 32 ueV. The correct model for this junction is the $P(E)$−theory as discussed in the previous Chapter 4.

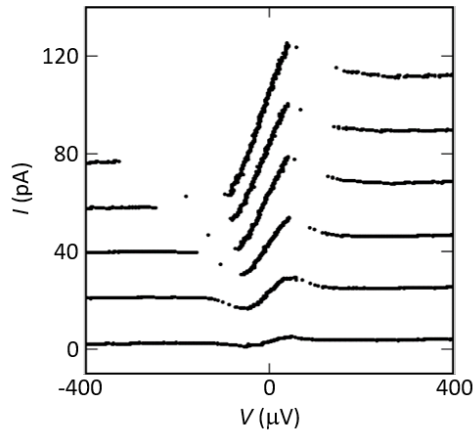

Figure 6.5: Measured current−voltage characteristics of pair−tunneling current with reducing the tip−sample distance.

Note that again the current peak amplitude is proportional to the square of I_C. Thus, measuring current−voltage characteristics and current peaks across the sample with a fine resolution provides the spatial variation of I_C, $I_C(\boldsymbol{r})$.

6.5. Characterization of *r*-space resolution.

Detection of a single impurity atom again provides the imaging capabilities of a $Bi_2Sr_2CaCu_2O_{8+x}$−tip. Figure 6.6 (a) shows the single−particle tunneling conductance map, $g(\boldsymbol{r}, E = -20$ meV) and Zn impurities are located by resonance peaks. Because of the convolution nature of a $Bi_2Sr_2CaCu_2O_{8+x}$−tip, the resonance energy is shifted to $E \sim -20$ meV. Note that smaller resonance peak, which was found in Chapter 5, also observed near zero bias.

$I_C(\boldsymbol{r})$ taken in the same field of view is shown in Figure 6.6 (b). Zn impurity in $Bi_2Sr_2CaCu_2O_{8+x}$ is known for breaking superconductivity. [102] The suppression of I_C is clearly observed in the vicinity of Zn impurities found in Figure 6.6 (a). This not only characterizes *r*−space resolution of a $Bi_2Sr_2CaCu_2O_{8+x}$−tip but also verifies that measured I_C is indeed proportional to the Cooper−pair density.

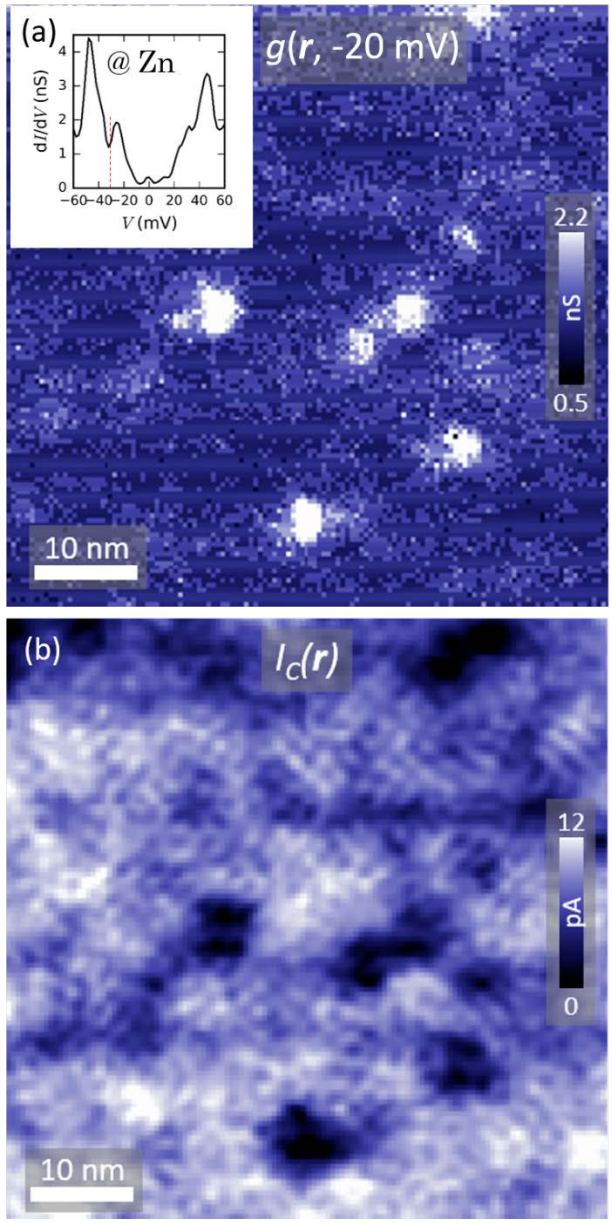

Figure 6.6: (a) The measured SIS conductance map, $g(\boldsymbol{r}, E = -20$ meV). Bright areas locate the Zn impurities. (Inset) Conductance measured at the bright site. Zn resonance energy is shifted due to the spectrum of a tip as indicated as a red dashed line. Smaller resonance peak is also observed near zero bias. (b) $I_C(\boldsymbol{r})$ measured in the same field of view as (a). The suppression of I_C, or superfluid density, in the vicinity of Zn sites is clearly observed.

6.6. Detection of Cooper-pair density wave.

In Chapter 5, we have directly measured the superconducting order parameter, Δ via the Ambegaokar–Baratoff formula. In this chapter, we instead analyze $I_C(\boldsymbol{r})$ rather than $\Delta(\boldsymbol{r})$ to detect PDW because PDW may or may not affect the amplitude of Δ depending on its wave function. For example, recall the FF state introduced in Chapter 6.2. In the FF state, only the phase of the order parameter rotates while the amplitude of the order parameter remains constant. Hence, measuring $I_C(\boldsymbol{r})$ which is proportional to the superfluid density is a proper choice to detect PDW.

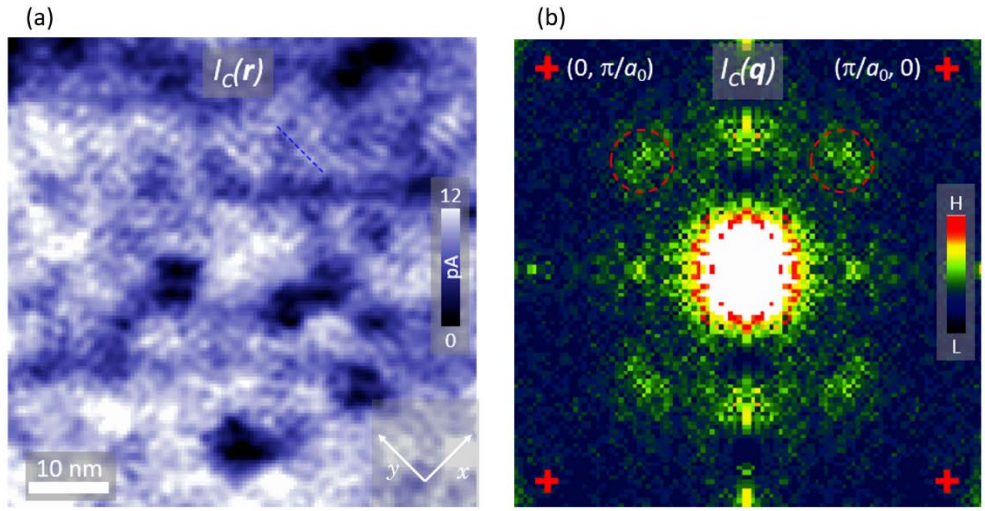

Figure 6.7: (a) IC(r) measured in a field of view of 60 nm x 60 nm. Modulations along the Cu–O bond directions are clearly observed. (b) The Fourier transform of $I_C(\boldsymbol{r})$ in (a). Red dashed circles show the wave vectors of the modulations in (a). The wave vectors Q_P are $(0.25, 0)\frac{2\pi}{a_0}$ and $(0,0.25)\frac{2\pi}{a_0}$.

In $I_C(\boldsymbol{r})$ in Figure 6.6 (b), one can easily notice the modulations of $I_C(\boldsymbol{r})$ along with the x and y directions. The modulations of $I_C(\boldsymbol{r})$ can be seen more clearly. The wave vectors of the modulations can be found in the power spectrum of the Fourier transform of Figure 6.7

(a), $I_C(\boldsymbol{q})$, which is shown in Figure 6.7 (b). The corresponding wave vectors are $Q_P \approx (0.25, 0)\frac{2\pi}{a_0}$ and $(0,0.25)\frac{2\pi}{a_0}$.

The line profile along the blue line in Figure 6.7 (a) is shown in Figure 6.8 as blue dots. The modulation of $I_C(\boldsymbol{r})$ corresponding to the wave vector Q_P is plotted together as a red solid line. The well-correspondence between them verifies the modulations of $I_C(\boldsymbol{r})$ with a periodicity of $4a_0$.

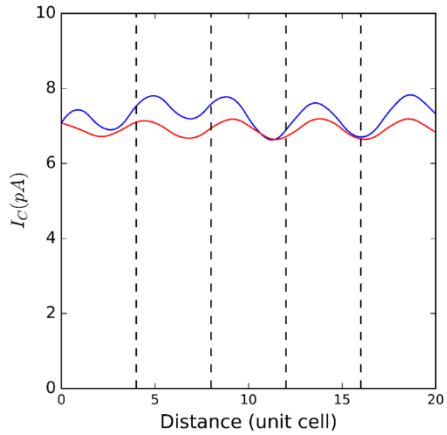

Figure 6.8: Line profile of $I_C(\boldsymbol{r})$ along the blue dashed line in Figure 6.7 (a). The modulation of $I_C(\boldsymbol{r})$ corresponding to the wave vector Q_P is plotted as a red solid line.

Having verified that I_C is proportional to the Cooper-pair density wave, the modulations of $I_C(\boldsymbol{r})$ are equivalently the modulations of the Cooper-pair density, *i.e.* pair density wave (PDW). PDW is theoretically expected to be present in the cuprates, although experimentally has never observed hitherto. The results presented here are the first experimental evidence of the presence of PDW. Furthermore, as can be seen in Figure 6.8, the modulation amplitude is ~5% of its average value. Hence, for below 50 mK, PDW state is subdominant to the *d*-wave superconductivity state in $Bi_2Sr_2CaCu_2O_{8+x}$ at p = 17%.

6.7. Discussion

PDW is one key part of the intertwined order theory. [57, 109] In the intertwined order picture, upon raising the temperature, spontaneously broken symmetries in a "parent" state are partially melted. Consequently, in this intermediate or so-called "vestigial" orders possess a subset of broken symmetries in the parent state. It has been shown that the pure PDW state as a parent state can produce experimentally observed symmetry broken states, i.e., nematic phase and stripe phase. Especially, the stripe phase and the suppression of the interlayer Josephson coupling can be described within the intertwined order with the presence of PDW. [57, 108, 109] However, PDW state is only predicted theoretically hitherto and no clear experimental evidence has not been found. Although no stripe phase and suppression of the interlayer Josephson coupling has not been detected in Bi-based compounds, detection of PDW in $Bi_2Sr_2CaCu_2O_{8+x}$ can expedite the theoretical understanding in cuprates physics.

On the other hand, the fact that charge ordered states found in $Ca_{2-x}Na_xCuO_2Cl_2$ [48, 69], $Bi_2Sr_2CuO_{6+x}$ [47], and $Bi_2Sr_2CaCu_2O_{8+x}$ [48, 49] have a similar periodicity to that of PDW state suggests intimate relation between them. Some theories indeed showed that a PDW state coexisting with uniform d-wave superconductivity induces CDW state and vice versa. [57, 109] It has not been confirmed which state coexists with uniform d-wave superconductivity, however, all three states are seemingly intertwined in a way. Direct comparative analysis between single-particle tunneling measurement (charge order) and pair-tunneling measurement (PDW state) is required to address this problem.

7. Conclusion

In this thesis, I have introduced the novel technique, Scanning Josephson Tunneling Microscopy (SJTM), and presented SJTM studies on $Bi_2Sr_2CaCu_2O_{8+x}$ at two different temperatures of 4.2 K and 50 mK. Both studies utilized a novel in-situ tip fabrication method with the aid of a novel STM head design introduced in Chapter 3 and a $Bi_2Sr_2CaCu_2O_{8+x}$-tip has been successfully characterized throughout Chapter 5 and Chapter 6.

In Chapter 5, I presented the first SJTM study performed on $Bi_2Sr_2CaCu_2O_{8+x}$ at 4.2 K, which is the highest temperature for SJTM experiments that have been reported. SJTM has its advantage that it can able to convert the tunneling regime from single-particle tunneling to pair-tunneling regime and vice versa. By exploiting this advantage, the direct measurement of spatial variation of superconducting order parameter revealed the possible discrepancy between pseudogap map and true superconducting gap map, although more studies in wide doping range are required to explicate the relation between pseudogap and superconductivity.

The substantial increase in the temperature range for SJTM suggests SJTM studies on extremely underdoped- or overdoped-$Bi_2Sr_2CaCu_2O_{8+x}$. Recent STM study showed that they can control the doping level of $Bi_2Sr_2CaCu_2O_{8+x}$ by vacuum-annealing and achieved extremely underdoped $Bi_2Sr_2CaCu_2O_{8+x}$ in the insulating phase. [72] With the expanded temperature range, *in-situ* tip fabrication, and *in-situ* tip preparation stage, it is possible to perform SJTM on extremely underdoped $Bi_2Sr_2CaCu_2O_{8+x}$ below and above T_C. This could help to develop theories in cuprate physics.

In Chapter 6, SJTM study performed on $Bi_2Sr_2CaCu_2O_{8+x}$ at 50 mK presented the first direct experimental evidence for the presence of Cooper-pair density wave (PDW). The detected PDW is coexisting

with the uniform d-wave superconductivity. Furthermore, considering the amplitude of the modulation of the Josephson critical current, the PDW is subdominant to the uniform d-wave superconductivity.

Further correlation analysis in the PDW measured in $I_C(\boldsymbol{r})$ and Bogoliubov quasiparticle density of states measured in conductance map, $g(\boldsymbol{r}, E)$, may reveal the signature of the PDW in single-particle tunneling measurement. There have been already vast quantities of single-particle tunneling measurement in cuprates and revisiting these abundant data with the signature of the PDW may help to resolve the problems in cuprate physics.

The novel techniques introduced in this thesis can be extended to any materials having layered structures, for example, iron-based superconductors. Moreover, the *in-situ* tip preparation stage can be extended to have multiple targets in order to render a tip to various states, such as ferromagnetic for spin-polarized STM. This enables to study heterostructures formed between tip and sample.

Bibliography

[1] Onnes, H.K., Commun. Phys. Lab. Univ. Laiden, 1911. **120b, 122b, 124c**.

[2] Meissner, W. and R. Ochsenfeld, *Ein neuer Effekt bei Eintritt der Supraleitf"ahigkeit.* Naturwissenschaften, 1993. **21**: p. 787-788.

[3] London, F. and H. London, *The Electromagnetic Equations of the Superconductor.* Proc. R. Soc. Lond. Math. Phys. Eng. Sci., 1935. **149**(866): p. 71-88.

[4] Ginzburg, V.L. and L.D. Landau, *On the theory of superconductivity.* Zh. Eksperim. iiTeor.Fiz., 1950. **20**: p. 1064-1082.

[5] Bardeen, J., L.N. Cooper, and J.R. Schrieffer, *Theory of Superconductivity.* Physical Review, 1957. **108**: p. 1175-1204.

[6] Gavaler, J.R., *Superconductivity in Nb-Ge films above 22 K.* Applied Physics Letters, 1973. **23**: p. 480.

[7] Bednorz, G. and K.A. Muller, *Possible high Tc superconductivity in the Ba-La-Cu-O system.* Z. Phys. B 1986. **64**: p. 189-193

[8] Wu, M.K., *Superconductivity at 93 K in a New Mixed-Phase Y-Ba-Cu-O Compound System at Ambient Pressure.* Physical Review Letters, 1987. **58**: p. 908

[9] Gao, L., *et al.*, *Superconductivity up to 164-K in* $HgBa_2Ca_{m-1}Cu_mO_{2m+2+\delta}$ *(m = 1, 2, and 3) under Quasi-Hydrostatic Pressures.* Physical Review B, 1994. **50**(6): p. 4260-4263.

[10] Kamihara, Y., *et al.*, *Iron-based layered superconductor* $La[O_{1-x}F_x]FeAs$ *(x=0.05-0.12) with T-c=26 K.* Journal of the American Chemical Society, 2008. **130**(11): p. 3296-+.

[11] Rotter, M., M. Tegel, and D. Johrendt, *Superconductivity at 38 K in the iron arsenide* $(Ba_{1-x}K_x)Fe_2As_2$. Physical Review Letters, 2008. **101**(10).

[12] Paglione, J. and R.L. Greene, *High-temperature superconductivity in iron-based materials.* Nature Physics, 2010. **6**: p. 645.

[13] Drozdov, A.P., *et al.*, *Conventional superconductivity at 203 kelvin at*

high pressures in the sulfur hydride system. Nature, 2015. **525**: p. 73.

[14] Cao, Y.*, et al.*, *Unconventional superconductivity in magic-angle graphene superlattices.* Nature, 2018. **556**: p. 43.

[15] Tinkham, M., *Introduction to Superconductivity: Second Edition*. 2004: Dover Publication, Mineola, Ny.

[16] Valatin, J.G., *Comments on the theory of superconductivity.* Il Nuovo Cimento (1955-1965), 1958. **7**(6): p. 843-857.

[17] Bogoljubov, N.N., *On a new method in the theory of superconductivity.* Il Nuovo Cimento (1955-1965), 1958. **7**(6): p. 794-805.

[18] Hubbard, J., *Electron correlations in narrow energy bands.* Proc. Royal Soc. Lond., 1963. **276**: p. 238.

[19] Ohta, Y., T. Tohyama, and S. Maekawa, *Charge-transfer gap and superexchange interaction in insulating cuprates.* Physical Review Letters, 1991. **66**(9): p. 1228-1231.

[20] Mott, N.F. and R. Peierls, *Discussion of the paper by de Boer and Verwey.* Proceedings of the Physical Society, 1937. **49**(4S): p. 72-73.

[21] Zaanen, J. and G.A. Sawatzky, *The electronic structure and superexchange interactions in transition-metal compounds.* Canadian Journal of Physics, 1987. **65**(10): p. 1262-1271.

[22] Imada, M., A. Fujimori, and Y. Tokura, *Metal-insulator transitions.* Reviews of Modern Physics, 1998. **70**(4): p. 1039-1263.

[23] Zaanen, J., G.A. Sawatzky, and J.W. Allen, *Band gaps and electronic structure of transition-metal compounds.* Physical Review Letters, 1985. **55**(4): p. 418-421.

[24] Bianconi, A.*, et al.*, *Localization of Cu 3d levels in the high Tc superconductor $YBa_2Cu_3O_7$ by Cu 2p X-ray photoelectron spectroscopy.* Solid State Communications, 1987. **63**(12): p. 1135-1139.

[25] Takahashi, T.*, et al.*, *Synchrotron-radiation photoemission study of*

the high-T_c superconductor $Y_2Ba_3CuO_{7-\delta}$. Physical Review B, 1987. **36**(10): p. 5686-5689.

[26] Varma, C.M., S. Schmitt-Rink, and E. Abrahams, *Charge transfer excitations and superconductivity in "ionic" metals.* Solid State Communications, 1987. **62**(10): p. 681-685.

[27] Emery, V.J., *Theory of high-T_c superconductivity in oxides.* Physical Review Letters, 1987. **58**(26): p. 2794-2797.

[28] Zhang, F.C. and T.M. Rice, *Effective Hamiltonian for the superconducting Cu oxides.* Physical Review B, 1988. **37**(7): p. 3759-3761.

[29] Ding, H., *et al.*, *Angle-resolved photoemission spectroscopy study of the superconducting gap anisotropy in $Bi_2Sr_2CaCu_2O_{8+x}$.* Physical Review B, 1996. **54**(14): p. R9678-R9681.

[30] Zeng, B., *et al.*, *Anisotropic structure of the order parameter in $FeSe_{0.45}Te_{0.55}$ revealed by angle-resolved specific heat.* Nature Communications, 2010. **1**.

[31] Alldredge, J.W., *et al.*, *Evolution of the electronic excitation spectrum with strongly diminishing hole density in superconducting $Bi_2Sr_2CaCu_2O_{8+\delta}$.* Nature Physics, 2008. **4**(4): p. 319-326.

[32] Renner, C. and O. Fischer, *Vacuum tunneling spectroscopy and asymmetric density of states of $Bi_2Sr_2CaCu_2O_{8+\delta}$.* Physical Review B, 1995. **51**(14): p. 9208-9218.

[33] Tsuei, C.C. and J.R. Kirtley, *Pairing symmetry in cuprate superconductors.* Reviews of Modern Physics, 2000. **72**(4): p. 969-1016.

[34] Tsuei, C.C., *et al.*, *Pairing Symmetry and Flux-Quantization in a Tricrystal Superconducting Ring of $YBa_2Cu_3O_{7-\delta}$.* Physical Review Letters, 1994. **73**(4): p. 593-596.

[35] Vanharlingen, D.J., *Phase-Sensitive Tests of the Symmetry of the Pairing State in the High-Temperature Superconductors - Evidence for D_{X2-Y2} Symmetry.* Reviews of Modern Physics, 1995. **67**(2): p. 515-535.

[36] Warren, W.W., *et al.*, *Cu Spin Dynamics and Superconducting Precursor Effects in Planes above Tc in $YBa_2Cu_3O_{6.7}$.* Physical Review Letters, 1989. **62**(10): p. 1193-1196.

[37] Kordyuk, A.A., *Pseudogap from ARPES experiment: Three gaps in cuprates and topological superconductivity (Review Article).* Low Temperature Physics, 2015. **41**(5): p. 319-341.

[38] Tanaka, K., *et al.*, *Distinct Fermi-momentum-dependent energy gaps in deeply underdoped Bi2212.* Science, 2006. **314**(5807): p. 1910-1913.

[39] Damascelli, A., Z. Hussain, and Z.X. Shen, *Angle-resolved photoemission studies of the cuprate superconductors.* Reviews of Modern Physics, 2003. **75**(2): p. 473-541.

[40] Homes, C.C., *et al.*, *Optical Conductivity of C-Axis Oriented $YBa_2Cu_3O_{6.70}$ - Evidence for a Pseudogap.* Physical Review Letters, 1993. **71**(10): p. 1645-1648.

[41] Basov, D.N. and T. Timusk, *Electrodynamics of high-T-c superconductors.* Reviews of Modern Physics, 2005. **77**(2): p. 721-779.

[42] Timusk, T. and B. Statt, *The pseudogap in high-temperature superconductors: an experimental survey.* Reports on Progress in Physics, 1999. **62**(1): p. 61-122.

[43] Lee, W.S., *et al.*, *Abrupt onset of a second energy gap at the superconducting transition of underdoped Bi2212.* Nature, 2007. **450**: p. 81.

[44] Kaminski, A., *et al.*, *Pairing, pseudogap and Fermi arcs in cuprates.* Philosophical Magazine, 2015. **95**(5-6): p. 453-466.

[45] Kohsaka, Y., *et al.*, *How Cooper pairs vanish approaching the Mott insulator in $Bi_2Sr_2CaCu_2O_{8+\delta}$.* Nature, 2008. **454**: p. 1072.

[46] Fujita, K., *et al.*, *Simultaneous Transitions in Cuprate Momentum-Space Topology and Electronic Symmetry Breaking.* Science, 2014. **344**(6184): p. 612.

[47] He, Y., *et al.*, *Fermi Surface and Pseudogap Evolution in a Cuprate*

Superconductor. Science, 2014. **344**(6184): p. 608.

[48] Kohsaka, Y., *et al., An Intrinsic Bond-Centered Electronic Glass with Unidirectional Domains in Underdoped Cuprates.* Science, 2007. **315**(5817): p. 1380.

[49] Hamidian, M.H., *et al., Atomic-scale electronic structure of the cuprate d-symmetry form factor density wave state.* Nature Physics, 2015. **12**: p. 150.

[50] Parker, C.V., *et al., Fluctuating stripes at the onset of the pseudogap in the high-Tc superconductor Bi2Sr2CaCu2O8+x.* Nature, 2010. **468**: p. 677.

[51] Wise, W.D., *et al., Charge-density-wave origin of cuprate checkerboard visualized by scanning tunnelling microscopy.* Nature Physics, 2008. **4**: p. 696.

[52] Boyer, M.C., *et al., Imaging the two gaps of the high-temperature superconductor* $Bi_2Sr_2CuO_{6+x}$. Nature Physics, 2007. **3**: p. 802.

[53] Pushp, A., *et al., Extending Universal Nodal Excitations Optimizes Superconductivity in* $Bi_2Sr_2CaCu_2O_{8+\delta}$. Science, 2009. **324**(5935): p. 1689.

[54] Lawler, M.J., *et al., Intra-unit-cell electronic nematicity of the high-Tc copper-oxide pseudogap states.* Nature, 2010. **466**: p. 347.

[55] Le Tacon, M., *et al., Two energy scales and two distinct quasiparticle dynamics in the superconducting state of underdoped cuprates.* Nature Physics, 2006. **2**(8): p. 537-543.

[56] Hufner, S., *et al., Two gaps make a high-temperature superconductor?* Reports on Progress in Physics, 2008. **71**(6).

[57] Fradkin, E., S.A. Kivelson, and J.M. Tranquada, *Colloquium: Theory of intertwined orders in high temperature superconductors.* Reviews of Modern Physics, 2015. **87**(2): p. 457-482.

[58] Comin, R. and A. Damascelli, *Resonant X-Ray Scattering Studies of Charge Order in Cuprates.* Annual Review of Condensed Matter Physics, 2016. **7**(1): p. 369-405.

[59] Tranquada, J.M., *et al., Evidence for stripe correlations of spins and*

holes in copper oxide superconductors. Nature, 1995. **375**(6532): p. 561-563.

[60] Hücker, M., *et al.*, *Stripe order in superconducting La${}_{2\ensuremath{-}x}$Ba${}_{x}$CuO${}_{4}$ ($0.095\ensuremath{\leqslant}x\ensuremath{\leqslant}0.155$).* Physical Review B, 2011. **83**(10): p. 104506.

[61] Abbamonte, P., *et al.*, *Spatially modulated 'Mottness' in $La_{2-x}Ba_xCuO_4$.* Nature Physics, 2005. **1**(3): p. 155-158.

[62] Fujita, M., *et al.*, *Structural effect on the static spin and charge correlations in $La_{1.875}Ba_{0.125-x}Sr_xCuO_4$.* Physical Review B, 2002. **66**(18): p. 184503.

[63] Fink, J., *et al.*, *Charge ordering in $La_{1.8-x}Eu_{0.2}Sr_xCuO_4$ studied by resonant soft x-ray diffraction* Physical Review B, 2009. **79**(10): p. 100502.

[64] LeBoeuf, D., *et al.*, *Electron pockets in the Fermi surface of hole-doped high-Tc superconductors.* Nature, 2007. **450**: p. 533.

[65] Hussey, N.E., *et al.*, *A coherent three-dimensional Fermi surface in a high-transition-temperature superconductor.* Nature, 2003. **425**(6960): p. 814-817.

[66] Platé, M., *et al.*, *Fermi Surface and Quasiparticle Excitations of Overdoped $Tl_2Ba_2CuO_{6+\delta}$.* Physical Review Letters, 2005. **95**(7): p. 077001.

[67] Ghiringhelli, G., *et al.*, *Long-Range Incommensurate Charge Fluctuations in (Y,Nd)$Ba_2Cu_3O_{6+x}$.* Science, 2012. **337**(6096): p. 821.

[68] Hoffman, J.E., *et al.*, *A Four Unit Cell Periodic Pattern of Quasi-Particle States Surrounding Vortex Cores in $Bi_2Sr_2CaCu_2O_{8+\delta}$.* Science, 2002. **295**(5554): p. 466.

[69] Hanaguri, T., *et al.*, *Quasiparticle interference and superconducting gap in $Ca_{2-x}Na_xCuO_2Cl_2$.* Nature Physics, 2007. **3**: p. 865.

[70] Comin, R., *et al.*, *Charge Order Driven by Fermi-Arc Instability in $Bi_2Sr_{2-x}La_xCuO_{6+\delta}$.* Science, 2014. **343**(6169): p. 390-392.

[71] da Silva Neto, E.H., *et al.*, *Ubiquitous Interplay Between Charge Ordering and High-Temperature Superconductivity in Cuprates.* Science, 2014. **343**(6169): p. 393.

[72] Zhao, H., *et al.*, *Charge-stripe crystal phase in an insulating cuprate.* Nature Materials, 2019. **18**(2): p. 103-107.

[73] Giaever, I., *Energy Gap in Superconductors Measured by Electron Tunneling.* Physical Review Letters, 1960. **5**(4): p. 147-148.

[74] Bardeen, J., *Tunnelling from a Many-Particle Point of View.* Physical Review Letters, 1961. **6**(2): p. 57-59.

[75] Binnig, G., *et al.*, *Surface Studies by Scanning Tunneling Microscopy.* Physical Review Letters, 1982. **49**(1): p. 57-61.

[76] Fischer, Ø., *et al.*, *Scanning tunneling spectroscopy of high-temperature superconductors.* Reviews of Modern Physics, 2007. **79**(1): p. 353-419.

[77] Tersoff, J. and D.R. Hamann, *Theory and Application for the Scanning Tunneling Microscope.* Physical Review Letters, 1983. **50**(25): p. 1998-2001.

[78] Pan, S.H., E.W. Hudson, and J.C. Davis, *3He refrigerator based very low temperature scanning tunneling microscope.* Review of Scientific Instruments, 1999. **70**(2): p. 1459-1463.

[79] Wintterlin, J., *et al.*, *Atomic-Resolution Imaging of Close-Packed Metal Surfaces by Scanning Tunneling Microscopy.* Physical Review Letters, 1989. **62**(1): p. 59-62.

[80] Chen, C.J., *Microscopic view of scanning tunneling microscopy.* Journal of Vacuum Science & Technology A, 1991. **9**(1): p. 44-50.

[81] Ernst, S., *et al.*, *Tip preparation for usage in an ultra-low temperature UHV scanning tunneling microscope.* Science and Technology of Advanced Materials, 2007. **8**(5): p. 347-351.

[82] Naaman, O., W. Teizer, and R.C. Dynes, *Fluctuation Dominated Josephson Tunneling with a Scanning Tunneling Microscope.* Physical Review Letters, 2001. **87**(9): p. 097004.

[83] Rodrigo, J.G., H. Suderow, and S. Vieira, *On the use of STM*

superconducting tips at very low temperatures. The European Physical Journal B – Condensed Matter and Complex Systems, 2004. **40**(4): p. 483–488.

[84] Proslier, T.*, et al.*, *Probing the superconducting condensate on a nanometer scale.* Europhysics Letters, 2006. **73**(6): p. 962–968.

[85] Kimura, H.*, et al.*, *Josephson scanning tunneling microscopy: A local and direct probe of the superconducting order parameter.* Physical Review B, 2009. **80**(14): p. 144506.

[86] Andreev, A.F., *The Thermal Conductivity of the Intermediate State in Superconductors.* Soviet Physics Jetp-Ussr, 1964. **19**(5): p. 1228–1231.

[87] Klapwijk, T.M., G.E. Blonder, and M. Tinkham, *Explanation of subharmonic energy gap structure in superconducting contacts.* Physica B+C, 1982. **109–110**: p. 1657–1664.

[88] Josephson, B.D., *Possible new effects in superconductive tunnelling.* Physics Letters, 1962. **1**(7): p. 251–253.

[89] Nicol, J., S. Shapiro, and P.H. Smith, *Direct Measurement of the Superconducting Energy Gap.* Physical Review Letters, 1960. **5**(10): p. 461–464.

[90] Anderson, P.W. and J.M. Rowell, *Probable Observation of the Josephson Superconducting Tunneling Effect.* Physical Review Letters, 1963. **10**(6): p. 230–232.

[91] Ambegaokar, V. and A. Baratoff, *Tunneling Between Superconductors.* Physical Review Letters, 1963. **10**(11): p. 486–489.

[92] Ambegaokar, V. and A. Baratoff, *Tunneling Between Superconductors.* Physical Review Letters, 1963. **11**(2): p. 104–104.

[93] Devoret, M.H.*, et al.*, *Effect of the electromagnetic environment on the Coulomb blockade in ultrasmall tunnel junctions.* Physical Review Letters, 1990. **64**(15): p. 1824–1827.

[94] Grabert, H. and M.H. Devoret, *Single Charge Tunneling.* Vol. Vol. 294. NATO ASI Series. Boston, MA: Springer US, 1992.

[95] Kautz, R.L. and J.M. Martinis, *Noise-affected I-V curves in small hysteretic Josephson junctions.* Physical Review B, 1990. **42**(16): p. 9903-9937.

[96] Martinis, J.M. and R.L. Kautz, *Classical phase diffusion in small hysteretic Josephson junctions.* Physical Review Letters, 1989. **63**(14): p. 1507-1510.

[97] Cleland, A.N., J.M. Schmidt, and J. Clarke, *Charge fluctuations in small-capacitance junctions.* Physical Review Letters, 1990. **64**(13): p. 1565-1568.

[98] Ivanchenko, Y.M. and L.A. Zil'berman, *The Josephson effect in small tunnel contacts.* Sov. Phys. JETP 1969. **28**: p. 1272.

[99] Ingold, G.-L., H. Grabert, and U. Eberhardt, *Cooper-pair current through ultrasmall Josephson junctions.* Physical Review B, 1994. **50**(1): p. 395-402.

[100] Grabert, H. and G.-L. Ingold, *Mesoscopic Josephson effect.* Superlattices and Microstructures, 1999. **25**(5): p. 915-923.

[101] Caldeira, A.O. and A.J. Leggett, *Quantum tunnelling in a dissipative system.* Annals of Physics, 1983. **149**(2): p. 374-456.

[102] Pan, S.H.*, et al.*, *Imaging the effects of individual zinc impurity atoms on superconductivity in* $Bi_2Sr_2CaCu_2O_{8+\delta}$. Nature, 2000. **403**(6771): p. 746-750.

[103] McElroy, K.*, et al.*, *Relating atomic-scale electronic phenomena to wave-like quasiparticle states in superconducting*$Bi_2Sr_2CaCu_2O_{8+\delta}$. Nature, 2003. **422**(6932): p. 592-596.

[104] Howald, C., P. Fournier, and A. Kapitulnik, *Inherent inhomogeneities in tunneling spectra of* $Bi_2Sr_2CaCu_2O_{8+x}$ *crystals in the superconducting state.* Physical Review B, 2001. **64**(10): p. 100504.

[105] Hashimoto, M.*, et al.*, *Direct spectroscopic evidence for phase competition between the pseudogap and superconductivity in* $Bi_2Sr_2CaCu_2O_{8+\delta}$. Nature Materials, 2014. **14**: p. 37.

[106] Vishik, I.M.*, et al.*, *Phase competition in trisected superconducting dome.* Proceedings of the National Academy of Sciences, 2012.

109(45): p. 18332-18337.

[107] Chang, J., *et al.*, *Direct observation of competition between superconductivity and charge density wave order in $YBa_2Cu_3O_{6.67}$.* Nature Physics, 2012. **8**: p. 871.

[108] Berg, E., *et al.*, *Dynamical layer decoupling in a stripe-ordered High-T_c superconductor.* Physical Review Letters, 2007. **99**(12).

[109] Berg, E., *et al.*, *Striped superconductors: how spin, charge and superconducting orders intertwine in the cuprates.* New Journal of Physics, 2009. **11**.

[110] Kivelson, S.A., *et al.*, *How to detect fluctuating stripes in the high-temperature superconductors.* Reviews of Modern Physics, 2003. **75**(4): p. 1201-1241.

[111] Himeda, A., T. Kato, and M. Ogata, *Stripe States with Spatially Oscillating d-Wave Superconductivity in the Two-Dimensional t-t'-J Model.* Physical Review Letters, 2002. **88**(11): p. 117001.

[112] Fulde, P. and R.A. Ferrell, *Superconductivity in a Strong Spin-Exchange Field.* Physical Review, 1964. **135**(3A): p. A550-A563.

[113] Larkin, A.I. and Y.N. Ovchinnikov, *Nonuniform state of superconductors.* Sov. Phys. JETP, 1965. **20**: p. 762.

[114] Matsuda, Y. and H. Shimahara, *Fulde-Ferrell-Larkin-Ovchinnikov State in Heavy Fermion Superconductors.* Journal of the Physical Society of Japan, 2007. **76**(5): p. 051005.

[115] Clogston, A.M., *Upper Limit for the Critical Field in Hard Superconductors.* Physical Review Letters, 1962. **9**(6): p. 266-267.

[116] Kinnunen, J.J., *et al.*, *The Fulde-Ferrell-Larkin-Ovchinnikov state for ultracold fermions in lattice and harmonic potentials: a review.* Reports on Progress in Physics, 2018. **81**(4): p. 046401.

국 문 초 록

1986년 최초로 고온 초전도체가 발견된 이후 많은 이론적 및 실험적 연구가 진행되었다. 이러한 노력에도 불구하고 구리화합물 고온 초전도체 현상을 완전히 이해하지 못하고 있고, 이러한 난제들은 여러 상들이 얽혀있는 상평형 그림에서 기인한다. 본 연구는 고온 초전도 현상에 직접적으로 접근하고자 하였다.

본 연구에서는 나노미터 해상력을 가진 주사형 조셉슨 터널링 현미경을 처음으로 고온 초전도체인 $Bi2Sr2CaCu2O_{8+x}$에 적용하였다. 조셉슨 전류 혹은 Cooper-pair 터널링 전류를 통해 초전도 질서 변수와 초전도 응축체를 측정할 수 있었다. In-situ 팁 스테이지를 통해 *in-situ* 가공한 $Bi_2Sr_2CaCu_2O_{8+x}$팁이 사용되었다.

주사형 조셉슨 터널링 현미경 연구는 4.2 K과 50 mK 두 온도에서 수행하였다. 두 온도 모두에서 나노미터 해상도로 조셉슨 임계 전류를 측정할 수 있음으로 상세히 규명했다. 4.2 K에서 수행한 주사형 조셉슨 터널링 현미경 연구에서는 처음으로 초전도 갭의 공간상의 변화를 직접 측정하였으며, 주사형 조셉슨 터널링 현미경의 측정 가능 온도 범위를 mK에서 4.2 K으로 상승시켰다. 50 mK에서 수행한 주사형 조셉슨 터널링 현미경 연구에서는 초전도 응축체가 주기적으로 변화하는 것으로 처음으로 관측하였다.

주요어: 고온 초전도체, 주사형 조셉슨 터널링 현미경, 초전도 갭맵, 쿠퍼쌍 밀도파
학번: 2012-23101